RVJSTEAM
Volume 1 | Issue 2 | July 2020

Contents

RV College of Engineering®
RV Vidyaniketan Post, Mysuru Road, Bengaluru - 560 059, India
Phone: 080-67178020 , 67178161 : Fax: 0091-80-67178011
web: rvce.edu.in

Printed at: Ananya Prints, Bengaluru-560085
Phone: 9880528846

RV Journal of Science Technology Engineering Arts and Management Vol. 1 Issue 2 July 2020

RV College of Engineering®

Go, change the world

RVJSTEAM
Volume 1 | Issue 2 | July 2020

RV Journal of Science Technology Engineering Arts and Management

Published by
RV College of Engineering®
RV Vidyaniketan Post, Mysuru Road, Bengaluru-59, INDIA
Autonomous Institution affiliated to Visvesvaraya Technological University, Belagavi
Approved by AICTE, New Delhi
Accredited by NAAC, Bengaluru and NBA, New Delhi
Phone: 080-6717 8020, 8161 :: Fax: 0091-80-6717 8011
www.rvce.edu.in :: http://rvjstem.rvce.edu.in

RV College of Engineering®
RV Vidyaniketan Post, Mysuru Road, Bengaluru - 560 059, India
Phone: 080-67178020 , 67178161 : Fax: 0091-80-67178011
web: rvce.edu.in

Vision

Leadership in Quality Technical Education, Interdisciplinary Research & Innovation, with a Focus on Sustainable and Inclusive Technology.

Mission

- To deliver outcome based quality education, emphasizing on experiential learning with state-of-the-art infrastructure.
- To Create a conducive environment for interdisciplinary research and innovation.
- To develop professionals through holistic education focusing on individual growth, discipline, integrity, ethics and social sensitivity.
- To nurture industry-institution collaboration learning to competency enhancement and entrepreneurship.
- To focus on technologies that are sustainable and inclusive, benefitting all sections of the society.

Quality Policy

Achieving Excellence in Technical Education, Research and Consulting through an Outcome Based Curriculum focusing on Continuous Improvement and Innovation by Benchmarking against the global Best Practices.

Author Guidelines

For Authors to submit manuscript, scan

RVJSTEAM

RV Journal of Science Technology Engineering Arts and Management

Editorial

On behalf of the Board of RV Journal of Science, Technology, Engineering, Arts and Management, and my co-editors, I am glad to present the Volume 1, Issue 2 of the Journal. Amidst COVID-19 from March till date, the second issue of RVJSTEAM has taken a good shape in terms of number of papers received from faculty & research scholars and UG/PG students. Editorial committee was entrusted with review of papers for quality. Out of the selected papers, 12 technical papers in the areas of Automobile, IoT, Civil, Mechatronics, Mechanical, Cloud computing, Thin films, Biotechnology, Facilities Planning are selected for publication. Some of the papers are data driven and case study oriented. Experts have selected papers from all the streams of Science, Engineering, Technology and Management.

There is a slight modification in the cover page in order to meet the requirements of ISSN board. In the subsequent issues, the Journal will also possess ISSN and quality of papers will see newer heights. The editorial board is meeting frequently and addressing the gaps and further enriching this journal. All these developments are promising signs, we could grow at a better pace with the support of the board members and intellectual generosity of the readers and contributors

I congratulate all the authors for publication of good quality journal papers. Post COVID-19, the opportunities are enormous for good publications adding value to the research domain of STEAM.

Dr K N Subramanya
Principal, RVCE, Bengaluru, India
Editor-in-Chief

RVJSTEAM

RV Journal of Science Technology Engineering Arts and Management

Board of Editors

Editor-in-Chief

Dr K N Subramanya
Principal, RV College of Engineering®, Bengaluru, India
Email: principal@rvce.edu.in

Managing Editor

Dr H N Narasimha Murthy
Professor & Dean, R&D, RV College of Engineering®, Bengaluru, India
Email: narasimhamurthyhn@rvce.edu.in

Editors

Dr S S Iyengar
Computer Scientist and Distinguished University Professor, Ryder Professor and Director of Computer Science, Florida International University-USA
Email: iyengar@cis.fiu.edu

Dr Arokiaswami Alphones
Associate Professor, School of Electrical & Electronic Engineering,
Nanyang Technological University, Singapore
Email:ealphones@ntu.edu.sg

Dr K P Gopinathan
Professor INSA Hon. Scientist
IISc, Bengaluru, India
Email: kpg@mcbl.iisc.ernet.in

Dr M Mathirajan
Chief Research Scientist
Management Studies IISc, Bengaluru, India
Email: msdmathi@iisc.ac.in

Dr Prasanta Kumar Panda
Chief Scientist & Head
Materials Science Division
CSIR-NAL, Bengaluru, India
Email: pkpanda@nal.res.in

Dr S Satyanarayana
Professor, Dept of Chemistry
RV College of Engineering®
Email: satya.s@rvce.edu.in

Dr M Krishna
Professor and Head, Dept. of Mechanical Engineering, RV College of Engineering®
Email: krishnam@rvce.edu.in

Dr. S Ravishankar
Professor, Dept of Electronics & Communication Engg., RV College of Engineering®
Email: ravishankars@rvce.edu.in

Dr. Pushpa Agrawal
Professor, Dept of Biotechnology
RV College of Engineering®
Email: pushpa_agrawal@rvce.edu.in

Dr M Uttarakumari
Professor, Dept. of Electronics and Communication Engineering
RV College of Engineering®
Email: uttarakumari@rvce.edu.in

Dr B G Sudarshan
Associate Professor, Dept. of Electronics and Instrumentation Engineering
RV College of Engineering®
Email: sudarshanbg@rvce.edu.in

Dr K Uma Rao
Professor, Dept of Electronics Electrical Engineering, RV College of Engineering®
Email: umaraok@rvce.edu.in

Dr K Sreelakshmi
Professor and Head, Dept. of Telecommunication Engg., RV College of Engineering®
Email: sreelakshmik@rvce.edu.in

Dr P Ramakanth Kumar
Professor and Head, Dept. of Computer Science Engg., RV College of Engineering®
Email: ramakanthkp@rvce.edu.in

Dr M V Renuka Devi
Professor, Dept of Civil Engineering
RV College of Engineering®
Email: renukadevimv@rvce.edu.in

Dr N S Narahari
Professor, Dept. of Industrial Engineering and Management, RV College of Engineering®
Email: naraharins@rvce.edu.in

Dr G Shobha
Professor, Dept of Computer Science Engg.
RV College of Engineering®
Email: shobhag@rvce.edu.in

Dr. B Sathish Babu
Professor, Dept of Computer Science Engg .
RV College of Engineering®
Email: bsbabu@rvce.edu.in

Dr G R Rajkumar
Associate Professor, Dept of Mechanical Engg.
RV College of Engineering®
Email: rajkuargr@rvce.edu.in

Dr Gangadhar Angadi
Asst. Professor, Dept of Mechanical Engg.
RV College of Engineering®
Email: gangadharangadi@rvce.edu.in

Associate Editors

Dr Rajalakshmi Mudbidre
Asst. Professor, Dept of Chemiical Engg.
RV College of Engineering®
Email: rajalakshmim@rvce.edu.in

Dr Sumanta Manokaran
Asst. Professor, Dept of Biotechnology
RV College of Engineering®
Email: sumathram@rvce.edu.in

Dr N Shylashree
Associate Professor, Dept of Electronics & Communication Engineering
RV College of Engineering®
Email: shylashreen@rvce.edu.in

Dr Rachana S Akki
Asst. Professor, Dept of Electronics & Instrumentation Engg., RV College of Engineering®
Email: rachana.akki@rvce.edu.in

Dr Kartik Shastry
Asst. Professor, Dept of Physics
RV College of Engineering®
Email: karthikshastryc@rvce.edu.in

Dr B S Premananda
Associate Professor, Dept of Electronics & Telecommunication & Engg.
RV College of Engineering®
Email: premanandabs@rvce.edu.in

Dr Sridevi T R
Librarian, RV College of Engineering®
Email: sridevitr@rvce.edu.in

Dr A Bharathish
Asst. Professor, Dept of Mechanical Engg.
RV College of Engineering®
Email: bhartishachutarao@rvce.edu.in

Dr S Nagesh
Asst. Professor, Dept of Mechanical Engg.
RV College of Engineering®
Email: nageshs@rvce.edu.in

Dr. Shivaraj B W
Asst. Professor, Dept of Mechanical Engg.
RV College of Engineering®
Email: shivrajwali@rvce.edu.in

M R Archana
Asst. Professor, Dept of Civil Engg.
RV College of Engineering®
Email: archanamr@rvce.edu.in

R Jyothi
Asst. Professor, Dept of Electrical & Electronics Engg.
RV College of Engineering®
Email: jyothir@rvce.edu.in

S G Raghavendra Prasad
Asst. Professor, Dept of Information Science & Engg., RV College of Engineering®
Email: raghavendrap@rvce.edu.in

K Deepika
Asst. Professor, Dept of Master of Computer Applications, RV College of Engineering®
Email: deepikak@rvce.edu.in

Rajashekar PL
Asst. Professor, Dept of Mathematics
RV College of Engineering®
Email:rajashekarpl@rvce.edu.in

R Supreeth
Asst. Professor, Dept of Aerospace Engg.
RV College of Engineering®
Email:supreethr@rvce.edu.in

Contents

Aim and Scope

RV Journal of Science, Technology, Engineering Arts and Management (RVJSTEAM) is a biannual open access research journal of RV College of Engineering. RVJSTEAM features peer reviewed research articles in Engineering Sciences.Research articles such as Review, Technical papers and Letters are published after peer review.

Copyright©

Upon acceptance of an article, authors will be asked to complete a 'Journal Publishing Agreement. An e-mail will be sent to the corresponding author confirming receipt of the manuscript together with a 'Journal Publishing Agreement' form or a link to the online version of this agreement. Subscribers may reproduce tables of contents or prepare lists of articles including abstracts for internal circulation within their institutions. Permission of the Publisher is required for resale or distribution outside the institution and for all other derivative works, including compilations and translations. If excerpts from other copyrighted works are included, the author(s) must obtain written permission from the copyright owners and credit the source(s) in the article.

For Authors to submit manuscript, scan

Author Guidelines

Article Types

Review articles: Extensive and critical review of synthesised literature based on the current literature including the latest on one topic

Technical papers: Original articles with novelty in materials, processes, systems, tools, techniques, measurement methods and applications

Letters: High quality and breakthrough investigations which need immediate and rapid attention

Design and Performance Analysis of Memristor Based Non-Volatile SRAM Cell

Harish K[1], Girish B[1], Vinutha H L[1], Kariyappa B S[1*], Hemanth Kumar C S[2]

[1]*Department of Electronics and Communication Engineering, RV College of Engineering®, Bengaluru -59*

[2]*Department of Electronics and Communication Engineering, Government Engineering College, Ramangara-562159, Research scholar VTU Belagavi*

Abstract

Non-Volatile memories are gaining more importance in memory design due to their data retaining capability during power-down mode. Conventional 6 Transistor Static Random-Access Memory (SRAM) cell does not have Non-Volatile property. Memristor is one of the non-volatile techniques used in Non-Volatile SRAM (NVSRAM). This research deals with 7 Transistor and 1 Memristor (7T1M) based NVSRAM cell. Multi-threshold Complementary Metal Oxide Semiconductor (MTCMOS) power reduction technique was implemented to reduce the total power consumed in the circuit. Memristor was modelled using Verilog-A code in the Cadence Virtuoso tool and its hysteresis behaviour was obtained for the better Static Noise Margin (SNM) value. The designed Memristor was integrated with Volatile SRAM to realize NVSRAM cell. Both 7T2M and the proposed 7T1M architectures were analyzed for the delay, power, and SNM values. The proposed 7T1M NVSRAM cell has a higher SNM value of 0.518 V, whereas the 7T2M NVSRAM cell has the SNM value of 0.04V. Delay in the two architectures is nearly same. The 7T1M cell has slightly more power because the bistable element is directly connected to the ground. The 6T SRAM cell, 7T2M NVSRAM cell, 7T1M NVSRAM cell, and MTCMOS based 7T1M NVSRAM cell were implemented in Cadence Virtuoso tool at 45 nm technology with operating voltage 1.2V.

***Keywords**: Memristor, NVSRAM (Non-Volatile Static Random-Access Memory), SNM (Static Noise Margin), MTCMOS, HRS (High Resistance State), LRS(Low Resistance State).*

1.0 Introduction

In VLSI design, memory plays a very important role. The critical issues associated with memories are operation speed, noise immunity, area, and power consumption. There are two types of memories SRAM and Dynamic RAM (DRAM). DRAM structure has a transistor and the capacitor. It has only one transistor and one capacitor. The capacitor is used for data storage by charging it. The main property of the DRAM is periodic refreshing. It is inevitable to refresh the DRAM after every cycle which increases the power dissipation of

---

**Mail address: Kariyappa B S, Professor, Department of Electronics and Communication Engg., RV College of Engineering®, Bengaluru – 59*
Email: kariyappabs@rvce.edu.in, *Ph.: +91 9449223582*

the circuit. So, the SRAMs are used for high-speed memory design to avoid periodic refreshing. The SRAM provides high read and write stability by using a bistable inverter element in its structure. These properties of SRAM make them preferable over DRAM [1]. A detailed study is reported on SRAM for selecting suitable architecture for the design. The study revealed that 6T architecture is preferred over the 4T architecture [2]. The 4T SRAM has less area but it has more power dissipation and higher write and read access time. Due to the more delay exhibited by the 4T SRAM cell, the 6T SRAM cell is used for the design which has a better noise margin, lesser delay, and also lower power dissipation. The volatile nature of the SRAM cell makes the cell to lose the data whenever the power goes off. So, to make volatile SRAM as Non-Volatile, different Non-Volatile techniques are to be used along with the conventional 6T SRAM cell. Then the cell will be able to restore the data after the power comes back. This feature of the cell is known as Non-Volatility.

Different Non-Volatile technologies to make the SRAM as NVSRAM are Ferroelectric RAM (FeRAM), Magnetic Tunnel Junction RAM (MTJ RAM), Memristor RAM (MRAM), Resistive RAM (RRAM) [3], Phase Change RAM, etc. A memristor is a Non-Volatile memory component that has the ability to restore the data back after power down. This Non-Volatility of the Memristor is got by changing its resistance during on and off mode thereby it stores the data when there is no power. The two resistance states of Memristor are the High Resistance State (HRS) and Low Resistance State (LRS). Memristors are widely used in many devices because it will add the Non-Volatile feature for that device that means the device can retain the memory without power. The Memristor will change its resistance state from HRS to LRS during its operation and it limits the current in one direction and increases the current in other direction. Memristors are considered as a sub-category of Resistive RAM(RRAM). Memristor has higher SNM and endurance than that of any other technologies. Thus, Memristor is widely used in Non-Volatile memory designs.

The NVSRAM is in demand because of its Non-Volatile property. Different Non-Volatile techniques are used to make SRAM as Non-Volatile. Amongst different models of Memristor, the VTEAM model showed better performance [4]. To overcome the volatile property of SRAM, the seven Transistor and two Memristor based NVSRAM has been proposed [5]. The 7T2M NVSRAM cell had a good read and write margins when compared to other NVSARM architectures but had a lesser value of SNM. To reduce the overall power of the NVSRAM circuit many power reduction techniques such as MTCMOS and Self Controllable Voltage (SVL) have been implemented [6] and the significant reduction in the total power is observed.

Passive elements like resistor, capacitor and inductor are the basic fundamental elements in circuit design. The Memristor acts like a fourth fundamental passive element [7].

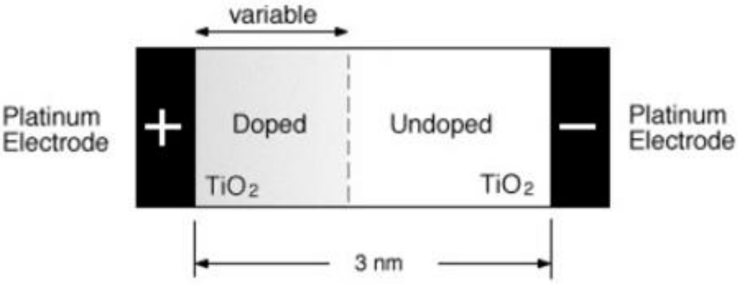

Fig. 1. Structure of a Physical Memristor [8]

The Memristor has two terminals: positive terminal and negative terminal. The positive and negative terminal of the Memristor is made of the Platinum electrode. The positive and negative terminal is decided based on the doping level of Titanium Dioxide (TiO2). The physical structure of a Memristor is shown in Fig. 1. If the TiO2 is heavily doped, then that side of the Memristor is the positive terminal and the opposite side is the negative terminal [9]. The doping concentration can be variable. When the high electric field is applied to the TiO2, its dopants try to move in the direction of the current. The applied voltage between two terminals makes oxygen atoms drift towards left or right and depending upon the voltage applied the material will become thicker or thinner. If the material is thicker, then the device is in the HRS state and if the material is thinner then the device is in the LRS state.

The SRAM is the basic component of the memory. The SRAM stores the data if the power is supplied to the circuit. This property of SRAM is known as volatility. There are many configurations of SRAM like 4T, 5T, 6T, and so on. Every configuration of SRAM has its advantages and drawbacks in terms of power, area, and delay. The 4T SRAM has a smaller on-chip area but the power consumption is very high. Therefore, 6T SRAM is concluded as the optimized design of the SRAM [10].

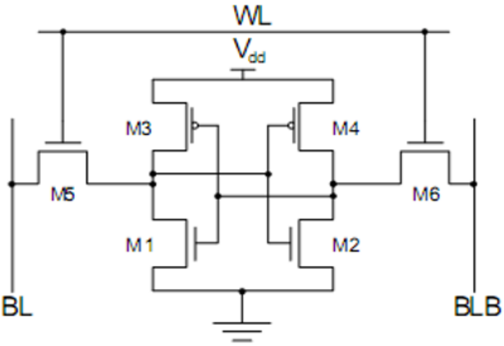

Fig. 2. Schematic of Conventional 6T SRAM circuit

The conventional 6T SRAM consists of two cross-coupled inverters [11]. As the inverters have two stable states that are ‘0’ and ‘1’, the 6T SRAM configuration is stable. It has both read and write phases of operation. In 6T SRAM cell, the inverter is connected to the bit line and the complementary line through the access transistors. Bit lines act as input during the write operation and as output during the read operation. The control of the access transistors is done with another line called word line which is used to control the read and write phases of the cell. Fig. 2 shows the schematic of a conventional 6T SRAM using the CMOS technology. The circuit operates at the voltage of 1.2 V.

6T SRAM can be analyzed in two modes of operations:

Write Mode: During write ‘1’ operation, BL is made ‘1’ and BLB is made ‘0’. After this word line is asserted to enable a write operation. The value on the bit line will be written to the device. This written value will be available at the output pin (Q and QB). During write ‘0’, the above operation repeats with the initial value on BL as ‘0’. The BL will be pulled down to ‘0’ by the pull-down transistors.

Read Mode: During the read operation, the bit lines are pre-charged to VDD/2. Later based on the stored value, the BL is either pulled down to the ground or pulled up to VDD by the NMOS or PMOS transistor respectively. The ratio of the pull-down transistor width to that of the access transistors width must be high for better read stability.

2.0 Proposed NVSRAM Design

Different models used to design Memristor are Linear Ion Drift Model, Non-Linear Ion Drift Model, Simmons Tunnel Barrier Model, Threshold Adaptive Memristor (TEAM) Model, and The Voltage Threshold Adaptive Memristor (VTEAM) Model. The VTEAM model has better results for Non-Volatile property because it has better SNM value in the Hysteresis curve. The equation used to design the VTEAM Model [12] is shown in mathematical expression (1).

$$i(t) = \left[R_{ON} + \frac{R_{OFF} - R_{ON}}{w_{off} - w_{on}}\left(w - w_{off}\right)\right]^{-1} . v(t) \tag{1}$$

Which gives I-V relation of the Memristor. Here, R_{ON} and R_{OFF} are the resistance levels of the Memristor, and w_{off} and w_{on} define the boundary of state variable w.

The conventional 6T SRAM Cell is volatile because it doesn’t have any storage element to store the data when the power goes down. To make the SRAM cell as Non-Volatile the resistive NVSRAM cell was introduced called as 7T1R cell. This cell has the Non-Volatile feature, but it suffers from the stability issues and it has higher power consumption due to the resistive component in it. To improve the stability of 7T1R NVSRAM cell, the Memristor based NVSRAM cell known as 7T2M NVSRAM has been designed. It has 7 transistors and 2 Memristors in its architecture. The architecture is shown in Fig. 3.

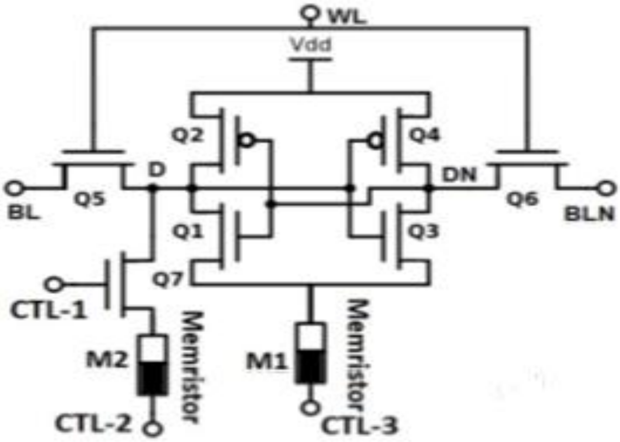

Fig. 3. Circuit structure of 7T2M- NVSRAM cell [5]

The architecture has one basic 6T SRAM cell, two Memristors (M1 and M2), and one pull-down NMOS transistor (Q7). The Memristor M1 positive terminal is connected to the source of transistor Q1 and Q3. The negative terminal of the Memristor is connected to the control input C3. In this architecture, there will be less power dissipation because bistable element is connected to Memristor M1instead of ground.

The Memristor M1 resistance states are changed using the control input pin C3. To keep M1 in HRS mode, the C3 value should be logic 1. To keep M1 in LRS mode, the C3 value should be logic 0. The output voltage swing of the NVSRAM cell depends on the HRS and LRS mode. The Memristor M2 is included in the design for the Non-Volatile operation of the 7T2M NVSRAM cell. The positive terminal of the Memristor M2 is connected to the source of pull-down transistor Q7 and the negative terminal is connected to the control input pin C2. The gate terminal of MOSFET is given to control input C1 and the drain of the transistor is connected to the output node of the SRAM cell. This Memristor is used as a Non-Volatile storage element for the SRAM since it stores the logic value of the output node of SRAM when the power goes down and when the power comes back it will restore to the output node value.

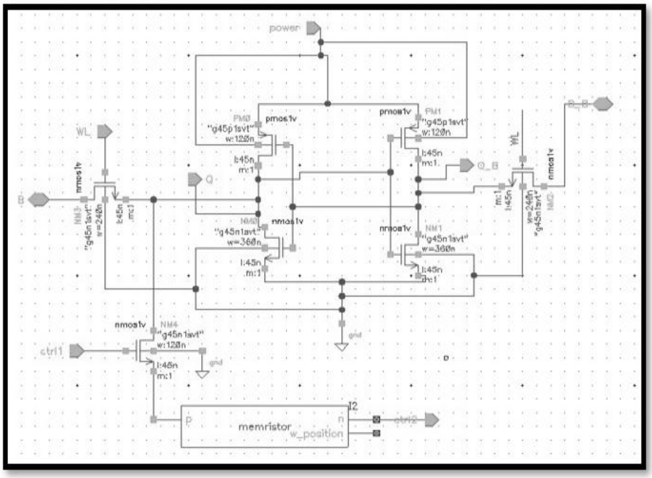

Fig. 4. Circuit structure of proposed 7T1M-NVSRAM cell

The proposed 7T1M-NVSRAM cell is shown in Fig. 4 and it operates in the following modes.

Write 1 mode: In this mode both the control input pins C1 and C2 are made off (logic 0) and the logic 1 value is written on to the memory cell by the bit line through access transistors. The Memristor logic storage action will not take place in this mode as control pin C1 has terminated the connection between the output line and the Memristor.

Store 1 mode: In this mode, the control input C1 is made logic 1 that turns on the transistor connected to the Memristor and the control input C2 is kept at logic 0. Now the Memristor has got the path to output node Q and the logic 1 value will be stored in the Memristor.

Power down mode: In this mode, the power supply (V_{DD}) in the circuit is made 0. Thus, the source of the PMOS transistor is connected to logic 0 and the output node Q goes down to logic 0. During this operation, the control inputs C1 and C2 are kept at 0 to make sure that Memristor is holding the previous output data value.

Restore 1 mode: In this mode, the power supply is made high i.e. logic 1. The control inputs C1 and C2 are made logic 1. The Memristor writes the previously stored logic 1 value onto the memory cell output node Q. Thus, the memory cell has been successfully got restored the value after the power-down operation.

Similarly, if the output node value is at logic 0 then we perform the same store, power down, and restore operations. But during restoring logic 0, the visual representation of output changing to 0 will not be there because of previous power-down operation. During power-down mode, the output node will be zero. So, restoring 0 after power-down mode does not have any impact on the output graph.

MTCMOS is the power reducing technique used in the CMOS designs to optimize the total power consumed in the circuit [13-16]. In this technique, two additional transistors called sleep transistors are introduced one at the top and the other at the bottom of the circuit. Both upper and lower transistors have complementary inputs. The upper transistor has a sleep input and the lower transistor has a sleep bar input. The transistors are made off during sleep or standby mode and the low Vt logic will be separated from the VDD and ground. Hence very less subthreshold current will be flowing in the circuit[17-18]. Thus, it reduces the total power consumption of the circuit. Fig. 5 shows the implementation of MTCMOS based 7T1M NVSRAM cell.

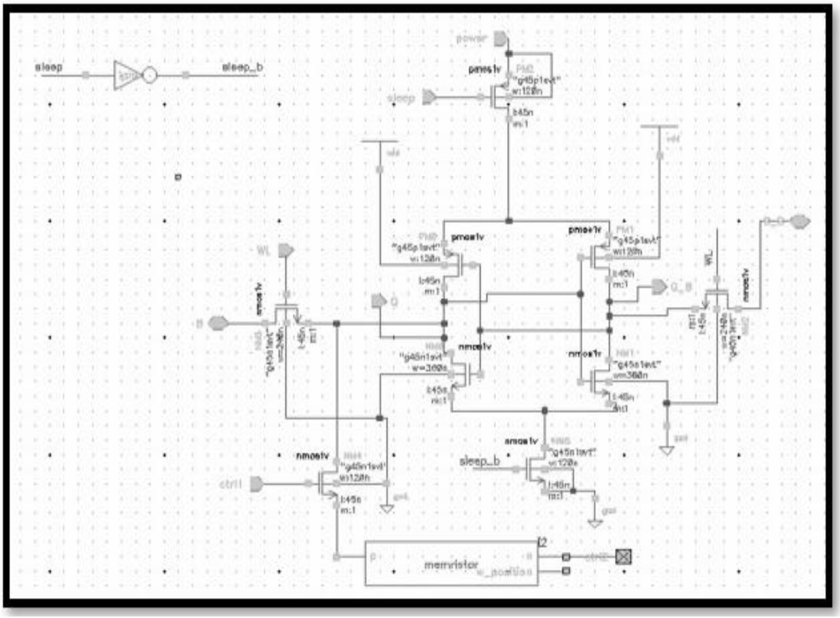

Fig. 5. Circuit structure of proposed 7T1M-NVSRAM cell with MTCMOS technique

3.0 Results and Discussion

The steps followed to get the Memristor hysteresis curve were:

1. Mathematical models such as Simmons Tunneling Model, Non-Linear Ion Drift Model, TEAM model, and VTEAM model were tried to get a better hysteresis loop for the Memristor. The VTEAM model provided a better hysteresis curve for the lower operating voltage of 1.2 V.
2. The Memristor model is designed in Cadence Virtuoso tool using Verilog-A code.
3. The symbol of the Memristor is created and obtained the hysteresis curve for operating voltage of 1.2V.
4. The obtained I-V curve of Memristor is shown in Fig. 6.

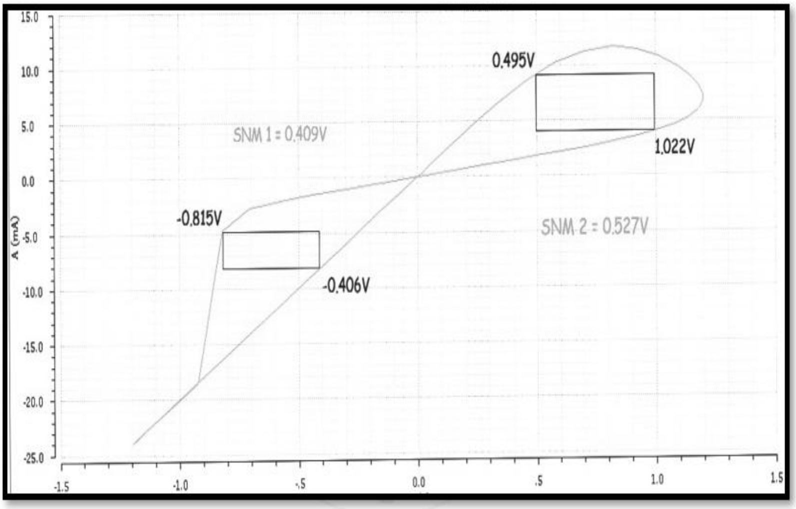

Fig. 6. Hysteresis curve of Memristor

The butterfly curve of the Memristor has two lobes with two different SNM's for each lobe. The SNM is the amount of noise voltage that the device can handle without distorting its output value. The minimum SNM of those two lobes is the SNM of the Memristor. Here SNM1 is 0.409V and SNM2 is 0.527V and hence SNM of the Memristor is 0. 409V. Table 1 depicts the parameters used for creating the Memristor model.

Table 1. Simulation Parameters of a Memristor

Parameters	**Values**
HRS(Roff) (kΩ)	62.5
LRS(Ron) (Ω)	50
Aoff	5
Aon	2
Voff (V)	0.02
Von (V)	-0.2
Woff (nm)	3
Won (nm)	0

Fig. 7 shows the operation of the 6T SRAM cell. When pre-charge is 0, the bit and bit bar line get charged to VDD/2. When the write/read bar is 0, SRAM is in the read mode and the bit line reads the content of the output line when the word line is asserted. When the write/read bar is made high the SRAM is in write mode. It writes data onto the memory when the word line is asserted.

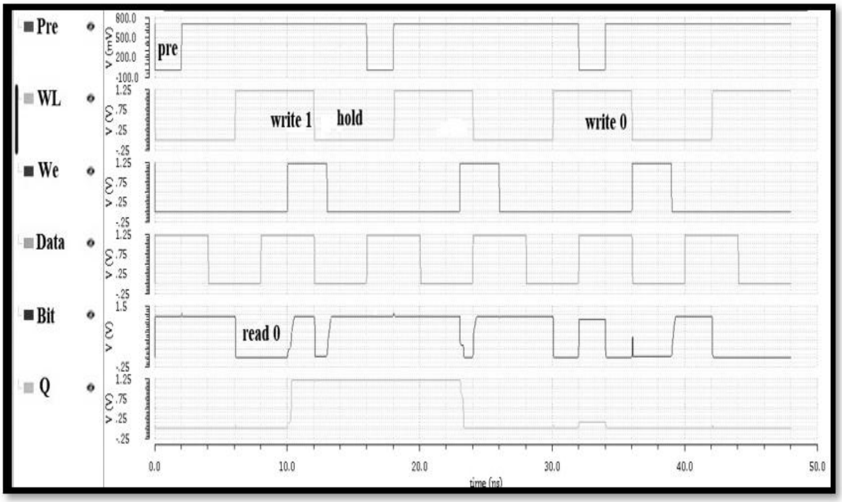

Fig. 7. Read and write operations of a 6T SRAM

Fig. 8 shows the hysteresis curve of the 6T SRAM cell. SNM of the cell can be calculated by Min (SNM1, SNM2). Hence, SNM of the 6T SRAM cell is 0.502V. Fig. 9 shows the hysteresis curve of a 7T2M Non-Volatile SRAM cell. The SNM of 7T2M architecture is 40mV. This architecture will improve the stability of the cell but the SNM of the cell is very less. The proposed 7T1MNVSRAM architecture will improve the SNM of the cell.

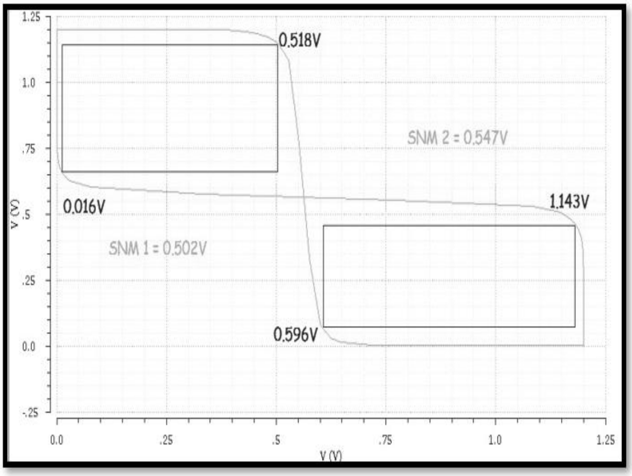

Fig. 8. Hysteresis curve of 6T SRAM

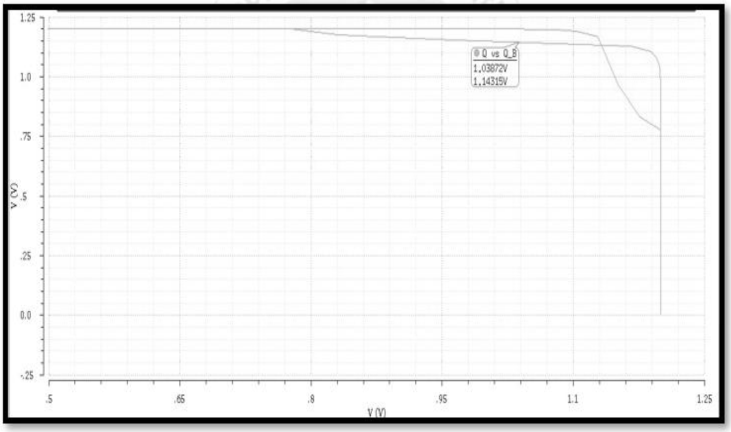

Fig. 9. Hysteresis curve of a 7T2M-NVSRAM cell

7T1M NVSRAM cell Read and Write operations can be analyzed in four modes namely Write, Store, Power down, and Restore modes. During Write 1 mode, the SRAM will store the logic 1 value and the memristive action will not take place in this mode. During Store 1 mode, the Memristor stores the logic 1 value. During Power down mode, the power supply is made zero so that the output of SRAM cell goes to logic 0. During Restore 1 mode, the Memristor will help to restore the output node value to logic 1. The Fig. 10 shows the output operation of the 7T1M NVSRAM cell. Fig. 11 shows the hysteresis curve of the 7T1M-NVSRAM cell. The SNM of the 7T1M-NVSRAM cell is 0.518V.

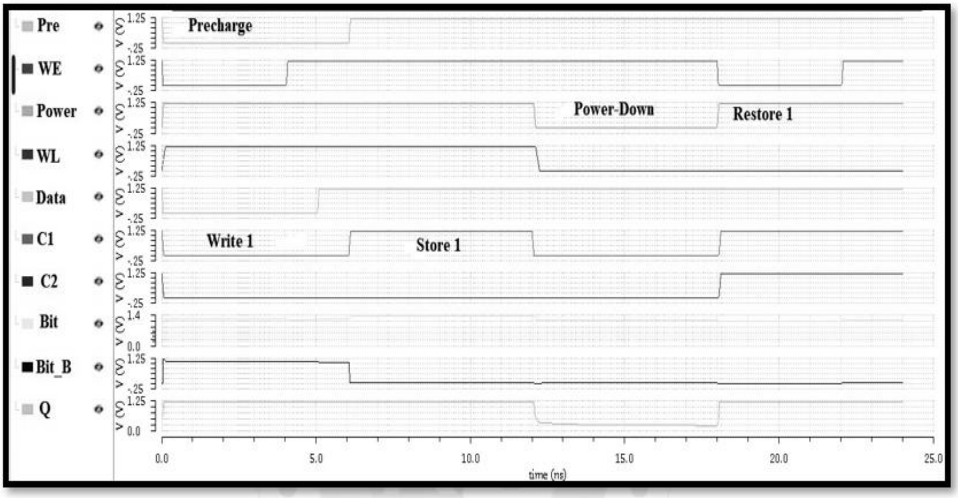

Fig. 10. Read and write operations of a proposed 7T1M-NVSRAM cell

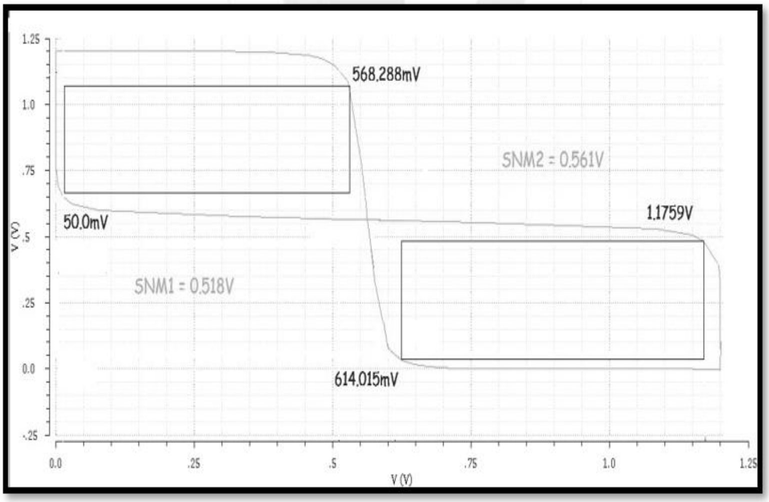

Fig. 11. Hysteresis curve of proposed 7T1M-NVSRAM cell

The proposed 7T1M-NVSRAM cell, 7T2M-NVSRAM cell, and 6T SRAM structures were simulated in the Cadence Virtuoso tool at 45nm technology, and various performance parameters such as Read Access Time (RAT), Write Access Time (WAT), power and SNM are measured. The RAT of the proposed 7T1M-NVSRAM is optimized so that it requires lesser time to perform the read operation compared to 7T2M-NVSRAM cell and also WAT required for both the architecture are almost similar. The obtained values of SNM for 6T SRAM, 7T2M-NVSRAM, and proposed 7T1M-NVSRAM are 0.502V, 0.04V, and 0.518V respectively. This shows that the Proposed 7T1M-NSRAM has a higher SNM value compared to 7T2M-NVSRAM and 6T SRAM. The power value of 7T1M is slightly higher because the NMOS transistors of the 6T SRAM cell are directly connected to the ground. The power can be optimized by using power optimization techniques like MTCMOS and SVL techniques. The comparison of the performance parameters of a different architecture is listed in Table 2.

Table 2. Comparison of Results

Design Specifications		6T SRAM Cell	7T2M NVSRAM	Proposed7T1M NVSRAM
Read Access Time	Restore 0	0.054nS	0.154nS	0.150nS
	Restore 1	0.037nS	0.50nS	0.124nS
Write Access Time	Write 0	0.260nS	0.145nS	0.167nS
	Write 1	0.272nS	0.145nS	0.161nS
Power		9.33uW	23.05uW	38.31uW

PDP (Power DeLay Product)	2.48 fsW	5.439 fsW	5.765 fsW
SNM	0.502V	0.04V	0.518V
Area (Number of circuit elements used)	6 Transistors	7 Transistors, 2 Memristor	7 Transistors, 1 Memristor

4.0 Conclusion

In this paper, the 7T1M NVSRAM cell is proposed by integrating one Memristor and one pull-down transistor for the conventional 6T SRAM. The VTEAM Model-based Memristor has been designed and obtained a higher SNM value of 0.409V. The proposed NVSRAM cell has been compared with 7T2M NVSRAM cell for Power, Delay, SNM, and Area. The Read and Write Access time of both the architectures are almost same with the compromise of power. The power reduction technique MTCMOS is employed to the proposed NVSRAM cell to reduce the power consumption of the cell. The proposed 7T1M NVSRAM cell has the SNM of 0.518V, whereas the 7T2M NVSRAM cell has the SNM of 0.04V. The 7T2M architecture uses two Memristors whereas the proposed 7T1M NVSRAM cell has only one Memristor. Therefore, the proposed NVSRAM cell has a better SNM value and lesser area when compared to the existing 7T2M NVSRAM cell.

References

1. F Wang, M Hamdi, Matching the speed gap between SRAM and DRAM, *IEEE* International Conference on High Performance Switching and Routing, ISBN: 978-1-4244-1982-1,Shanghai, China, May 2008

2. Wasir Singh, Design of 6T, 5T and 4T SRAM Cell on Various Performance Metrics, *2nd IEEE International Conference on Computing for Sustainable Global Development (INDIACom)*, ISBN: 978-9-3805-4416-8, New Delhi, India, March 2015

3. Yanan Sun, Jiawei Gu, Weifeng He, Qin Wang, Naifeng Jing, Zhigang Mao, Weikang Qian, and Li Jiang, Energy-Efficient Nonvolatile SRAM Design Based on Resistive Switching Multi-Level Cells, *IEEE Transactions on Circuits and Systems II,* 66 (5), 753 – 757, May 2019

4. C Chinmay, Mahantesh S Kenchannavar, A Tejaswini, B S Kariyappa, VTEAM Model Based In-Memory Computation using Memristors, *International Journal of Innovative Technology and Exploring Engineering (IJITEE),* 9 (1), ISSN: 2278-3075, 3426-3432, October 2019

5. Jeetendra Singh, Balwinder Raj, Design and Investigation of 7T2M-NVSRAM With Enhanced Stability and Temperature Impact on Store/Restore Energy, *IEEE Transactions on Very Large Scale Integration (VLSI) Systems*, 27 (6), 1322 – 1328, June 2019

6. Naman S Kumar, N G Sudhanva, V Shreyas Hande, Mallikarjun V Sajjan, C S Hemanth Kumar, B S Kariyappa, SRAM design using Memristor and Self-controllable Voltage (SVL) Technique, *International Conference on Computational Intelligence & Data Engineering (ICCIDE 2017) Vijayawada*, Andhra Pradesh, July 2017
7. D B Strukov, G S Snider, D R Stewart, R S Williams, The missing Memristor found, *Nature,* 453, 80–83, 2008
8. S Kvatinsky, E G Friedman, A Kolodny, U C Weiser, The desired Memristor for circuit designers, *IEEE Circuits Systems,* 13, 17–22, 2013
9. Matthew D Pickett, Dmitri B Strukov, Julien L Borghetti, J Joshua Yang, Gregory S Snider, Duncan R Stewart, R Stanley Williams, Switching dynamics in titanium dioxide memristive devices, *Journal of Applied Physics,* 106 (074508), October 2009
10. R Venkatraman, R Castagnetti, O Kobozeva, F L Duan, A Kamath, S T Sabbagh, M A Vilchis-Cruz, J.J. Liaw, Jyh-Cheng You, S. Ramesh, The Design, Analysis, and Development of Highly Manufacturable 6-T SRAM Bitcells for SoC Applications, *IEEE Transactions on Electron Devices,* 52 (2), 218-226, Febraury 2005
11. Wei Wei, Kazuteru Namba, Jie Han, Fabrizio Lombardi, Design of a Non-Volatile 7T1R SRAM Cell for Instant-on Operation, *IEEE Transactions on Nanotechnology*, 13 (5), 905-916, September 2014
12. Shahar Kvatinsky, Misbah Ramadan, Eby G Friedmanand Avinoam Kolodny, VTEAM: A General Model for Voltage-Controlled Memristors, *IEEE Transactions on Circuitsand Systems,* 62 (8), 786-790, August 2015
13. C S Hemanth Kumar, B S Kariyappa, 7T Based SRAM Topologies with Low Power and Higher SNM, *International Journal of Innovative Technology and Exploring Engineering (IJITEE),* ISSN: 2278-3075, 8 (11), 2779-2783, September 2019
14. C S Hemanth B S Kariyappa, Analysis of Low Power 7T SRAM Cell Employing Improved SVL (ISVL) Technique, *IEEE International Conference on Electrical, Electronics, Communication, Computer and Optimization Techniques (ICEECCOT-17), Mysore,* ISBN: 978-1-5386-2361-9, 478-482, December 2017
15. Neha Gupta, Hitesh Pahuja, Balwinder Singh, Navneet Nagpal, A Novel Design of Low Power Nonvolatile 10T1R SRAM Cell, *IEEE Fifth International Conference on Wireless Networks and Embedded Systems (WECON)* ISBN : 978-1-5090-0893-3 Rajpura, India, October 2016
16. Vijay Singh Baghel, Shyam Akashe, Low power Memristor Based 7T SRAM Using MTCMOS Technique, *IEEE Fifth International Conference on Advanced Computing & Communication Technologies, Haryana, India.* ISBN: 978-1-4799-8488-6, February 2015

17. J Mounica, G V Ganesh, Design of a Nonvolatile 8T1R SRAM Cell for Instant-On Operation, *International Journal of Electrical and Computer Engineering (IJECE)*, 6 (3), 1183 – 1189, June 2016

18. Reena S Wasankar, Ashish E Bhande, U A Kshirsagar, Design of Power Efficient Memristor Based SRAM Using MTCMOS Technique, *International Journal of Innovative Research in Computer and Communication Engineering*, 4, April 2016, DOI: 10.15680/IJIRCCE.2016.0404137

Smart and Interactive Features for Lane Detection

Suhas N Bhargav[1], Rajani Katiyar[1*]

[1]Department of Electronics & Communication Engineering, RV College of Engineering®,
Bengaluru

Abstract

The advent of newer and more sophisticated automobiles has greatly pushed the performance limits in terms of speed and maneuverability. However, this has greatly increased the risk of driver losing control over their car, resulting in accidents. Many techniques have been proposed in the past that addresses this concern by limiting the movement of the car to a particular lane only. Practical implementation of such systems demands highly capable hardware like TDA3x which can perform real-time processing. The efficiently designed code helps the individual tasks to run and complete on a particular processor core independent of what the other core is doing. The main emphasis given in this paper is to implement the Lane Detection and Warning System (LDWS) on a Texas Instruments Driver Assist 3x (TDA3x) board with a frame resolution of (1920×1080p) at 2GHz, compared to the existing implementation that provide a resolution of just (480*270p) at 100MHz.The work proposed in the paper is to detect the lane for any range of camera height to road width ratio between [0.3 to 0.8] Since the standard ratio on Indian roads is approximately 0.524, the proposed algorithm would work well under the given idealistic road conditions in India.

Keywords: *Lane Detection and Warning System (LDWS), Canny edge detection, Hough transforms, Vanishing point estimates, Principal component analysis, TDA3x*

1.0 Introduction

There can be various reasons for an accident to occur on the road. There are also circumstances where the accident occurs due to sheer negligence on part of the person controlling the vehicle. To overcome this problem there is a need for an autonomous system designed and implemented inside the vehicle which work independent of the person controlling the vehicle. The advantage of having such setup of autonomous system inside the car is that they will be able to identify the errors committed by the driver and also predict the possible collisions. This will not only alert the driver on his mistakes, but also help him to overcome such mistakes by taking corrective actions, on-time.

Among the many applications that the autonomous systems can provide, implementation of Lane information detection (LID) is proposed in this paper. In this application (LID) camera is placed on the bonnet of the car captures the

---

**Mail address: Rajani Katiyar, Assistant Professor, Dept. of Electronics & Communication Engg, RV College of Engineering®, Bengaluru – 59*
Email: rajanikatiyar@rvce.edu.in, Ph: 9036902505

video frames, and then extracts the information related to the lane markings that are laid on the road. Based on the available information, the movement of the vehicle will be tracked, and a suitable warning shall be issued to the driver in advance. This will not only alert the driver, but also help to avoid the possible collision before it is too late to respond for the driver.

In the past, lot of research ideas were proposed by various authors in the field of vehicle safety. Detection of the lanes based on the fact that lines which are drawn on the road will be thick in nature; the individual lane markings have a non-zero width [1]. The work proposed [2] focus on increasing the processing speeds than on the accuracy of lane detect system by reducing the resolution of the captured image. Papers [3-4] focused on the noise aspect of the image to enhance the quality and also performed illumination adaptability for adjusting to various lighting conditions on the road. Authors in [5] highlights the specific bottlenecks in the existing techniques, such as the obstruction caused by the presence of vehicles, unclear markings of the lane, shadow obstructions due to buildings, etc. Authors [6] and [7] also worked on solving the issue of poor visibility of the lanes at hilly regions due to the dynamic weather conditions such as rain, fog, haze, etc that are prevalent. Work proposed in [8] perform lane detection based on vision processing, where techniques such as perspective mapping, deep neural networks, vanishing point estimates, and other mathematical models were used.

However, to implement the proposed idea in real time, there is a requirement for a suitable hardware which is capable of supporting the highly complex algorithms that takes up a huge computational time. Also, these kinds of applications demand for the use of highly optimized hardware that can allow the real-time processing of the captured images. Texas Instruments has developed a hardware called “TDA3x” whose whole purpose is to support the implementation of the Advanced Driver Assistance Systems (ADAS) applications. In this work, the entire operation of the lane detection and warning system is divided into smaller tasks, with each task allocated or made to run on a different processor. Thus, the efficiently designed code helps the individual tasks to run and complete on a particular processor core independent of what the other core is doing.

2.0 System Development

Real-time processing of the applications will be possible only when the hardware which it uses is capable enough to provide support for high speed processing. The work proposed in the paper used TDA3x hardware for implementation of lane info system. The figure 1 depicts the block diagram for the same. To implement the lane info system, an ISS OV10640 omni vision camera is used to capture the video frames which is then connected to the board via CSI2 interface. Also, the developed application code is dumped into the board by flashing it through a SD card. Hence, every time a code is modified, it needs to be re-flashed into the board. Here, the detected lanes and in turn the lane cross warning is displayed to the end user through the use of a HDMI LCD display.

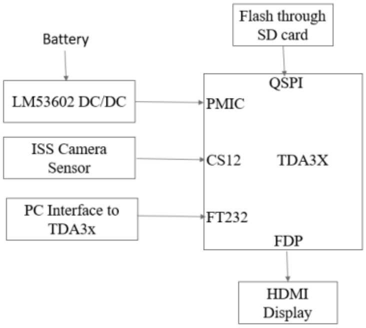

Fig. 1. Block Diagram of Lane Detection and Warning System (LDWS)

TDA3x board works on a supply of 12V. Since the car's battery can generate a voltage drop of 12V across its terminal, this lane info system can be easily setup inside the car.

2.1 Methodology adopted

This section gives details information about the methodology adopted for the proposed algorithm used for lane detection system. The fig. 2 depicts the flowchart of the steps that needs to be accomplished for the same.

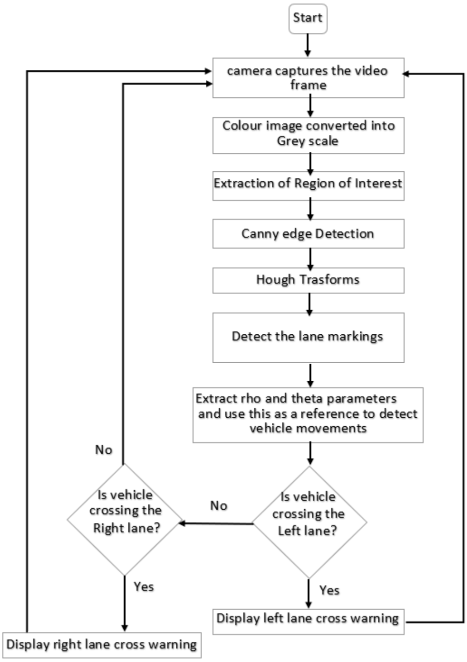

Fig. 2. Flowchart for the LDWS Lane Detection and Warning System (LDWS)

When a camera captures a video stream, it should be converted into a grey scale image as canny edge detection can only operate only on the monochrome images. The extraction of Region of Interest (ROI) boundary helps to limit the search area of the algorithm and hence eliminates any unwanted details from the captured image. Though canny edge detection helps to identify the lane edges in the input image, Hough transforms will help to generate a mathematical relationship between those edge points, be it a straight line, a parabola, or a circle. Hough transforms will also help to extract the polar equivalents of the obtained lane coordinates to help track the position of the lane with respect to the test vehicle. By incorporating all the algorithms mentioned above, any accidental lane drifts by the car can be easily identified and suitable action can be taken by the system.

2.2 Experimental details

The government bodies (RTO) who paint the lanes on the road will ensure that they always run parallel to each other. However, the way a camera looks at these lanes in reality will be quite different. As the camera is placed parallel to the road surface, the lanes in front of the car appears to look like a trapezoid, instead of a rectangle. As a result, the lane boundary near the camera appears to be thick, while it looks thin at the far end. The fig. 3 depicts this phenomenon.

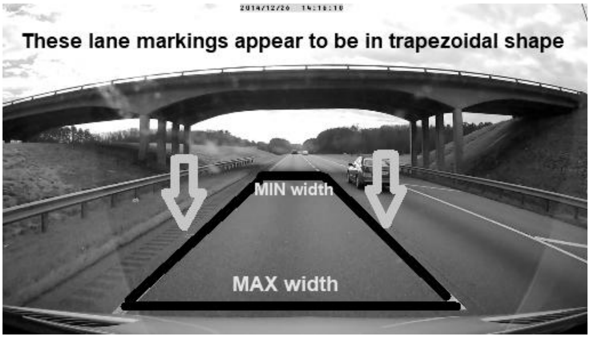

Fig. 3. Viewpoint of the camera

For the Lane Detection and Warning System (LDWS) to identify the trapezoid, the four extreme vertices of this trapezoid needs to be determined first. This is done by extracting the information of the lane points at the output of the Hough Transforms block. The fig. 4 depicts the pictorial representation of the trapezoid.

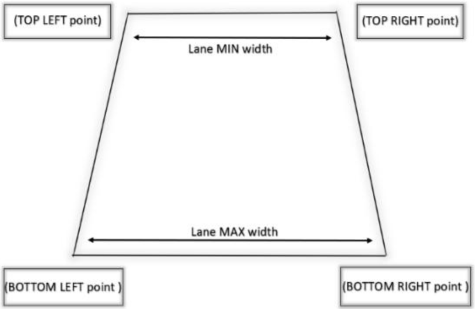

Fig. 4. Pictorial representation of the trapezoid

Once the 4 vertexes are obtained, 2-point formula can be used to generate the equation of a line and in turn identify the lane markings. Suppose that there exists any two points in space, (x_1,y_1)& (x_2,y_2). To extract the polar counterparts (rho and theta) from the given straight line, a perpendicular line has to be drawn from the origin to the line. This is shown in the fig. 5.

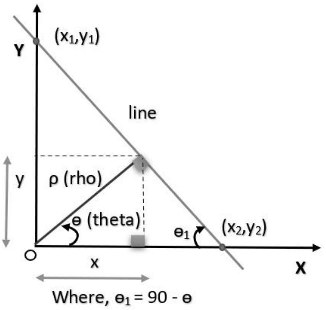

Fig. 5. Extraction of polar counterparts from a line

The pictorial representation of the lane under normal condition is shown in fig. 6. Here, “ө$_1$” denotes the angle subtended by the left lane while “ө$_2$” denotes the angle subtended by the right lane. Similarly, “ρ1” denotes the magnitude of the perpendicular to the left lane and “ρ2” denotes the magnitude of the perpendicular to the right lane. When the car is moving well inside the current lane, it is said to be in normal condition.

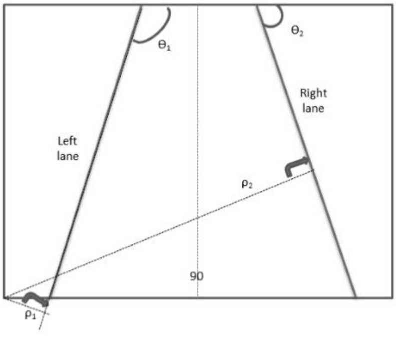

Fig. 6. Pictorial representation of the lane under normal condition

When the car drifts to the left, then the angles subtended by both the lanes will decrease, while magnitude of the perpendicular to the left lane increases and magnitude of the perpendicular to the right lane decreases. The fig. 7 depicts the above criteria.

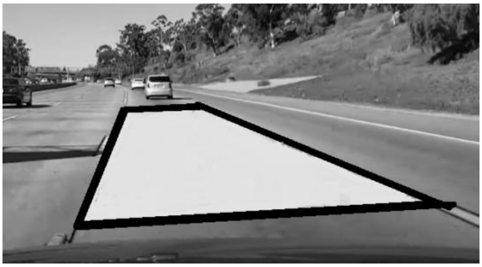

Fig. 7. Pictorial representation of the lane under left lane drift

Similarly, When the car drifts to the right, then the angles subtended by both the lanes will increase, while magnitude of the perpendicular to the left lane decreases and magnitude of the perpendicular to the right lane increases. The fig. 8 depicts the above criteria.

Fig. 8. Pictorial representation of the lane under right lane drift

The above concepts will be used to obtain the results for the proposed lane info system.

3.0 Results and Discussion

Based on the concepts that were discussed in the previous sections, screenshots of the obtained result are shown, followed by their detailed analysis. The fig. 9 depicts the screenshot of the detected lanes under normal condition.

Fig. 9. Screenshot of the detected lane under normal condition

The fig. 10 depicts the screenshot obtained during the left lane cross warning, and the fig. 11 depicts the screenshot obtained during the right lane cross warning.


*** LEFT LANE CROSS ***, 2

Fig. 10. Screenshot obtained during left lane cross warning


RIGHT LANE CROSS ###, 1

Fig. 11. Screenshot obtained during right lane cross warning

The above experiment was also conducted by making use of a carboard sheet and a cello tape to mimic the lane markings on the road. The output was analyzed for various configurations of the camera parameters, and the resulting readings were tabulated, as shown in the table 1 and table 2. It is important to note that all these seven values are user configurable. Based on the parameters in table 1, the efficiency of the lane info system can be altered. This is because, when the car is moving inside the lane, it has some set of (Rho & Theta) values for the left and the right lanes.

Table 1. Lane cross warning results

Sl. No	Left theta (max, min) in degrees	Right theta (max, min) in degrees	Left rho (max, min)	Right rho (max, min)	Type of road (single/ double lane	camera angle w.r.t vertical axis	Lane cross warning results
1	130, 126	46, 45	140, 133	151, 150	Single	0	Left/right warnings correctly observed
2	130, 126	46, 45	140, 133	151, 150	Double	0	Left/right warnings correctly observed
3	130, 126	46, 45	140, 133	151, 150	Double	30 deg to the right	Left lane cross is detected with difficulty. Right lane cross is detected easily
4	127, 126	41, 40	140, 139	151, 145	Single	30 deg to the right	Left lane cross is detected with difficulty. Right lane cross is detected easily
5	127, 126	41, 40	140, 139	151, 145	Single	30 deg to the left	right lane cross is detected with difficulty. left lane cross is detected easily
6	127, 120	41, 39	149, 139	151, 150	Single	0	Left lane cross is detected with difficulty. Right lane cross is detected unreliably
7	130, 126	46, 45	140, 133	152, 150	Single	0	Left/right warnings correctly observed

Now, when the car tries to drift across the left/right lane, depending on the direction of the drift, even the (Rho & Theta) values also change.As a result, the algorithm continuously monitors the obtained values with the (MAX, MIN) threshold pairs that have been set by the user prior to the experiment. So, effectively the algorithm issues a left/right lane cross warning to the end user when the real time (Rho/Theta) values exceed the above threshold values.

The readings for various parameters of the camera is shown in Table 2. After analyzing the obtained readings from the table 2, it can be concluded that the performance of the proposed application depends on the relative difference between the height of the camera and the width of the road. As the ratio between these two values keep increasing, then it gets more and more difficult for the lane info system to detect the lanes correctly. At the same time, when the ratio gets too low of a value, then the lane markings on the road cannot be detected accurately. This is because, in both the cases, lanes in the captured image goes well beyond the processing range of the algorithm.

Table 2. Readings for various parameters of the camera [17]

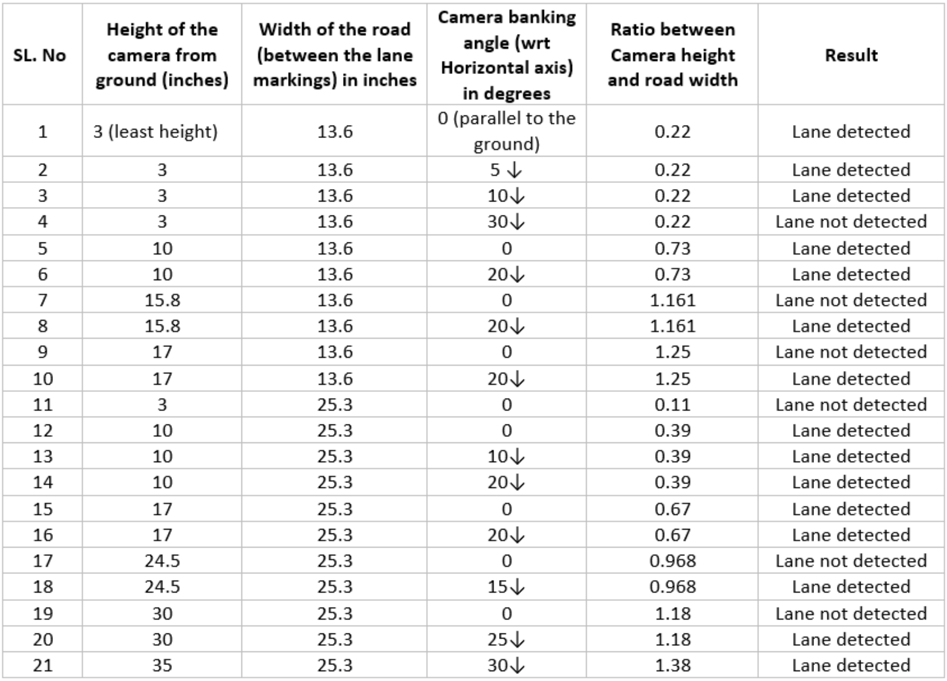

SL. No	Height of the camera from ground (inches)	Width of the road (between the lane markings) in inches	Camera banking angle (wrt Horizontal axis) in degrees	Ratio between Camera height and road width	Result
1	3 (least height)	13.6	0 (parallel to the ground)	0.22	Lane detected
2	3	13.6	5 ↓	0.22	Lane detected
3	3	13.6	10↓	0.22	Lane detected
4	3	13.6	30↓	0.22	Lane not detected
5	10	13.6	0	0.73	Lane detected
6	10	13.6	20↓	0.73	Lane detected
7	15.8	13.6	0	1.161	Lane not detected
8	15.8	13.6	20↓	1.161	Lane detected
9	17	13.6	0	1.25	Lane not detected
10	17	13.6	20↓	1.25	Lane detected
11	3	25.3	0	0.11	Lane not detected
12	10	25.3	0	0.39	Lane detected
13	10	25.3	10↓	0.39	Lane detected
14	10	25.3	20↓	0.39	Lane detected
15	17	25.3	0	0.67	Lane detected
16	17	25.3	20↓	0.67	Lane detected
17	24.5	25.3	0	0.968	Lane not detected
18	24.5	25.3	15↓	0.968	Lane detected
19	30	25.3	0	1.18	Lane not detected
20	30	25.3	25↓	1.18	Lane detected
21	35	25.3	30↓	1.38	Lane detected

If at all, the user wants to still be able to detect the lanes correctly at higher ratios, then the camera needs to be titled downwards by a small angle such that it no longer is parallel to the road surface. The placement of the camera will remain universal across all the brands of the car until it satisfies a particular criterion that the ratio between the camera height and the road width remains within the range (0.3 to 0.8). The proposed system can work for cars of any dimension. When the ratio goes beyond 0.8, the algorithm can be still made to work by changing the camera angle. The very nature of the proposed system makes it scalable and also portable.

4.0 Conclusions

The existing techniques that implement the lane information detection on the Xilinx's Zynq-7000 APSoC platform supports only a resolution of (480×270p) at 100MHz [16]. Whereas, the TDA3x board used in the proposed work supports a full HD resolution of (1920×1080p) at 2GHz. Hence, the lane markings from the captured video streams will be sharper and the detected edges will be highly accurate. Also, due to the higher frequency of operation, there will be no cluttering of the video streams during run-time.

The speed of the vehicle should not matter until the lane markings are clearly captured by the camera. If the captured image of the camera appears blurred due to potholes, humps or even sudden jerks, or even due to the obstacle ahead of the test vehicle, then this algorithm will not be able to work as expected. The above work has not been tested for the application on a curved road. It has only been tested on a straight road. Hence, the lane info system may not be able to work on sharp bends (as seen on hilly roads). However, considering the fact that the regular highways in our country have relatively lower curve gradients compared to the hilly roads, algorithms mention in paper can work satisfactorily.

The authors would like to thank Mr. Ameermon V A, senior staff Engineer, Ignitarium Technology solutions Private Limited, for his constant support and encouragement throughout.

References

1. Ganlu Deng, Yefu Wu, Double Lane Line Edge Detection Method Based on Constraint Conditions Hough Transform, *17th International Symposium on Distributed Computing and Applications for Business Engineering and Science (DCABES)*, 19-23 Oct. 2018
2. Li Dang, Girma Tewolde, Xiaoyuan Zhang, Jaerock Kwon, Reduced resolution lane detection algorithm, *IEEE AFRICON*, Sept. 2017.
3. Mehdi Feniche, Tomader Mazri, Lane Detection and Tracking for Intelligent Vehicles: A Survey, *International Conference of Computer Science and Renewable Energies (ICCSRE)*, July 2019
4. Alireza Bosaghzadeh, Seidfarbod Seidali Routeh, A novel PCA perspective mapping for robust lane detection in urban streets, *Artificial Intelligence and Signal Processing Conference (AISP)*, Oct. 2017
5. Suvarna Shirke, C Rajabhushanam, A study of lane detection techniques and lane departure system, *International Conference on Algorithms, Methodology, Models and Applications in Emerging Technologies (ICAMMAET)*, Feb. 2017
6. Kodeeswari Manoharan, Philemon Daniel, A Robust Approach for Lane Detection in Challenging Illumination Scenarios, *International Conference on Advances in Computing, Communication Control and Networking (ICACCCN)*, Oct. 2018
7. Nima Zarbakht, Ju Jia Zou, Lane Detection under Adverse Conditions Based on Dual Color Space, *Digital Image Computing: Techniques and Applications (DICTA)*, Dec. 2018
8. Xuqin Yan, Yanqiang Li, A method of lane edge detection based on Canny algorithm, *Chinese Automation Congress (CAC)*, Oct. 2017
9. Yueen Ma, Vincent Havyarimana, Jing Bai, Zhu Xiao, Vision-Based Lane Detection and Lane-Marking Model Inference: A Three-Step Deep Learning Approach, *9th International Symposium on Parallel Architectures, Algorithms and Programming (PAAP)*, Dec. 2018

10. Van-Quang Nguyen, ChangjunSeo, Heungseob Kim, Kwangsuck Boo, A study on detection method of vehicle based on lane detection for a driver assistance system using a camera on highway, *11th Asian Control Conference (ASCC),* Dec. 2017
11. Huifeng Wang, Yunfei Wang, Xiangmo Zhao, Guiping Wang, He Huang, Jiajia Zhang, Lane Detection of Curving Road for Structural Highway with Straight-Curve Model on Vision, *IEEE Transactions on Vehicular Technology*, 68 (6), 5321–5330, 2019
12. Chung-Bin Wu, Li-Hung Wang, Kuan-Chieh Wang, Ultra-Low Complexity Block Based Lane Detection and Departure Warning System, *IEEE Transactions on Circuits and Systems for Video Technology*, 29 (2), 582 – 593, 2019
13. Yang Xing, Chen Lv, Long Chen, Huaji Wang, Hong Wang, Dongpu Cao, Efstathios Velenis, Fei-Yue Wang, Advances in Vision-Based Lane Detection: Algorithms, Integration, Assessment, and Perspectives on ACP-Based Parallel Vision, *IEEE/CAA Journal of Automatica Sinica*, 5 (3), 645 - 661, 2018
14. Chanho Lee, Ji-Hyun Moon, Robust Lane Detection and Tracking for Real-Time Applications, *IEEE Transactions on Intelligent Transportation Systems,* 19 (12), 4043 – 4048, 2018
15. Yingna Su, Yigong Zhang, Tao Lu, Jian Yang, Hui Kong, Vanishing Point Constrained Lane Detection with a Stereo Camera, *IEEE Transactions on Intelligent Transportation Systems*, 19 (8), 2739-2744, 2018
16. Chanon Khongprasongsiri, Pinit Kumhom, Watcharapan Suwansantisuk, Teerasak Chotikawanid,Surachate Chumpol, Masami Ikura , A Hardware Implementation for Real-Time Lane Detection using High-Level Synthesis, *International Workshop on Advanced Image Technology (IWAIT),* Jan. 2018.
17. Suhas N Bhargav, Rajani Katiyar, Advanced Driver Security Application, *International Journal of Engineering and Advanced Technology (IJEAT)* ISSN: 2249 – 8958, 9 (4), April 2020

Optimal Load Balancing Strategy in a Virtual Environment

Sahana B[1], Abhay Deshapande[1*], AV Sruthi[1], Deekshith KN[1], Diksha Dinesh[1]

[1]*Department of Electronics and Communication Engineering, RV College of Engineering®, Bengaluru*

Abstract

In a virtual environment, load balancing is the method of assigning a collection of tasks through a range of resources, in order to make their total functionality more efficient. Load balancer is used to increase the device efficiency for the user, and overall service stability at the same time. Resource allocation in a virtual environment, in this paper, is accomplished using Amazon Web Services (AWS) as the basis for our virtual environment. Amazon Relational Database Services (RDS) supports high storage capacity and scalability. HAProxy performs the duties of a Load Balancer, by allocating incoming requests amongst the virtual servers. The virtual servers, which are created by setting up Amazon Elastic Computer Cloud (EC2) instances have same properties such as load bearing capacity and reaction time. One of the EC2 instances is configured to host HAProxy as the load balancer. The load bearing potential of HAProxy is inversely proportional to the execution time, ensuring faster processing of the incoming requests. The proposed model is highly efficient, as it is noticed that the number of user increases the execution time varies by small amount. For up to 5 users the average execution time is 0.690 ms whereas for the user range of 20-25 the average execution time is 0.801 ms. For a scenario where the web servers differ in terms of load bearing capacity, the algorithm may be modified by assigning weights. HAProxy load balancer optimizes resource allocation and provides flexibility.

Keywords: *Access Log Files, Amazon Relational Database Services (RDS), Amazon Web Services (AWS), Elastic Computer Cloud (EC2) Instances, HAProxy, Virtual Machines VM.*

1.0 Introduction

Cloud computing is an essential technology in today's continuously technically advancing world. Providing different types of user services through internet form the basis of cloud computing. These services include tools and applications like data storage, servers, databases, networking, etc. So long as an electronic user has access to the internet, they have access to the data and software programs needed to operate it. In cloud computing, virtualization means creating a virtual instance of hardware computer systems, disk tools, and

---

**Mail address: Abhay Deshpande, Associate Professor, Department of Electronics and Communication Engineering, RV College of Engineering®, Bengaluru – 59*
Email: abhayadeshpande@rvce.edu.in, Ph.: +91 9980815636

network computing services. A well-known example of virtualization is the drive facility offered by Google which helps millions of users to store and share data. Majority of servers used by companies is based on a pay and use policy. Best examples of cloud providers currently are Google cloud, Microsoft Azure, Amazon Web Services (AWS), Alibaba Cloud, IBM cloud, Salesforce, SAP, etc. The conventional methods of maintaining a server is highly inefficient compared to today's virtual cloud servers. Maintaining large number of physical servers is costly; moreover, not all the servers are used at every point of time. Server usage depends on sent requests. Excessive number of requests leads to overloading of a server, hence causing it to shut down. Using cloud servers overcomes all these problems as large number of servers can be rented for that particular peak time. Based on the number of requests there is always scope for extension, thus avoiding the problem of overloading.

Current developments in virtualization technology have transformed the way computing networks are designed and operated. Nonetheless, virtualization systems have a detrimental impact on the device output predictability, which poses many problems in managing efficiency and resource utilization. Lianjie Cao et al. [1] resolved efficiency issues by defining and modeling resource management task output in two technology scenario: distributed network simulation and network virtualization (NFV). Mahendra Bhatu Gawali et al. [2] proposed a heuristic approach combining the modified analytical hierarchy process (MAHP), bandwidth aware divisible scheduling (BATS) +BAR optimization, longest expected processing time preemption (LEPT) and dividing-and-conquering methods for scheduling tasks and allocating resources. Haitham Salman Chyad et al. [3] addressed utilization of soft computing with better efficiency on cloud to automate and plan the tools. Rajanikanth Aluvalu et al. [4] recommended productive allocation of virtual machines for successful use and increase in resource utilization and productive virtual machine implementation in cloud resources. Abhirup Khanna et al. [5] presented a novel resource allocation system which works on the dynamic resource allocation principles. B. Adrian et al. [6] proposed K-means clustering algorithm for virtual machine allocation process in place of cloudSim FIFO algorithm. Bhavan Bidarkar et al. [7] addressed optimal algorithms for load balancing. Sandeep Kapur et al. [8] presented a unique way of choosing encryption algorithms to prevent misuse. Mahesh et al. [9] suggested the method of decentralized distribution of services delegated to cloud consumers. The calculation of unequal usage of different VM services and the skew interest load balancing between VMs can be used.

Tinghuai Ma et al. [10] discussed five main cloud computing topics: locality-aware job scheduling; reliability-aware scheduling; RAS energy-aware; RAS layer of SaaS software; and workflow scheduling. Mayanka Katyal et al. [11] provided a broad variety of load balancing solutions in different cloud settings focused on Service Level Agreement (SLA) specifications. Lu Huang et al. [12] is focused on the actual condition in the cloud with the algorithms of resource management and scheduling. V Vinothina et al. [13] discussed in detail various resource allocation strategies and their challenges.

HAProxy load balancer has very high load bearing capacity when implemented with Round Robin algorithm which uses basic data structures to perform resource allocation. The algorithm implemented in this work does not store the states of the previous requests of the prior states, instead it performs hash mapping of the resources allocated to a particular virtual machine. It also maintains the state list which shows the availability of virtual machine for performing resource allocation, based on which the HAProxy can allocate resources to the available virtual machines exclusively, thus maintaining data integrity. Load balancers like application load balancer redirects the incoming requests based on the IP address of the virtual machines whereas, the HAProxy load balancer is configured for the user to access the webpage through public DNS of the load balancer. The load balancer is responsible for allocating resources cyclically using round robin algorithm.

2.0 System Development

The system development starts by creating a Relational Database System (RDS). The RDS is linked to the two EC2 instances (VM1 and VM2), each one acting as a separate virtual server. HAProxy is set up as the load balancer as it is efficient with quick response time and it uses the RRA to assign resources to the VMs. Some more significant aspects of the virtual network include security groups which is created for each entity, and a VPC which is created for the whole network.

2.1 Methodology

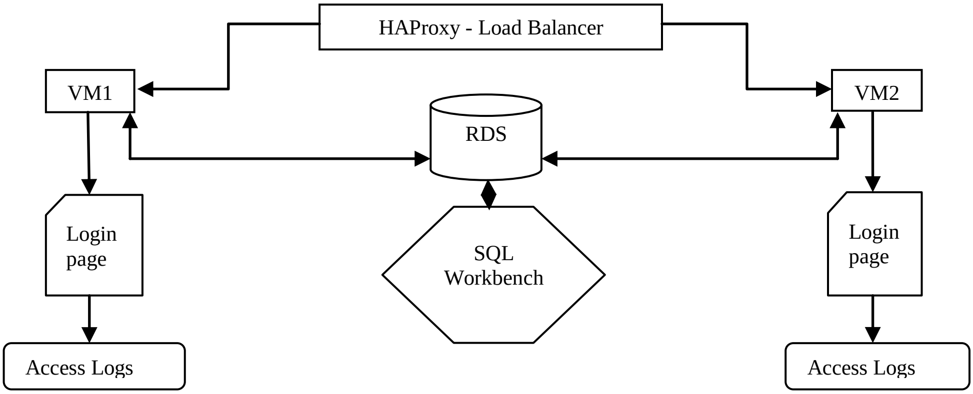

Fig. 1. Process of optimal load balancing using HAProxy

Process of optimal load balancing using HAProxy is shown in Fig. 1. Two Amazon Elastic Cloud Compute instances (VM1 and VM2) were created to act as virtual servers. Amazon RDS is used to create the database accessed by the EC2 instances. The contents of the RDS instance can be known by checking the SQL workbench. The VM1 and VM2 instances are connected to apache web servers which host login pages that act as a user interface. A third instance EC2 instance is created to act as the HAProxy, which performs as a load balancer by distributing the load amongst the servers. The HAProxy instance is configured to balance the load by specifying the Public DNS of the virtual servers in its configuration file. Accessing the Public DNS of the HAProxy instance will redirect the user to either of the virtual servers. An entry is made into the access logs of each of the virtual servers whenever the HAProxy instance's Public DNS is visited. It is observed that even when one of the two virtual servers is turned off, the HAProxy redirects the user to the working server. The same will be reflected in the servers' access logs.

2.2 Creating Database Instance

Using the Amazon RDS on AWS, MySQL database is created. There is a header called Databases in AWS under which RDS is found. In order to set up MySQL database, certain specifications must be made while creating an instance of MySQL database. The class of instance used is t2.micro that has a storage capacity of 20 GB with one day of automated backup. The database is created by choosing Create database option. Various database engines are available on AWS including Oracle, Amazon Aurora, MySQL, etc. MySQL is used as the engine in this work for the database after configuration.

2.3 Creating EC2 Instances

Once the database is created using RDS instance, EC2 instances must be created to serve the purpose of web servers (VM) and load balancer. Two of the instances created host login pages via apache web server. Each instance created is linked to a previously created VPC and security group, having public and private subnets in at least two availability zones.

2.4 Installing Apache Web Server

After creating the EC2 instances they are connected to apache web servers that host login pages created as a PHP file. The option to fix all the previous bugs and to update security of the EC2 instance must be chosen to update the command prompt interface with a predefined command. In order to create the login page, it is necessary to install the software package of PHP using a command on Linux *sudo yum install.* Using this software package the Apache web server will be installed. If the apache web server page is displayed when the DNS of an instance is accessed, it can be confirmed that the instance is connected to the apache server. Permissions are given to the web server and www group is added to the ec2-user group. Other general commands for refreshing, logout, changing directory, etc. are specified.

2.5 Connecting Web Server and Database

Once the apache web server is installed it should be connected to the database created on AWS, i.e. the RDS instance. This connection is done by specifying parameters such as 'DB_SERVER' (the end point of the database), 'DB_USERNAME" (user dependent), 'DB_PASSWORD' (user dependent) and ‘DB_DATABASE’ (default is sample) in the PHP file, which contains the code for the login page.

Connection with the created EC2 instance is kept as it is and a new subdirectory is created. The directory is changed to *www/html* and a fresh file is created in html format to code the login page in PHP. This file is edited in Sublime Text editor. The code ensures that a connection is established between the RDS instance and the Apache Web Server.

2.6 Round Robin Algorithm

RRA distributes workload on the basis on the round robin principle. The workload is distributed to the servers equally in a periodic manner. The assignment of the load is done in circular fashion without considering any priority and after reaching the last VM, it allocates the requests back to the first VM. The cycle repeats as long as the requests are being sent. This method of static allocation is easy to use and implement. The execution time for this model is less as there is no inter-process communication.

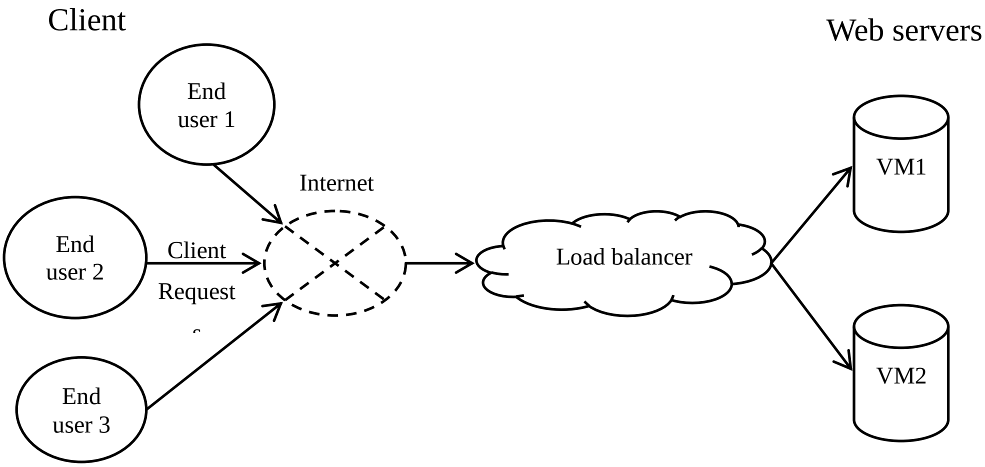

Fig. 3. Representation of interface from client to server in cloud environment

The RRA implemented in this work has a very high load bearing capacity. This algorithm need not save the prior states of the previous requests and is developed using concepts of basic data structures. One of the most important data structures maintained is the state list of each web servers (VM) which stores the allocation status of each VM, i.e., if it is busy or available for resource allocation. One of the other important data structures used is hash mapping, which stores the entry details of the request of a client and the VM allocated for the same [7]. If one of the VMs go down, the load balancer identifies it and the request is allocated to the VMs that are active and free to perform their duties. The first step of the algorithm is to consider all the VMs available in the list and set their allocation status to available or not available. At first there will be no entries and therefore the hash mapping will be set to no entries. If there are new requests received by the load balancer then the load balancer must queue these requests first for allocation in RRA, and it removes requests one at a time from top of the queue of requests. If the VM satisfies the conditions of the request sent, and the hash map contains the data necessary, the VM is assigned for the mentioned process. If these conditions are not satisfied, the request is allocated to the following VM using the RRA. Once the allocation is done, an entry is made in the hash mapping data structure and also into the VM list. The process is shown in Fig. 3.

3.0 Results and Discussion

Public key is used to log into AWS via terminal, and the EC2 instance's Public DNS is used to access the login pages. Three EC2 instances were generated on AWS. Two instances (instance 1 and instance 2) act as virtual servers. The third instance is the HAProxy load balancer. To activate the HAProxy, it must be accessed using the security pem file, similar to that of the other two instances.

HAProxy is configured in the config file to balance the incoming load amongst the VMs. The Public DNS IDs of the two VMs (instance 1 and instance 2) are assigned as active servers to the HAProxy, and the RRA is specified. The login page is hosted by apache web server. All the login details are stored in the RDS instance created. The initial access log file is created as soon as the server is created, and it is located in the var/log/httpd folder.

Every time a user accesses the login pages, through the HAProxy, an entry is created in the access log file of that instance. Access log files are created on a daily basis, from which information on server load can be obtained. Simulation results are presented in Table 1.

Table 1. Simulation results based on the number of users

No of Users	Execution time, ms	Load average	Idle state	UNIX Ports	Internet connection state	Memory status
1-5	0.690	0.0~0.1	Almost 100	No duplicates	Established	Good
5-10	0.726	0.2	99			
10-15	0.747	0.7	92			
15-20	0.786	0.9	87			
20-25	0.801	1.2	81			

As the number of users increased, the average load on the load balancer, execution time and CPU usage increased. As the number of clients increased the run-time changed nominally, showing that the proposed model is responsive.

4.0 Conclusion

Resource allocation in a virtual environment was implemented using HAProxy as load balancer. Amazon RDS provides database storage of 20 GB which can be expanded to 1TB based on the requirements. The Round Robin algorithm used in this work is more efficient as the EC2 instances used as the web servers have same specifications of capacity and response time. HAProxy has high load bearing capacity with a low response time, ensuring faster resource allocation. The combination of HAProxy, EC2 instances and the Amazon RDS database makes the resource allocation mechanism efficient and reliable.

In case of web servers with different load bearing capacities, the round robin algorithm can be modified. Implementation of HAProxy as load balancer increases the flexibility and makes optimal usage of the VMs when compared with application load balancer.

References

1. L Cao, S Fahmy, P Sharma, Data-driven Resource Allocation in Virtualized Environments, *2019 IFIP/IEEE Symposium on Integrated Network and Service Management (IM), Arlington, VA, USA*, 20(6), 659-664, 2019
2. Mahendra Bhatu Gawali, Subhash K Shinde, Task scheduling and resource allocation in cloud computing using a heuristic approach, *Journal of Cloud Computing: Advances, Systems and Applications,* 7(4), 1-16, 2018
3. Haitham Salman Chyad, Raniah Ali Mustafa, Kawther Thabt Saleh, Study and Implementation of Resource Allocation Algorithms in Cloud Computing, *International Journal of Engineering & Technology*, 7 (4.28), 591 -594, 2018
4. Rajanikanth Aluvalu, M A Jabbar Vardhaman, Jalpa Kantaria, Performance evaluation of clustering algorithms for dynamic VM allocation in cloud computing, *2017 International Conference On Smart Technologies For Smart Nation (SmartTechCon), Bangalore, 1560-1563,* 2017
5. A Khanna, Sarishma, RAS: A novel approach for dynamic resource allocation, *1st International Conference on Next Generation Computing Technologies (NGCT), Dehradun*, 25-29, 2015
6. B Adrian, L Heryawan, Analysis of K-means algorithm for VM allocation in cloud computing, *International Conference on Data and Software Engineering (ICoDSE),* Yogyakarta, 48-53, 2015
7. Bhavana Bidarkar, Shakheela Attikeri, Ramya S Pure, Round Robin Approach for Better VM Load Balancing in Cloud computing, *International Journal of Engineering Innovation & Research, 3 (*4), 499-502, 2014

8. Sandeep Kapur, Kumar Dinesh, Resource Utilization in Cloud Computing using Hybrid Algorithm, *Indian Journal of Science and Technology*, 9 (43), 1-10, 2016

9. Mahesh, Prashant, Poonam, An Efficient Dynamic Resource Allocation Strategy for VM Environment in Cloud, *International Conference on Pervasive Computing*, 4(2), 1-5, 2015

10. Tinghuai Ma, Ya Chu, Licheng Zhao, Otgonbayar Ankhbaya, Resource Allocation and Scheduling in Cloud Computing: Policy and Algorithm, *IETE Technical Review*, 31 (1), 4-16, 2014

11. Mayanka Katyal, Atul Mishra, A Comparative Study of Load Balancing Algorithms in Cloud Computing Environment, *International Journal of Distributed and Cloud Computing*, 1 (2), 5-14, 2013

12. Lu Huang, Hai-shan Chen, Ting-ting Hu, Survey on Resource Allocation Policy and Job Scheduling Algorithms of Cloud Computing, *Journal of Software,* 8 (2), 480-486, 2013

13. V Vinothina, R Sridaran, Padmavathi Ganapathi, A Survey on Resource Allocation Strategies in Cloud Computing, *International Journal of Advanced Computer Science and Applications*, 3 (6), 97-104, 2012

Synthesis, Experimental and Theoretical Study of Imine based Conjugated Polymer for Humidity Sensing Applications

Vishnumurthy K A[1*], Girish K H [2], Pallavi S G[1]

[1]*Department of Chemistry, RV College of Engineering®, Bengaluru*

[2]*Department of Mechanical Engineering, RV College of Engineering®, Bengaluru*

Abstract

A donor-acceptor conjugated polymer was synthesized by poly-condensation reaction of dialdehyde and aromatic diaime. The characterization of polymer was done by UV-Vis, FT-IR, ^{1}H NMR spectroscopic techniques. The obtained polymer was found to be partially soluble inorganic solvents such as chlorobenzene, DMF. The polymer was found to be responsive to humidity, which varied its electrical properties on exposure to humidity, arising due to protonation of imide nitrogen in polymer backbone. Further, Theoretical studies using density functional theory (DFT) were performed on the polymer to optimize the geometry, verify the proposed experimental sensing mechanism and also to understand its photophysical properties. The theoretical results showed good agreement with the experimental values. Humidity sensing properties like response-recovery and the reproducibility of the polymer were also studied. The research findings showed that the new polymer is promising material in moisture sensing application.

Keywords: *DFT method, Imine linkage, Donor acceptor, moisture sensor*

1.0 Introduction

The ability of conjugated polymers (CP) to interact with various analytes resulting in changes in their photo physical properties have been explored by the scientific community extensively for sensing various toxic gases such as NH_3, NO_2, CO_2, CO, HCl and volatile gases like alcohol and in humidity sensing applications [1-4]. These conjugated polymer-based sensors are more imperative as compared to metal oxide-based sensors due to their faster response and recovery, ease of fabrication and ability to operate at room temperature. Recently, humidity sensors have gained increasing applications in both industries, in environmental control as well as in house-hold equipment's like microwave ovens, washing machines etc. Based on the measurement units, there are two types for humidity sensors Relative Humidity (RH) sensors and Absolute humidity (moisture) sensors. Most humidity sensors are relative humidity sensors and can be further classified based on the materials used for the development of sensors into ceramic sensing materials, semi-conducting

---

**Mail address: Vishnumurthy K A, Assistant Professor, Department of Chemistry,*
RV College of Engineering®, Bengaluru-560 059
Email: vishnumurthyka@rvce.edu.in Ph.: +91 9741211557

materials and polymer-based humidity sensors [5]. Most of the commercial humidity sensors available in the market are resistive based humidity sensors [6]. The material used for sensing may be ceramic, polymers or electrolytes. They display change in the conductivity due to adsorption of water vapor [7]. Conjugated polymers emerge as promising materials for humidity sensors. They have presence of unsaturation or double bonds and offer flexibility in controlling their band gap by substituting various donor (D) acceptor (A) moieties which dictates the electrical and optical properties of the polymer. Water can easily protonate these double bonds and shows changes in the conductivity. Conjugated polymers like polyaniline have been previously reported to be used as humidity sensors. Polyaniline and its composites with zinc oxide, magnesium chromate[8], doped with acids [9], PANI-chitin blend[10] have also been reported as humidity sensors. Additionally, Poly pyrrole and its composites have also been studied in humidity sensors[11 - 12].

Considering the above, we report the synthesis of polymer P, bearing a surplus of phenylene group. The polymer P proved to be a potential candidate for humidity sensing with high response for which the sensing mechanism was studied. Optical and electrical properties of polymer P was experimentally studied using UV, FT-IR and NMR techniques. Additionally, theoretical calculations were performed using density functional theory (DFT) and time dependent DFT (TDDFT) to characterize the photophysical properties such as HOMO-LUMO, band gap and UV-vis spectra of polymer P and to elucidate the response mechanism of the polymer towards humidity sensing.

2.0 Experimental Work

2.1 Synthesis of polymer P

The Octyl diphenylamine dialdehyde (ODPADA) monomer was synthesized according to reported literature [13]. Polymerization of N-Octyl diphenylamine dialdehyde (ODPADA) with p-diamino diphenyl (Polymer P) Condensation polymerization of Octyl diphenylamine dialdehyde (ODPADA) with 1,4 diphenylene diamine was carried out using anhydrous methanol as the solvent. For this, both the monomers, dialdehyde (0.00297 mole) and 1,4 diphenylene diamine (0.00297 mole) each one equivalent were mixed with each other in 25 ml of methanol in a round bottom flask. On formation of homogeneous solution, 2 drops of concentrated sulfuric acid were added which immediately resulted in formation of a dark red colored precipitate. The polymerization reaction was carried for 4 hours at room temperature. After 4 hours, polymerization was terminated by pouring in ice cold water and then filtering the product through Buchner funnel. The impurities present in the polymer i.e. polar and non-polar were removed by stirring the polymer in hexane and ethyl acetate solvents followed by decantation. Thus, the obtained precipitate was dried under ambient conditions and is as shown in Scheme 1.

Polymer P was partially soluble in the organic solvents like chlorobenzene, DMF, DMSO etc. The partial solubility may be due to the increased molecular weight of the polymer. The polymer showed high thermal stability may be attributed to the presence of aromatic phenyl rings. Due to partial solubility of the polymer, thin films on the glass plate were prepared by solid state method. For this, solid polymer powder was ground with few drops of DMF in a mortar and pestle and then cast on the glass plate.

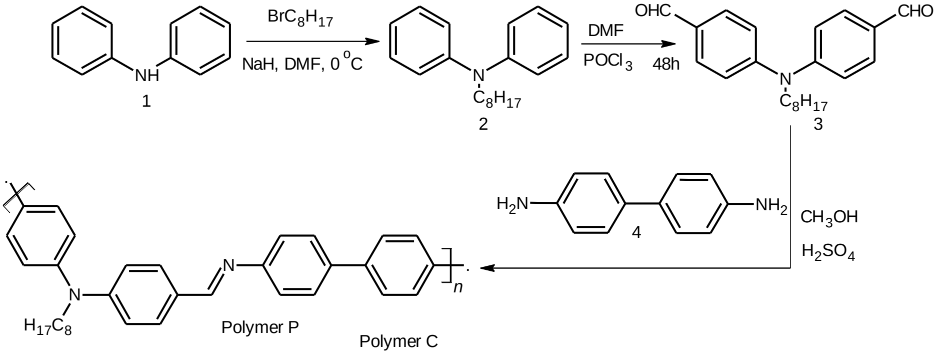

Scheme 1: Synthesis of Polymer P

3.0 Material Characterization

3.1 Materials

Dialdehyde monomer was synthesized according to the reported procedure[13]. All the chemicals used in present work were procured from Sigma Aldrich and Lanchaster (UK). All the solvents purchased were of analytical grade and was used as such without any further purification.

3.2 Instrumentation

Infrared spectra of all compounds and polymer were recorded using Nicolet Avatar 5700 FTIR (Thermo Electron Corporation). The UV-visible spectrum was recorded in Perkin Elmer LS55. ^{1}H NMR spectra were obtained with Brukere 400 MHz FT-NMR spectrometer using TMS/solvent signal as internal reference.

3.3 Characterization

FTIR spectroscopic study of the polymer showed strong bands at 2927(Aromatic C-H stretch), 2848, 2600(Broad C-N stretch), 1575(C=C stretch), 1497, 1353(=C-N stretch), 1136(-C-N stretch), 1029, 801. Disappearance of carbonyl stretching frequency from 1685 cm^{-1} from the dialdehyde monomer indicates that the formyl group involved in polymerization reaction. Also formation of peak at 1353 cm^{-1}represents the formation of imine linkages in the polymer backbone as represented in Fig. 1.

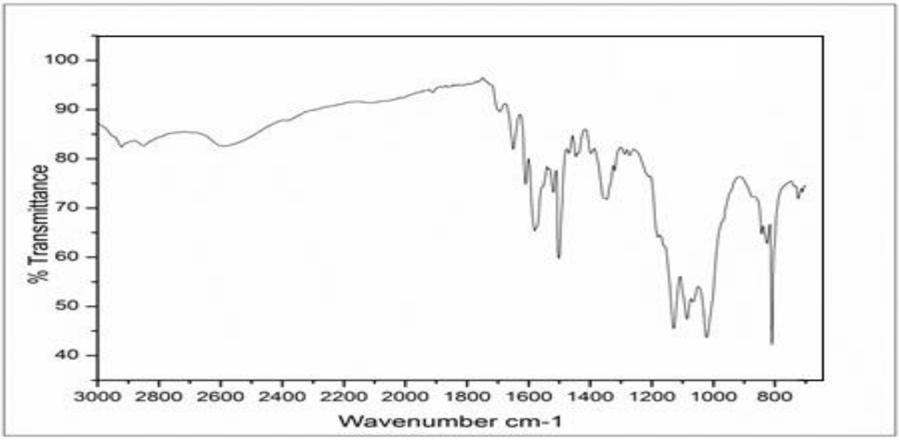

Fig.1. FT-IR spectrum of Polymer P

The NMR spectral study of the polymer showed chemical shifts at 7.89-7.3δ (m)(Benzyl H), 7.27-7.1 δ (m)(Benzyl H), 6.65, 6.62 δ (s) (-N=CH), 3.82 δ (t)(N-$CH_{2)}$,1.62 δ (m)(- CH_2-) , 1.18 δ (m)(- CH_2-)0.79δ (t)(-CH_3). Disappearance of aldehydic proton from the monomer clearly indicates that the polymerisation reaction is happened with the monomer. Also appearance of new –N=CH- chemical shift at 3.82δ indicates the formation of imine functionality in the polymer bbackbone and it is represented in Fig. 2.

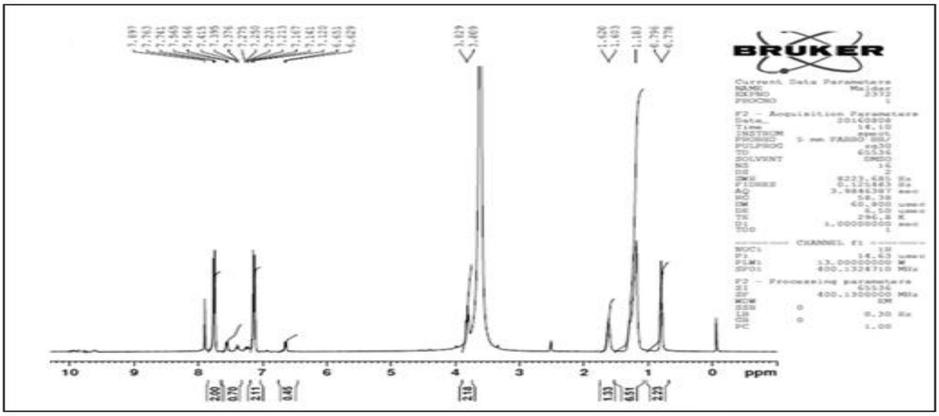

Fig. 2. NMR spectrum of Polymer P

3.4 Optical study of the polymer

UV-Visible spectral study of the polymer was done in thin films. Thin films are casted on glass surface and taken for study. The absorption maximum of polymer was found to be 350 nm in film state **Fig. 3**. The optical band gap was calculated by using optical edge and was found to be 3.04 eV. The broad absorption of the polymer may be attributed to its donor acceptor nature and conjugation due to imine linkage.

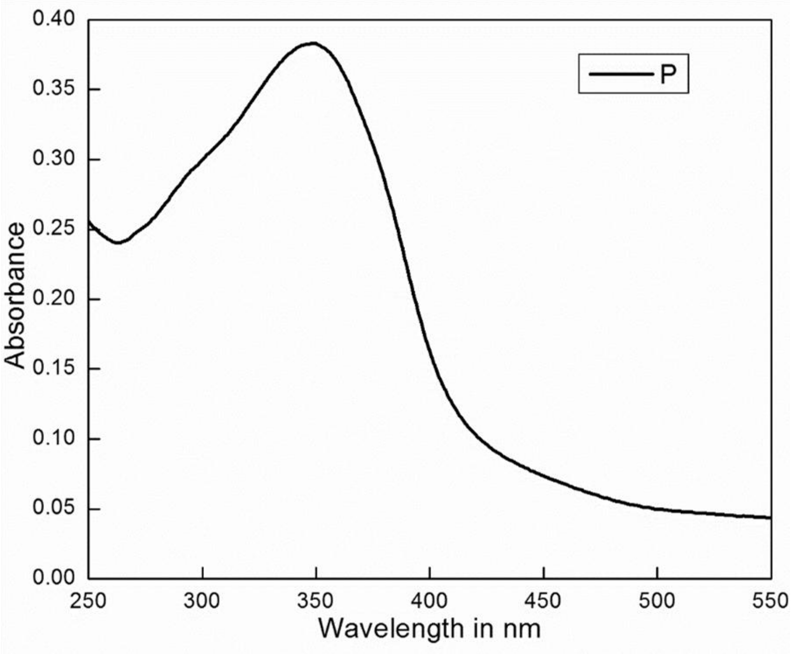

Fig. 3. UV-Visible spectrum of Polymer P in film

4.0 Computational Details

The theoretical computational studies on Polymer P were performed using density functional theory (DFT) to optimize the geometry and to understand the humidity sensing mechanism by the polymer. To reduce the computational cost, a single repeating unit of the polymer is considered for computations and the alkyl side chains were replaced by propyl chains. The geometries of polymer P and polymer P-H_2O complex were optimized using Becke's three parameter hybrid functional [14] with the Lee, Yang, and Parr correlation functional (B3LYP) using the Pople basis set, 6-31G(d) [15], in THF solvent. The dispersion interactions effects were also included using Grimme's DFT-D3(BJ) method. Further, the photophysical properties of polymer were calculated utilizing time dependent DFT (TDDFT) at B3LYP/cc-pVTZ level of theory in THF solvent incorporating CPCM solvent model. The humidity sensing mechanism of polymer was theoretically elucidated by interpreting the intermolecular bond lengths between host and guest molecule and variation in photophysical properties of polymer P and its complex. All the theoretical calculations were performed using ORCA 4.0.1 platform [16].

5.0 Results and Discussion

5.1 Humidity sensing of polymer P.

It has been well reported that saturated salt solutions, at a given temperature, in an enclosed environment generate an environment of particular relative humidity. The generated relative humidity depends upon the particular salt used[17], [18] . Relative humidity (RH) is defined as the amount of moisture content of air to the amount of the saturated moisture content of air at the same temperature and pressure[5], [7]. The RH%= Pv/Ps where Pv= Actual partial pressure of moisture content And Ps= Saturated pressure of moist air.

Thus, different saturated salt solutions (solid salt present) were prepared from chemically pure salt and distilled water in a sealed glass chamber and allowed to stabilize for 24 hours at room temperature. The solutions are as shown in the Fig. 4. At a specific temperature, different relative humidity in an enclosed space for a given salt solutions is known. Using the same, we have generated different relative humidity in the closed chamber for a specific salt solution and sensor measurements of the polymer P in this environment was successfully initiated. We have measured the response of polymer P at different relative humidity values and they are as reported in Table 1 and the graph of % response vs % relative humidity is as depicted in Fig. 5. Polymer P shows very good response (58%) even towards low relative humidity of 8.3%. The response increases drastically from 58% to 91.1% by increasing the relative humidity from 8.3% to 22.5%.

Fig. 4. Saturated salt solutions corresponding to different relative humidity

Table 1. Response of Polymer P on exposing to different relative humidity

Sl. No.	Chemical	Relative Humidity	Initial resistance (G Ohm)	Final resistance (G Ohm)	Response Time (sec)	Recovery Time (sec)	Diff resistance (G Ohm)	% Response
1	KOH	8.3	34	14	50	59	20	58.8
2	CH_3COONa	22.5	30	2.66	61	105	27.34	91.1
3	$CaCl_2$	32	22	1.95	68	110	20.05	91.1
4	K_2CO_3	43.2	32	2.3	94	123	29.7	92.8
5	$Mg(NO_3)_2$	57.6	24	2.4	77	112	21.6	90.0

6	NH_4NO_3	64	28	2.6	73	102	25.4	90.7
7	KI	68.8	35	3.2	61	83	31.8	90.9
8	NaCl	75.3	30	2	67	92	28	93.3
9	KCl	84.3	33	2.2	57	48	30.8	93.3
10	KNO_3	94	32	0.74	122	121	31.26	97.7
11	K_2CrO_4	97.88	32	1.01	60	84	30.99	96.8
12	K_2SO_4	97.3	32	0.55	83	111	31.45	98.3

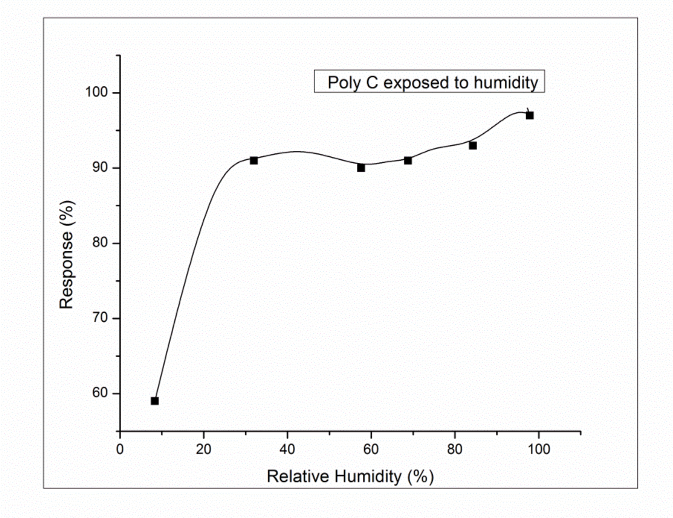

Fig. 5. Response of Polymer P at different relative humidity

5.1.1 Proposed mechanism for humidity sensing

Polyaniline shows non-redox doping by protonation. Water is also able to protonate PANI and its mechanism is well established. Imine nitrogen in PANI undergoes protonation due to which the resistance of polyaniline decreases[17]. On exposing polymer P to different relative humidity's, it has been observed that its film resistance decreases. This decrease in the resistance can be attributed to the protonation of H in to the polymer matrix. This protonation of imine nitrogen is very much similar to protonation which takes place in polyaniline. The decrease in resistance of polymer film is as shown in Fig. 6 and the probable mechanism displayed in Fig. 7.

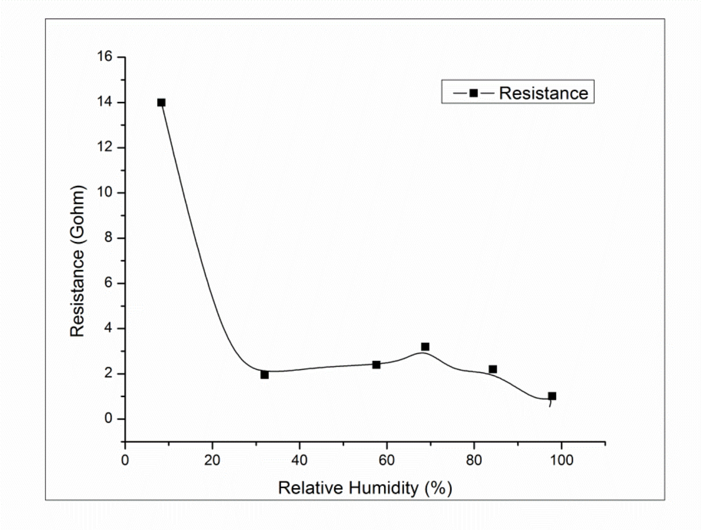

Fig. 6. Decrease in resistance of Polymer P at different relative humidity values

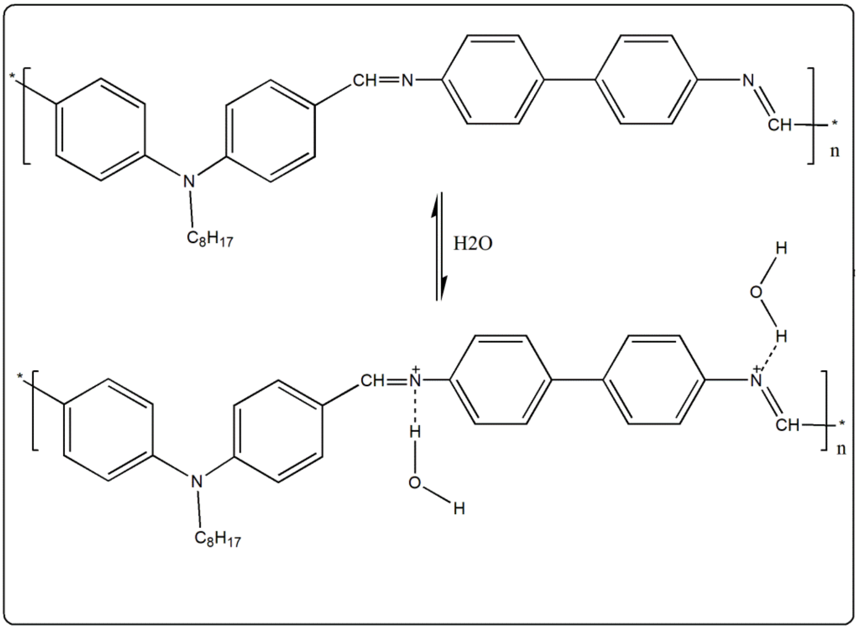

Fig. 7. Mechanism of protonation for Polymer P

The response and recovery time for the polymer film was also studied. The graph is as shown in Fig. 8. Both response and recovery time initially increased and then decreased. These observations happened rapidly between 1-2 min.

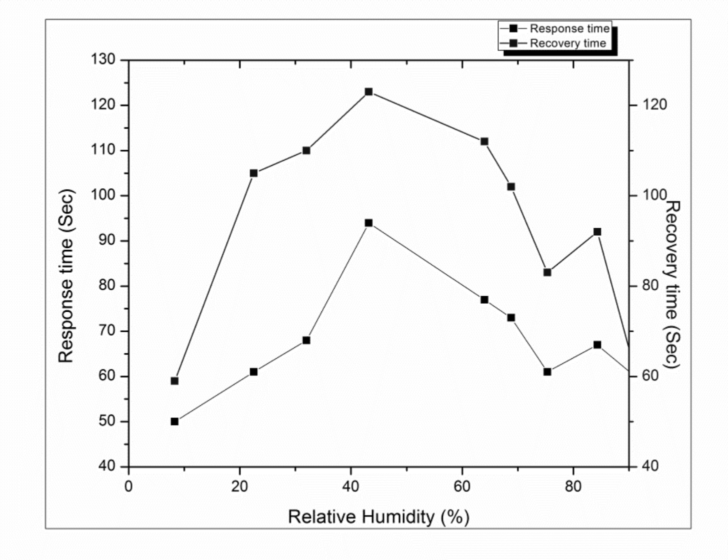

Fig. 8. Response- recovery studies of Polymer P at different relative humidity

5.2 Quantum chemical calculations

The geometry optimization of polymer P and its complex with water molecules was performed using DFT at B3LYP/6-31G(d) level of theory in THF solvent. The respective optimized structures are depicted in Fig. 9-10. The protonation sites on polymer backbone due to its interaction with water molecules were considered as suggested by experimental mechanism for the optimization of its complex state geometry. From Fig. 10 it can be noted that in the presence water molecules, the polymer forms hydrogen bond with the nitrogen atoms with bond lengths of 0.977Å and 1.221Å. These interaction bond lengths are comparable to the covalent bond length of N-H in the system, thus confirming the protonation of polyaniline.

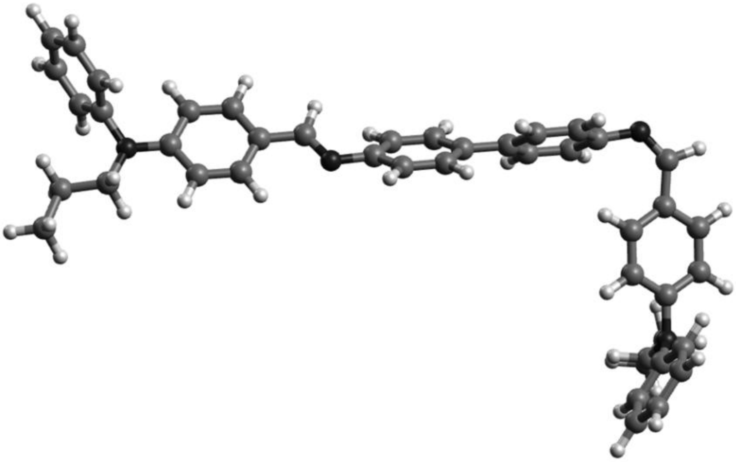

Fig. 9. Optimized geometry of polymer P at B3LYP/6-31G(d) in THF solvent

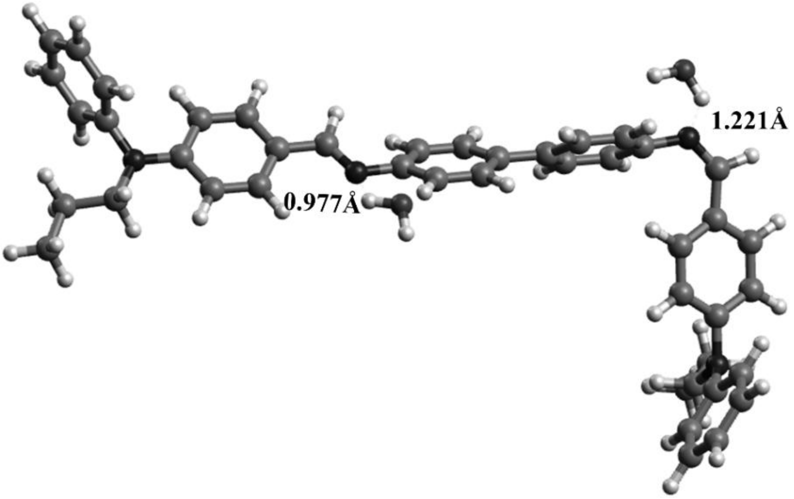

Fig. 10. Optimized geometry of polymer P + water complex at B3LYP/6-31G(d) in THF solvent

The Mulliken charges of polymer P were calculated at the same level of theory which is depicted in Fig. 11. From the bar graph it can be noted that the nitrogen atoms in the ground state geometry showed higher negative charge values indicating that these are the potential sites for protonation, and all the hydrogen atoms showed almost equal positive charge values.

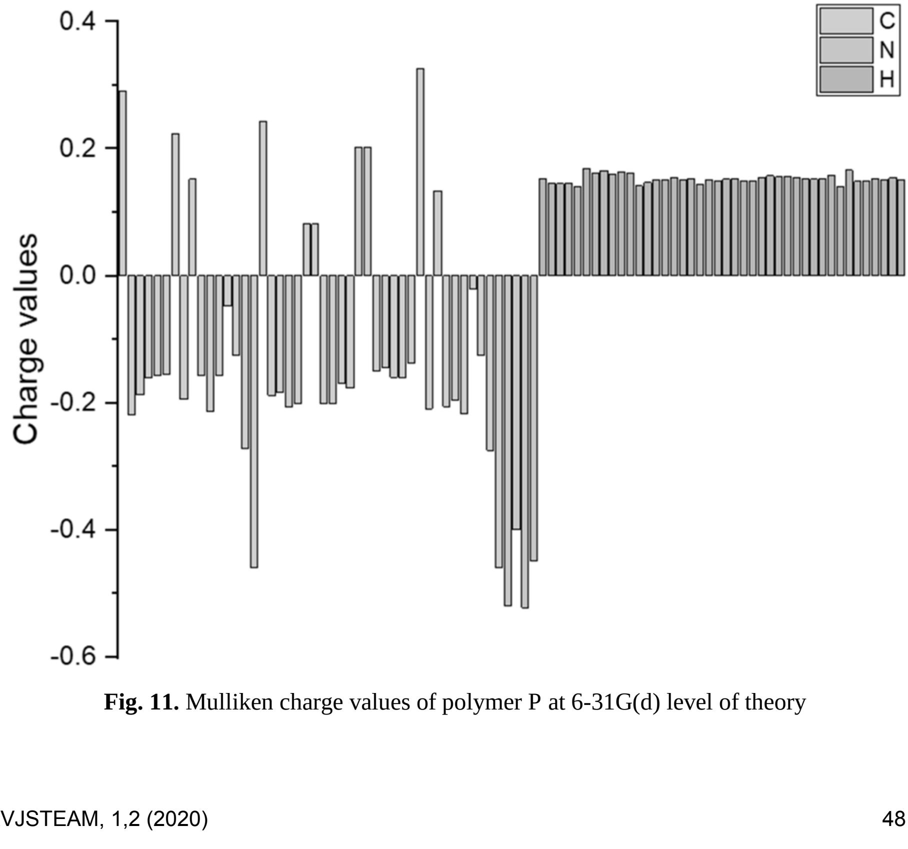

Fig. 11. Mulliken charge values of polymer P at 6-31G(d) level of theory

The frontier molecular orbital density plots of polymer P is visualized in Fig. 12. From the theoretical calculations the HOMO and LUMO values were found to be -5.269 eV and -1.795 eV respectively having a theoretical HOMO-LUMO energy gap of 3.47eV which is in good agreement with the experimental value (3.04 eV). From Fig. 12 it can be noted that HOMO orbital density is distributed over the entire monomer unit and LUMO orbital density localized over diphenylene ring, dictating the effective charge transfer across D-A system.

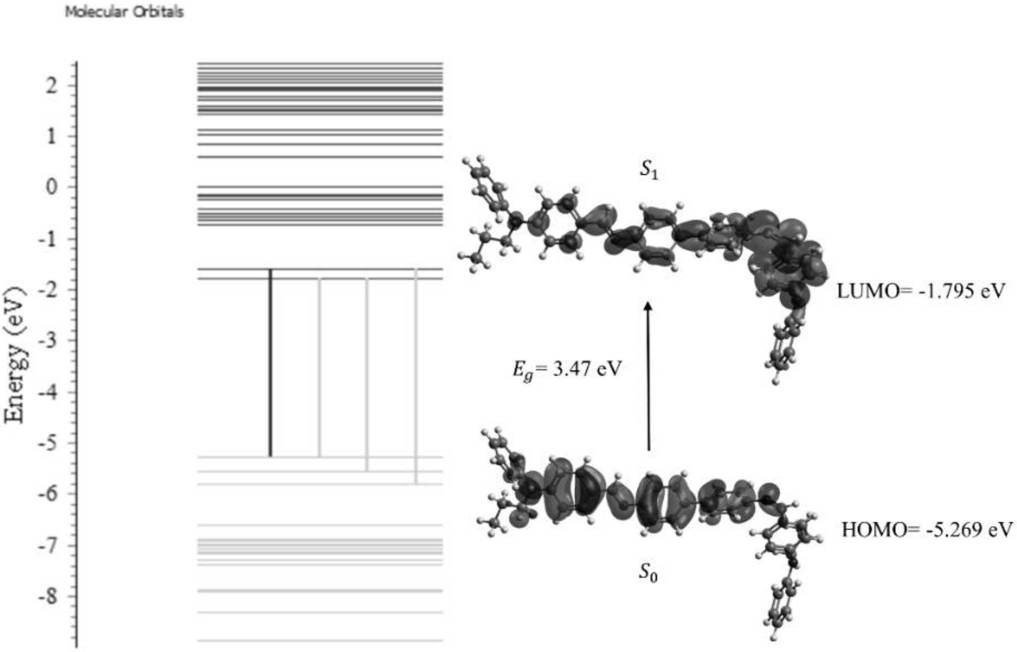

Fig. 12. HOMO-LUMO energy of polymer P in THF solvent (isovalue=0.02)

Table 2. Photophysical properties of Polymer P.

Major transitions*	**Energy (cm^{-1})**	**Osc. Strength (*f*)**	**λ_{max} (nm) theoretical**	**λ_{abs} (nm) experimental**
H→L+1 (78%)	26656.5	1.3762	375.14	350
H-1→L (77%)	21953.6	0.1332	455.50	-
H→L (75%)	21811.7	0.4295	458.47	-

**H denotes HOMO and L denotes LUMO*

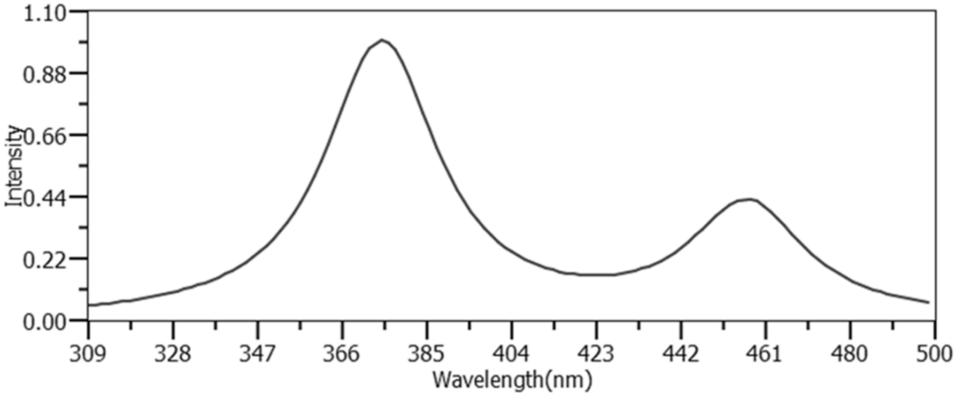

Fig. 13. Theoretical UV-vis spectra of polymer P

The theoretical optical and electronic properties of polymer P was studied employing time-dependent density functional theory (TDDFT) at B3LYP/cc-pVTZ level of theory in THF solvent system incorporating CPCM model. The above optimized geometry was used for TDDFT calculation. The major orbital transitions, oscillator strengths and absorption wavelengths are summarized in Table 2. The polymer P showed an absorption peak at 375.14 nm (Fig. 13) contributed by transition of HOMO→LUMO+1 (78%) having an oscillator strength of 1.3762. The theoretical calculations showed good agreement with the experimental values hence the polymer may be a potential candidate for humidity sensing.

6.0 Conclusion

A new donor acceptor conjugated polymer containing iminebridge was successfully designed and synthesized via poly condensation reaction. The structure of monomer and polymer were characterized by various spectroscopic techniques. The newly synthesized polymer showed absorption maximum at 350 nm with the optical band gap of 3.04 eV. The polymer films were casted on glass plate and used for sensor studies. Polymer showed very good response (58%) even with very low relative humidity of 8.3%. The response of polymer films increased drastically from 58% to 91.1% by increasing the relative humidity from 8.3% to 22.5%. The sensor response mechanism of polymer towards moisture may be due to the hydrogen bonding interaction. Further theoretical DFT studies of the polymer were in good agreement with the experiment results. Optimized geometry of polymer P + water complex showed clear evidence for bonding interaction between from theoretical study. The Sensing studies were showed enhanced response and recovery time. This may be attributed to the porous nature of the polymer which slows down the adsorption and desorption process on the surface of the sensor.

References

1. H Bai, G Shi, Gas Sensors Based on Conducting Polymers, *Sensors (Basel)*, 7(3), 267–307, Mar. 2007
2. N Mergu, H Kim, J Ryu, Y A Son, A simple and fast responsive colorimetric moisture sensor based on symmetrical conjugated polymer, *Sensors and Actuators B: Chemical*, 311, 127906, May 2020, doi: 10.1016/j.snb.2020.127906.
3. J C Bittencourt, B H de S Gois, V J R de Oliveira, D L da S Agostini, C de A Olivati, Gas sensor for ammonia detection based on poly(vinyl alcohol) and polyaniline electrospun, *Journal of Applied Polymer Science*, 136 (13), 47288, 2019
4. M O Ansari, S A Ansari, M H Cho, S P Ansari, M S Abdel-wahab, A Alshahrie, Conducting Polymer Nanocomposites as Gas Sensors, *Functional Polymers*, M. A. Jafar Mazumder, H. Sheardown, and A. Al-Ahmed, Eds. Cham: Springer International Publishing, 2018, 1–30
5. H Farahani, R Wagiran, M N Hamidon, Humidity Sensors Principle, Mechanism, and Fabrication Technologies: A Comprehensive Review, *Sensors*, 14 (5), 7881–7939, May 2014
6. S A Kolpakov, N T Gordon, C Mou, K Zhou, Toward a New Generation of Photonic Humidity Sensors, *Sensors*, 14 (3), 3986–4013, Mar. 2014
7. C Y Lee, G B Lee, Humidity Sensors: A Review, Jan. 2005. https://www.ingentaconnect.com/content/asp/senlet/2005/00000003/f0040001/art00001;jsessionid=htp5e7h1nvji.x-ic-live-01 (accessed Apr. 03, 2020).
8. T Machappa, M V N A Prasad, Humidity sensing behaviour of polyaniline/magnesium chromate (MgCrO4) composite, *Bull Mater Sci*, 35 (1), 75–81, Feb. 2012
9. S Jain, S Chakane, A B Samui, V N Krishnamurthy, S V Bhoraskar, Humidity sensing with weak acid-doped polyaniline and its composites, *Sensors and Actuators B: Chemical*, 96 (1), 124–129, Nov. 2003
10. A T Ramaprasad, V Rao, Chitin–polyaniline blend as humidity sensor, *Sensors and Actuators B: Chemical*, 148 (1), pp. 117–125, Jun. 2010
11. P G Su, Y P Chang, Low-humidity sensor based on a quartz-crystal microbalance coated with polypyrrole/Ag/TiO2 nanoparticles composite thin films, *Sensors and Actuators B: Chemical*, 129 (2), 915–920, Feb. 2008
12. M Z Yang, C L Dai, D H Lu, Polypyrrole Porous Micro Humidity Sensor Integrated with a Ring Oscillator Circuit on Chip, *Sensors*, 10 (11), 10095–10104, Nov. 2010

13. K A Vishnumurthy, M S Sunitha, R Philip, A. V. Adhikari, New diphenylamine-based donor–acceptor-type conjugated polymers as potential photonic materials, *Reactive and Functional Polymers*, 71 (12), 1119–1128, Dec. 2011

14. A D Becke, Density- functional thermochemistry. III. The role of exact exchange, *The Journal of Chemical Physics*, 98 (7), 5648–5652, Apr. 1993

15. W J Hehre, R Ditchfield, J A Pople, Self—Consistent Molecular Orbital Methods. XII. Further Extensions of Gaussian—Type Basis Sets for Use in Molecular Orbital Studies of Organic Molecules, *The Journal of Chemical Physics*, 56 (5), 2257–2261, Mar. 1972

16. F Neese, The ORCA program system, *WIREs Comput Mol Sci*, 2 (1), 73–78, Jan. 2012

17. A Carotenuto, M Dell Isola, An experimental verification of saturated salt solution-based humidity fixed points, *Int J Thermophys*, 17 (6), 1423–1439, Nov. 1996

18. L Greenspan, Humidity Fixed Points of Binary Saturated Aqueous Solutions, *Journal of Research of the National Bureau of Standards Section A: Physics and Chemistry*, 89-96, 1977

Effect of Femtosecond Laser Texturing on Roughness Characteristics of Tin Bronze Alloy

Bharatish A*[1], B S Suresh[1]

[1]*Department of Mechanical Engineering, RV College of Engineering®, Bengaluru*

Abstract

Femtosecond laser surface texturing of soft bearing materials such as tin bronze has gained greater attention in manufacturing community for various contact applications. This paper examines the effect of scanning speed and texture pitch on roughness characteristics of femtosecond textured high tin bronze alloy under lubricated conditions. These mainly include average roughness (R_a), root mean square roughness (R_q), skewness (R_{sk}) and Kurtosis (R_{ku}). Reciprocating wear test was conducted to assess the tribological performance of high tin bronze alloy at load conditions of 17, 27 and 38 N and constant frequency of 5 Hz. The correlations between the roughness characteristics and friction coefficient of high tin bronze alloy were assessed through regression analysis. Both scanning speed and pitch were found to be inversely related to Ra and Rq. The textures produced at higher pitch of 60 µm and scanning speed of 10 mm/s caused ~40 times higher kurtosis as against ~6 times achieved at 60 µm and 5 mm/s. The condition of higher kurtosis and negative skewness achieved at higher scanning speed and pitch could cause the improvement of lubrication conditions through reduced friction.

***Keywords**: Femtosecond laser, tin bronze alloy, surface roughness, kurtosis*

1. Introduction

In recent years, ultra short pulsed lasers are adopted for tailoring the surface properties of various metals, alloys and ceramics. Laser texturing is one of the surface modification processes adopted to reduce friction by producing different patterns in the form of micro-dimples or grooves Femtosecond laser surface texturing of soft bearing materials such as tin bronze has gained greater attention in manufacturing community for various contact applications. These include boundary lubricated bearings such as aircraft landing gear assemblies, control surface hinges and linkages [1]. Generally, bronze parts act as sacrificial components to protect the valuable steel components and becomes the major sources of friction and wear [2]. Since the surface roughness and topography strongly influence the tribological behavior of such soft contact interfaces especially under lubricated conditions, it is most vital to understand the influence of laser and groove geometrical parameters on the surface roughness characteristics to achieve better performance of mechanical components.

**Mail address: Bharatish A, Assistant Professor, Mechanical Engineering Department,*
RV College of Engineering®, Bengaluru – 59
Email: bharatisha@rvce.edu.in Ph:9886445035

Some of the commonly adopted surface roughness parameters are R_a, R_q, R_{sk} and R_{ku}. The most widely used roughness parameter for general quality control is the arithmetic average height parameter (R_a). Ra is meaningful for random surface roughness (stochastic) machined with tools that do not leave marks on the surface, such as sand blasting, milling and polishing. Rq corresponds to root mean square deviation of the assessed profile and is more sensitive to deviations from mean line than Ra. Eventhough, Ra and Rq provide a good general description of height variations, they do not provide the distinction between the peaks and valleys and hence surface with sharp peaks and deep valleys could not be characterized precisely [3]. Furthermore, other standard roughness parameters such as R_{sk} and R_{ku} provides realistic description of the surfaces. The skewness of the surface (R_{sk}) describes the asymmetry of the height distribution on the sampling length. Positive values of the skewness signify the high peaks spread on a regular surface while negative values are found on surfaces with pores and scratches as shown in Fig. 1. Rsk becomes vital in specifying honed surfaces and monitoring for different types of wear conditions. Rku is the measure of the sharpness of the profile peaks. If $R_{ku} < 3$, surface has few high peaks and low valleys (Platykurtic). If $R_{ku} > 3$, the surface has relatively many high peaks and low valleys (Leptokurtic) [4]

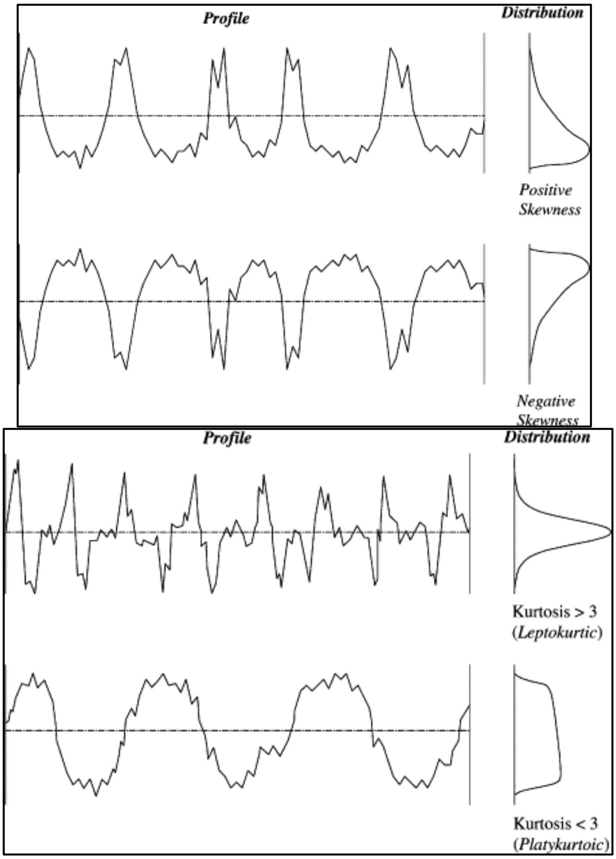

Fig. 1. a). Definition of Skewness and **b).** Kurtosis [4]

Some of the researchers have focused on influence of surface preparation on the friction and wear behavior of various metallic and ceramic surfaces. M. Sedlacek et al [5] reported the effect of surface preparation on roughness parameters and established a correlation between roughness parameters and friction coefficient. Disc type steel samples were examined in terms of different average surface roughness, using different grades of grinding, polishing, turning and milling. Lower roughness resulted in lower coefficient of friction under lubricated conditions. The same authors M. Sedlacek et al [6] investigated the effect of skewness and kurtosis parameters on the wear behavior of contact surfaces made of steel under dry and lubricated conditions. The authors reported that a higher value of Sku and a more negative Ssk results in lower friction under boundary lubrication conditions. G Lazzini et al [7] developed a correlation between areal roughness parameters and laser parameters (laser energy dose, repetition rate and scanning velocity) during surface texturing of 316L stainless steel adopted in food industry. The authors reported that increase in the laser energy dose results in average rise of height of the highest peaks and depth of the deepest dales. F Svahn et al [8] investigated the effect of surface roughness on the friction and wear behavior of carbon coatings containing tungsten and chromium. The friction was higher for rougher surfaces because of shearing of oxidized coating material deposited in the scratches. S Zhu et al [9] derived the correlations between dry or lubricated friction coefficient and bearing area ratio during turning, milling and grinding of steel samples. Positive correlation for dry friction coefficient and negative correlation for mixed lubrication coefficient and bearing area ratio was observed. V Podgursky et al [10] developed a correlation between the coefficient of friction and surface geometrical parameters such as average roughness, skewness and kurtosis during polishing of TiN, TiAlN and AlTiN coatings deposited on top of WC-Co substrates. The authors reported that that the coefficient of friction was inversely proportional to kurtosis, assuming positive skewness of the surface. B Podogornik et al [11] investigated the influence of laser texture parameters on kurtosis and skewness of the AISI 52100 steel surface and consequently coefficient of friction under lubricated conditions. The surface texturing was performed using Nd: YAG laser operated at an average power of 12.8 W, wavelength of 1064 nm, and frequency of 15 kHz. The authors reported that a higher kurtosis and a more negative skewness are obtained for semicircular grooves or dimples having larger depth, decreased density and size. X Jia et al. [12] fabricated nano patterns on ZnO crystal by adjusting the laser polarization combinations of multi-beam interference. J Chen et al. [13] investigated the influence of laser parameters such as beam diameter, pulse fluence, wavelength and number of pulses on the texture of aluminium surface by forming laser interferometry patterns. M M Calderon et al. [14] reported the formation of longitudinal and transversal LIPSSs on stainless steel surface at 2.71 J/cm2 fluence and 1 mm/s scanning speed resulting in 30 pulses per spot

Eventhough some of the authors have focused on analyzing the effect of surface texturing on friction and wear behavior of metals and ceramic coatings, the surfaces were prepared mostly with conventional techniques such as turning, polishing, milling and grinding, except [15]. The authors had also made an attempt to explore the possible correlation between surface geometrical parameters and frictional performance of various steel surfaces. With the rapid development of ultra short pulsed lasers, the surface texturing is more effective since high peak power intensities could produce minute structures in different materials ranging from polymers to semiconductors and metals [16]. The process is mainly controlled by various laser parameters such as laser fluence, scanning speed, pulse duration and number of pulses. Among these parameters, scanning speed effectively controls the material depth, material removal rate and plays an important role in producing textures with irregularities in the form of roughness, waviness and form errors. Also, texture geometrical parameters such as texture density can improve the wetting of the surface and support the formation of a lubrication film [11, 13]. The effect of femtosecond pulsed laser parameters on the surface roughness and friction performance of soft bearing materials such as tin bronze is not yet addressed so far. Hence, the present research focuses on investigating the effect of scanning speed and texture pitch on roughness parameters such as R_{sk} (skewness) and R_{ku} (kurtosis) and coefficient of friction of tin bronze under lubricated conditions.

2. Materials and methods

2.1 Specimen preparation

Sand-casted tin bronze alloy containing 12 wt. % tin was procured from M/s Meltech Alloys, Coimbatore. The casted rods of dimensions Φ 50 mm × 500 mm were grit blasted (20/40 mesh size) and then cut into square pieces of dimension of 25 mm × 25 mm × 5 mm in order to meet the experimental wear test rig requirements. The chemical composition of the casting was analyzed using Meta Vision tungsten arc spectrometer. The composition of the alloy was found to be within the range of ± 0.1 % wt from the nominal composition. The chemical composition of the sample is as shown in Table 1. The surface hardness of the samples containing 12 wt % tin was found to be 139.16 HV, which is averaged from six measurements. The testing conditions of 500 gf load and 10 s dwell time were adopted. The samples were polished to obtain the surface roughness of about 0.3 μm. Samples were cleaned with acetone prior to laser processing.

Table 1. Chemical composition of the sample

Element (%)	Cu	Sn	Pb	Zn	Fe	Si	Mn	Sb	P	S	Cr	Be	As
Sample	85.35	12.66	0.185	0.153	0.0054	0.014	0.01	0.013	0.142	0.012	0.01	0.002	0.002

2.2 Laser surface texturing with fs pulses

A commercial Ti: sapphire fs laser- Spitfire Ace power amplifier (12 W output power, 50ps - 100 fs pulse width, 10 kHz repetition rate) was employed to create micro-grooves on the samples. A near Gaussian laser beam at normal incidence was focused onto the tin bronze samples that were placed in processing chamber. The laser scanning speed could be controlled by the mirrors of galvanometer. An area of 20 mm × 8 mm was considered to generate linear micro groove textures, comprising of regularly spaced features. The experimental conditions are presented in Table 2.

Table 2. Experimental plan for fs laser surface texturing

Sl No	Texture (L)	Laser Power (mW)	Scanning Speed (mm/s)	Pitch (µm)
1	L1	100	10	40
2	L2	100	10	60
3	L3	100	5	40
4	L4	100	5	60
6	UL	0	0	0

Four types of textures with varying scanning speeds (5 and 10 mm/s) and pitch between the grooves (40 and 60 µm) were created on tin bronze sample having 12 wt % tin. The textured samples were designated as L1, L2, L3, and L4. The untextured sample was designated as UL5. Throughout the experiments, the laser power was maintained at 100 mW. The depth, width and roughness parameters of the grooves were measured using Bruker 3D Non-contact Profiler and presented in Table 3. The surface topography of the all the four textures and their associated cross-sectional profile (Y profile) are as shown in the Fig. 2 - 5.

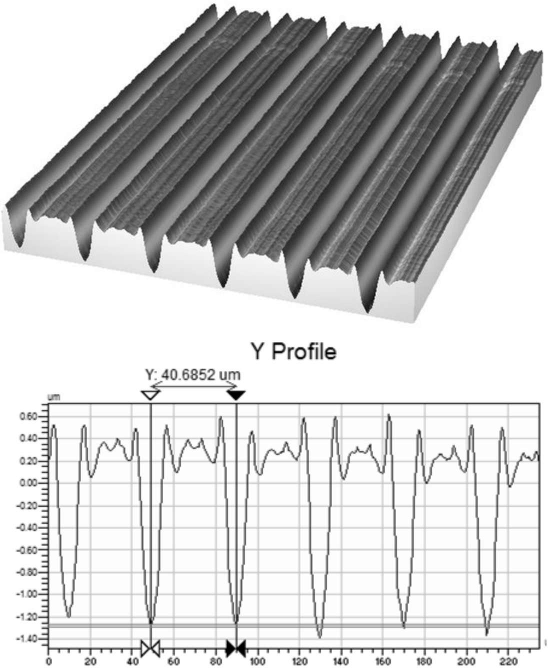

Fig. 2. **a).** Surface topography and **b).** Cross sectional profile of texture L1

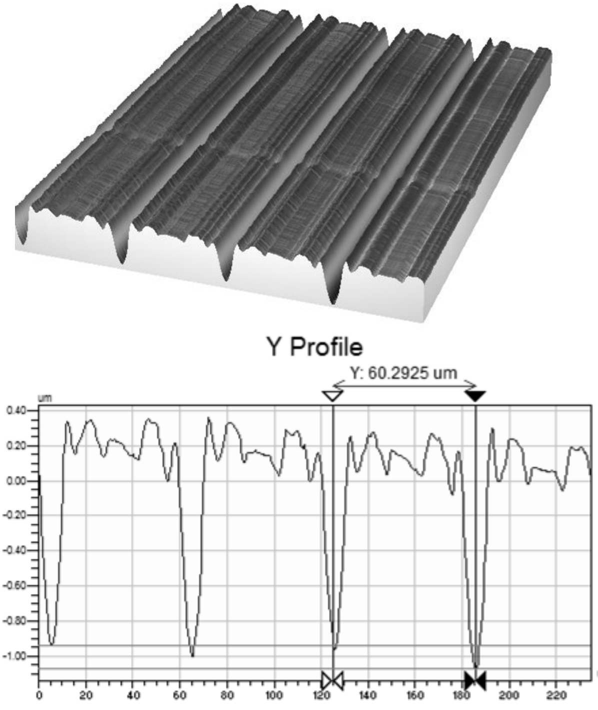

Fig. 3. **a).** Surface topography and **b).** Cross sectional profile of texture L2

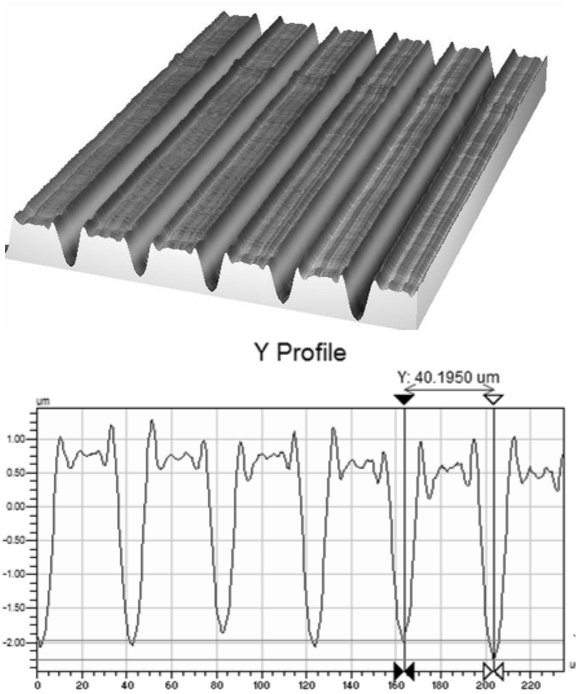

Fig. 4. a). Surface topography and **b).** Cross sectional profile of texture L3

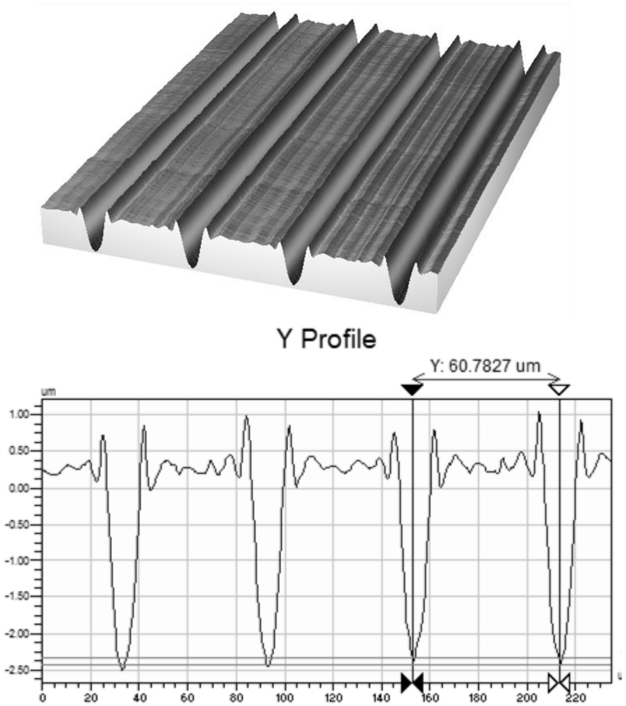

Fig. 5. a). Surface topography and **b)**. Cross sectional profile of texture L4

Table 3. Measured roughness characteristics of laser textures

Sl No	Texture (L)	Depth (μm)	Width (μm)	Measured Roughness Characteristics			
				Ra (μm)	Rq (μm)	Rsk	Rku
1	L1	1.66	12.21	0.44	0.545	-1.236	0.056
2	L2	1.29	12.41	0.237	0.342	-1.849	2.34
3	L3	2.77	14.21	0.826	0.993	-1.122	-0.277
4	L4	2.90	14.70	0.665	0.889	-1.632	1.242

2.3. Tribological Testing

The reciprocating ball-on-flat tests according to ASTM G133 standard were carried out using a customized wear test rig in order to assess the friction behavior of textured and untextured tin bronze surfaces slid against EN - 31 steel balls (60 HRC, Ra = 0.06 μm). The reciprocating wear test rig was adopted for performing tribological tests. The oscillating motion was provided by a controlled variable speed AC motor. An eccentrical scotch yoke mechanism was adopted for the adjustment of the stroke. The normal load was measured by a cantilever type load cell. The frictional force was acquired in the form of voltage output from piezoelectric transducer which was connected to flexure mechanism. The coefficient of friction was considered as ratio of frictional load to normal load and the sliding direction was chosen to be perpendicular to surface textures (grooves). The tribological test conditions were chosen based on review of literature and initial experiments, and are presented in Table 4.

The effect of load (17, 27 and 38 N) at reciprocating frequency of 5 Hz on coefficient of friction of all textured and untextured samples was reported. Hence, three conditions of wear parameters were tested on each of the textured (L1, L2, L23 and L4) and on untextured sample (UL5) constituting of total 15 experiments. These tests were carried out at oil lubricated conditions, 25ºC room temperature and 30 % relative humidity. For the lubricated tests, SAE 15W-40 oil was smeared on the surface only once well before the start of the experiment. Each experiment was performed with the combination of new track contacting with a new ball surface.

After each test, the ball and specimen were cleaned with acetone for 10 min and blown with dry air at 40ºC in order to remove any debris and oil droplets on the generated tracks.

3. Results and Discussion

3.1 Influence of scanning speed and texture density on Roughness parameters

Average surface roughness (Ra), root mean square (Rq), skewness (Rsk) and kurtosis (Rku) obtained for textured tin bronze samples are summarized in Table 3. The effect of scanning speed and texture pitch on Ra and Rq is as shown in Fig. 3. Increasing the pitch from 40 to 60 µm at constant higher scanning speed of 10 mm/s results in the decrease of Ra from 0.44 to 0.237 µm. When the scanning speed was reduced from 10 mm/s to 5 mm/s, Ra drastically increased from 0.237 to 0.826 µm. Increase in pitch from 40 to 60 µm at constant lower scanning speed of 5 mm/s resulted in the decrease of Ra from 0.826 to 0.665 µm. Thus, both scanning speed and pitch were found to be inversely related to Ra. Rq also exhibited the same trend as Ra at higher scanning speed of 10 mm/s. At lower scanning speed of 5 mm/s, Rq decreased slightly from 0.933 to 0.889 µm. Hence, increasing the pitch and producing textures at lower scanning speed had little effect on Rq.

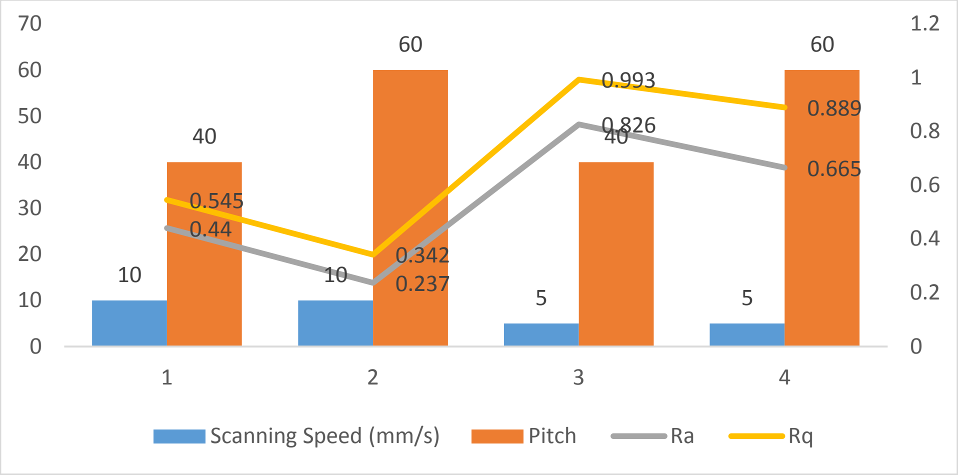

Fig. 3. Effect of scanning speed and pitch on Ra and Rq

The effect of scanning speed and pitch on R_{sk} and R_{ku} are as shown in the Fig. 4. At higher scanning speed of 10 mm/s, increasing the pitch from 40 to 60 µm leads to more negative value of Rsk i.e. decrease in Rsk from -1.236 to -1.849. But, Rku increased from 0.056 to 2.34 by increasing the pitch from 40 to 60 µm. Decreasing the scanning speed from 10 to 5 mm/s resulted in an increase of Rsk from -1.849 to -1.122. However, R_{ku} decreased from 2.34 to -0.27, thus attained a negative value. Increasing the pitch at lower scanning speed of 5 mm/s leads to more negative value of R_{sk}. R_{ku} also changed back from negative (-0.2769) to positive (1.242). The effect of increasing the pitch is more evident at higher scanning speed of 10 mm/s, where an increase in pitch from 40 to 60 µm resulted in ~40 times higher kurtosis as against ~6 times achieved at lower scanning speed of 5 mm/s. Increase in pitch provides higher surface area and higher scanning speed leads to lower degree of interaction of laser with material due to the which the kurtosis increases. Thus, higher kurtosis and negative skewness could be obtained at higher scanning speed and higher pitch.

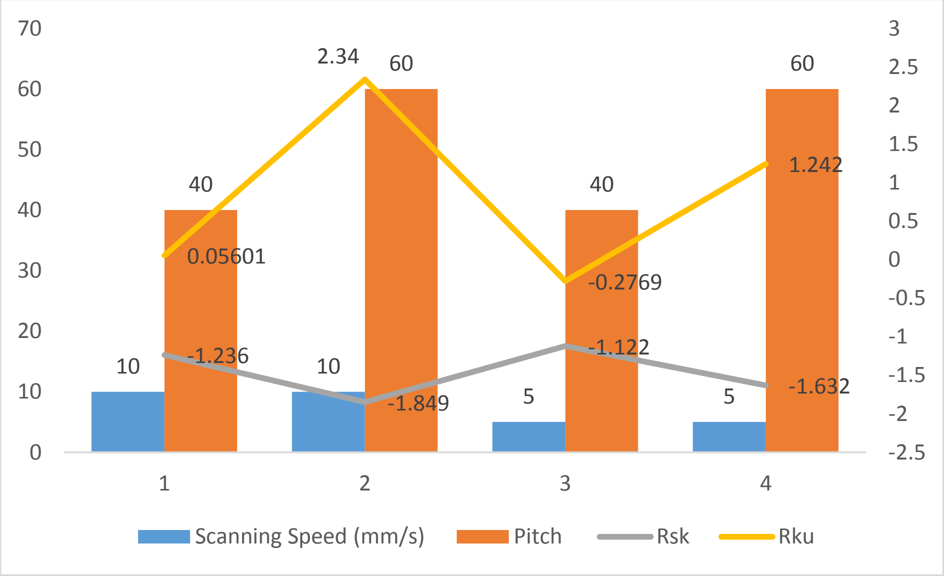

Fig. 4. Effect of scanning speed and Pitch on R_{sk} and R_{ku}

3.2 Influence of scanning speed and texture density on Coefficient of Friction

The effect of scanning speed and texture density on coefficient of friction (COF) is as shown in Fig. 5. The coefficient of friction was evaluated at frequency of 5 Hz and load conditions of 17, 27 and 38N. At higher scanning speed of 10 mm/s, increase in pitch from 40 to 60 µm leads to decrease in COF from 0.098 to 0.091 at a load of 17N. With decrease in scanning speed from 10 to 5 mm/s, the COF increased from 0.091 to 0.17. Again increasing the pitch leads to decrease in COF. When the load is increased from 17 to 27 N, the COF remains stable irrespective of change in pitch from 40 to 60 µm at higher scanning speed of 10 mm/s. With decrease in the scanning speed from 10 to 5 mm/s, COF increases from 0.091 to 0.105. Increasing the load from 27 to 38 N leads to decrease in COF from 0.0921 to 0.083 at higher scanning speed of 10 mm/s. Now, increasing the pitch from 40 to 60 µm further causes a decrease in COF from 0.083 to 0.0725. The COF decreases by ~15% with increase in load from 17 N to 38 N for the textures produced at higher scanning speed (10 mm/s) and higher pitch of 60 µm. For the textures produced at lower scanning speed (5 mm/s), the same conditions leads to a decrease in COF by ~20%. However, the textures produced at lower scanning speed of 5 mm/s and pitch of 40 µm exhibited ~48% decrease in COF when the load was increased from 17 to 38N. The friction performance of textured and untextured specimen at 5 Hz and 38 N is as shown in Fig. 6. All the textures (L1 to L4) exhibited COF less than that of untexured ones. After completion of 2500 cycles, L2 and L4 textures attained a more stable state when compared to that of L1 and L3. Thus, textures formed at a pitch of 60 µm and a scanning speed of 5 mm/s reduced the friction coefficient from untextured one (0.091) by ~25%.

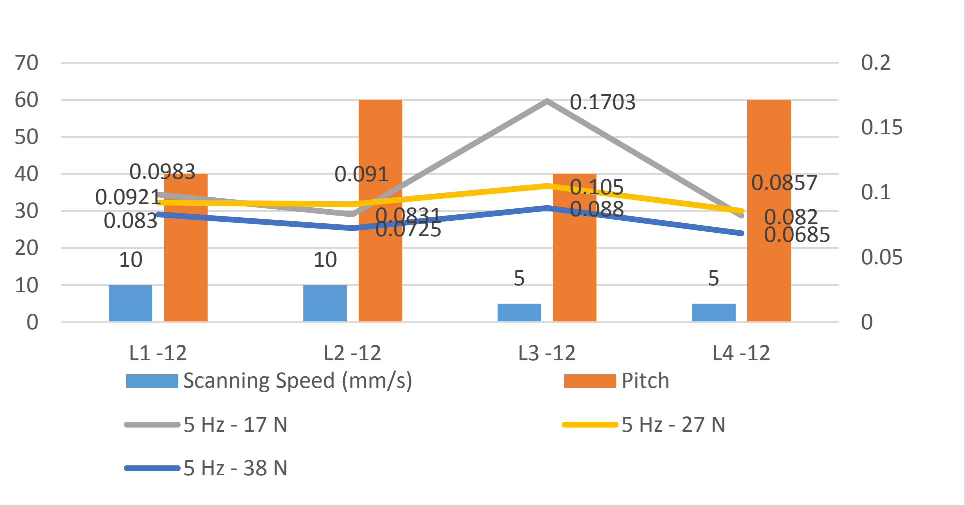

Fig. 5. Effect of scanning speed and texture density on coefficient of friction (COF)

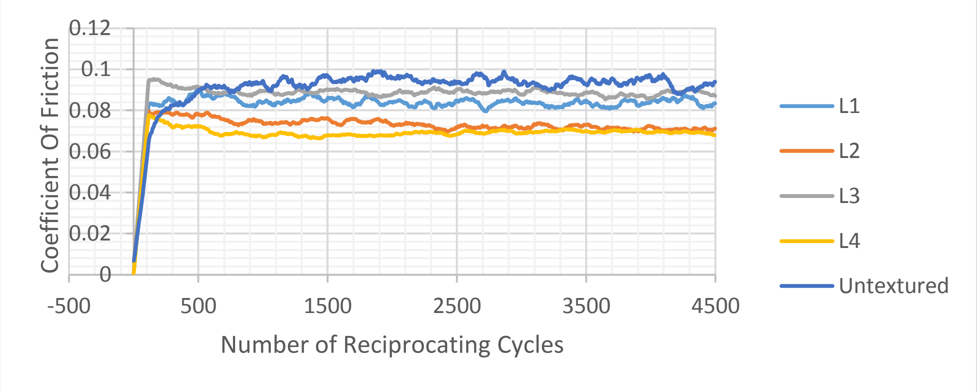

Fig. 6. Friction performance of textured and untextured specimen

3.3 Correlation between the Roughness parameters and Coefficient of Friction

Under lubricated conditions, the correlation between the roughness parameters and coefficient of friction of tin bronze is established. Fig. 7 predicts the relation of average surface roughness Ra with coefficient of friction evaluated at frequency of 5 Hz and three load conditions mainly 17, 27 and 38N. A polynomial curve fit with R-squared value mainly indicates the degree of correlation between the two factors. It can be observed that increase in load from 17 N to 38 N gradually decreases the correlation between Ra and COF. Increase in R_a leads to increase in COF at lower load of 17 N. Lowest COF of 0.0831 corresponds to lowest Ra of 0.237 for L2 sample i.e. texture produced at higher pitch and higher scanning speed. Thus, at higher loads of 27 N and 38 N, increase in R_a do not show much effect on COF. The same trend is even observed between R_q and COF as shown in the Fig. 8. The correlation gets completely deteriorated at higher load of 38 N which is indicated through lowest R-squared value. Thus, Ra and Rq are not sufficient enough to predict the friction performance at higher loads.

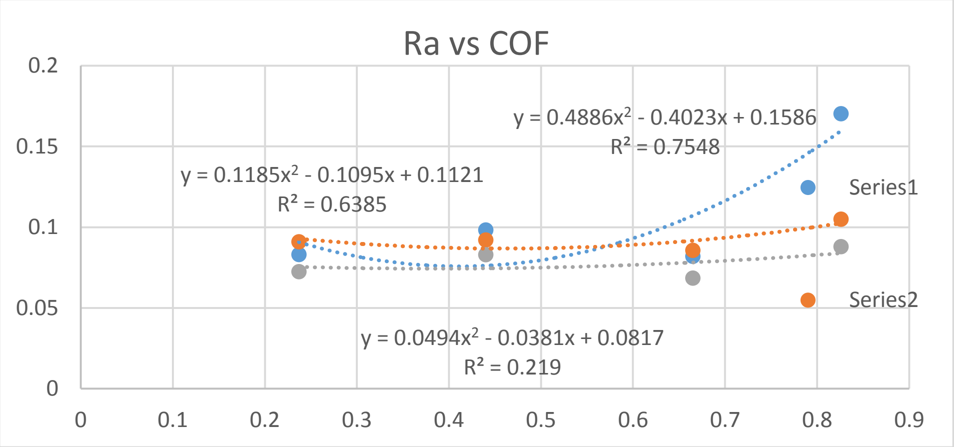

Fig. 7. Correlation of Ra with COF predicted at 17, 27 and 38 N

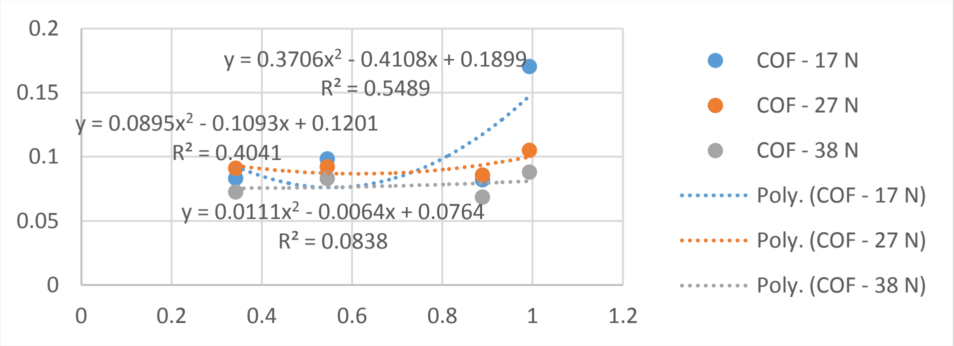

Fig. 8. Correlation of Rq with COF predicted at 17, 27 and 38 N

The correlation between the skewness (R_{sk}) and COF is as shown in Fig. 9. At all load conditions, skewness was found to be inversely related to COF. More negative the skewness lesser is the coefficient of friction under lubricated conditions. At higher load of 38 N, higher negative skewness (Rsk) of -1.849 was obtained for L2 sample having minimum COF of 0.0725. However, COF attained maximum value of 0.1703 when skewness became less negative (-1.122) for L3 texture produced at lower scanning speed and lower pitch. The correlation between Rsk and COF was found to increase with increase in load from 17 N to 38 N which is indicated by high R-squared values i.e. 83% at 17N, 94% at 27N and 98.23% at 38 N. This clearly indicates that the deep valleys and grooves that are characterized by negative skewness act as lubricant reservoirs [20] and causes the decrease in friction coefficient at higher loads. The effect of

R_{ku} on COF is as shown in the Fig. 9. The highest skewness of 2.34 was obtained for L2 sample having COF of 0.0725 at a load of 38N. Thus texture produced at higher scanning speed and higher pitch leads to higher kurtosis and negative skewness. The surface morphology of L2 texture is as shown in the Fig. 10. The uniformity of texture, waviness and roughness patterns obtained at certain area indicated the high quality of textures. However, kurtosis value remained less than 3 which also confirms that higher scanning speed (10 mm/s) will cause lower groove depth. Negative kurtosis of -0.2769 was found for L3 sample i.e texture produced at 5 mm/s and 40 µm. Thus, texture produced at lower scanning speed and lower pitch corresponds to negative kurtosis and less negative skewness. The corresponding surface morphology of L3 texture is as shown in the Fig. 12. The non-uniform patterns of texture, waviness and roughness obtained at certain area indicated the decreased quality of textures. Similar to R_{sk}, the correlation between R_{ku} with COF increased with increase in load i.e. 89% at 17N, 78.3% at 27N and 99.25% at 38 N.

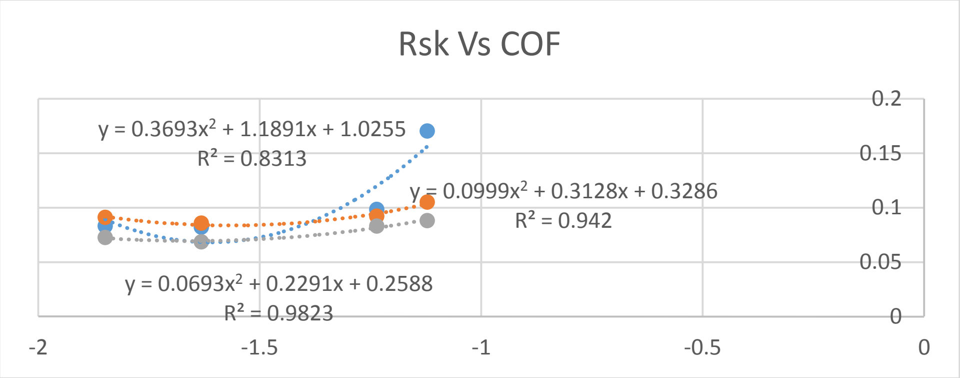

Fig. 9. Correlation of Rsk with COF predicted at 17, 27 and 38 N

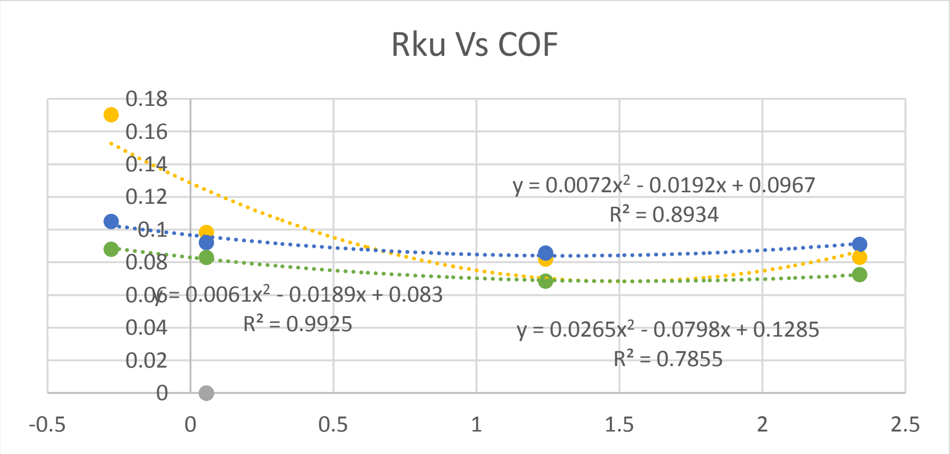

Fig. 10. Correlation of Rsk with COF predicted at 17, 27 and 38 N

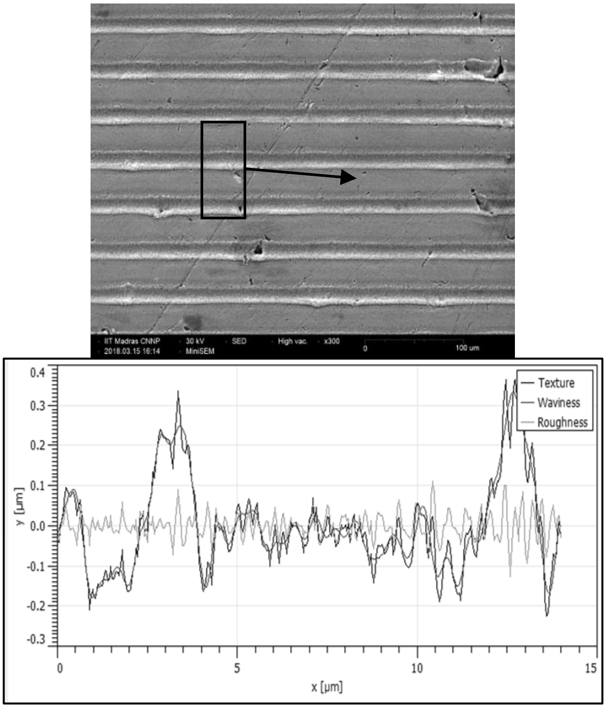

Fig. 11. Surface morphology of L2 texture (Higher scanning speed and higher pitch)

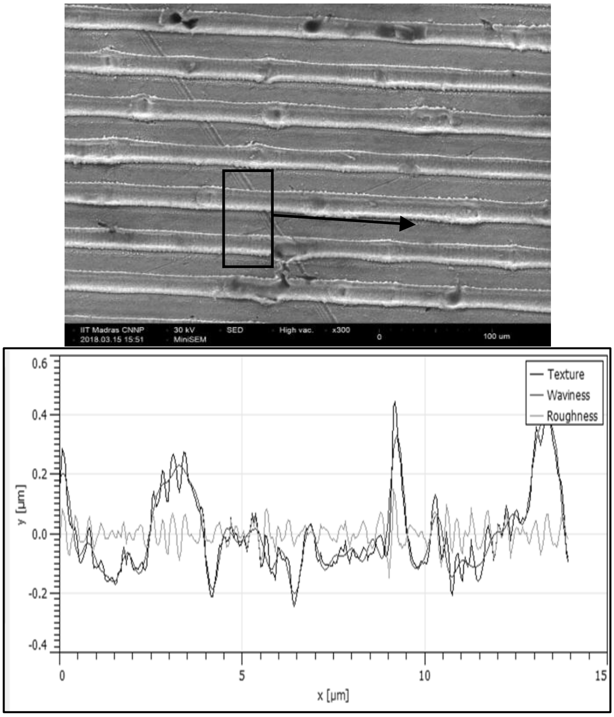

Fig. 12. Surface morphology of L3 texture (Lower scanning speed and lower pitch)

4.0 Conclusions

Femtosecond laser surface texturing of high tin bronze alloy was carried out in order to assess the effect of scanning speed and texture pitch on surface roughness parameters such as Ra, Rq, Rsk and Rku. While the scanning speed and pitch were found to be inversely correlated with Ra, increasing the pitch and producing textures at lower scanning speed had little effect on Rq. Textures produced at higher pitch and higher scanning speed showed ~40 times higher kurtosis as against ~6 times produced at lower scanning speed. The correlations between Ra and COF, and Rq with COF did not agree well at higher loads whereas the same achieved between Rsk and COF, and R_{ku} and COF were completely agreeable indicated by high R-squared values. Maximum COF was attained for the texture produced at lower scanning speed and lower pitch that corresponded to negative kurtosis and less negative skewness. Also, the textures produced at higher scanning speed and higher pitch leads to higher kurtosis and negative skewness which indicates the improved lubrication conditions. Thus, the analysis of roughness parameters before and after the tribological assessment could lead to better understanding of contact applications.

References

1. William A. Glaeser, Copper base bearing materials, Materials for Tribology, Chapter 2, pp 46 – 68, ISBN: 978-0-444-88495-4
2. William A. Glaeser, Soft metal bearing materials, Materials for Tribology, Chapter 3, pp 46 – 68, ISBN: 978-0-444-88495-4
3. James B. Taylor, Andres L. Carrano, Satish G. Kandlikar, Characterization of the effect of surface roughness and texture on fluid flow—past, present, and future, International Journal of Thermal Sciences, 45 (2006), 962–968.
4. E.S.Gadelmawla, M.M.Koura, T.M.A.Maksoud, I.M.Elewaa, H.H.Solimand, Roughness parameters, J. Mater. Process. Technol, 123, 133-145, 2002
5. M. Sedlacek, B. Podgornik, J. Vizintin, Influence of surface preparation on roughness parameters, friction and wear, Wear, 266 (2009) 482–487
6. M. Sedlacek, B. Podgornik, J. Vizintin, Correlation between standard roughness parameters skewness and kurtosis and tribological behavior of contact surfaces, Tribology International, 48, 2012, 102–112
7. G Lazzini, L Romoli , L Blunt, L Gemini, Design and characterization of textured surfaces for applications in the food industry, Surf. Topogr.: Metrol. Prop. 5 (2017) 044005
8. F. Svahn, Kassman-Rudolphi Åsa, E. Wallén, The influence of surface roughness on friction and wear of machine element coatings, Wear 254 (11) (2003) 1092–1098
9. Shengguang Zhu, Ping Huang, Influence mechanism of morphological parameters on tribological behaviors based on bearing ratio curve, Tribology International 109 (2017) 10–18

10. V. Podgursky, E. Adoberga, A. Surzenkova, E. Kimmaria, M. Viljus , V. Miklib, M. Hartelt, R. Wäsche, M. Símad, P. Kulu Dependence of the friction coefficient on roughness parameters during early stage fretting of (Al,Ti)N coated surfaces, Wear 271 (2011) 853– 858
11. B Podogornik, M Sedlacek, Performance, Characterization and Design of Textured Surfaces, Journal of Tribology, 134, 041701-1, 2012
12. Xin, J., Lingling, D.: Fabrication of complex micro/nanopatterns on semiconductors by the multi-beam interference of femtosecond laser. Phys Procedia. 56, 1059–1065 (2014)
13. Chen, J., Sabau, A.S., Jones, J.F., Hackett, A.C., Daniel, C., Warren, D.: Aluminum surface texturing by means of laser interference metallurgy. In: Hyland, M. (ed.) Light Metals 2015. Springer, Cham (2015)
14. Martinez-Calderon, M., Manso-Silvan, M., Rodriguez, A., Gomez-Aranzadi, M., Garcia-Ruiz, J.P., Olaizola, S.M., Martin-Palma, R.J.: Surface micro- and nano-texturing of stainless steel by femtosecond laser for the control of cell migration. Sci Rep. 6(1), 36296 (2016)
15. Koji Sugioka, Ya Cheng, Ultrafast lasers - reliable tools for advanced materials processing, Light: Science & Applications, Vol 3, page e149 (2014)
16. Chow, T. S., 1998, Wetting of Rough Surfaces, J. Phys.: Condens. Matter.10, pp. L445–L451

Flame Assisted Liquid Spray Pyrolysis for Thin Film Deposition

Divakara SG[1*], Ravishankar Holla[2], Meghanatha KL[2], Ranjith Kumar HN[2]
[1]*Department of Chemistry, RV College of Engineering®, Bengaluru*
[2]*Department of Electronics and Communication Engineering, RV College of Engineering®, Bengaluru -59*

Abstract

Spray pyrolysis offers significant potential for the synthesis of different kinds of functional nano-structured materials. It is a highly scalable technology and is suitable for continuous film coating. Thin films of nanomaterials sprayed on different substrates are worthwhile for novel applications. Spray pyrolysis system mainly consists of a precursor chamber for loading the solution; spray nozzle unit, compressor and heating unit. Cost effective automatic flame assisted liquid spray pyrolysis system was fabricated in which control arrangements were managed by a microcontroller based control circuit. In the preliminary tests, ZnO thin films were synthesized and characterized by SEM and XRD. Presence of Wurtzite ZnO structure was evidenced and particle size distribution showed size variation between 35 and 60 nm.

Keywords: *Spray pyrolysis, Zinc oxide, thin films, microcontroller*

1.0 Introduction

Thin films have gained great importance in applications related to several real-world problems as a two dimensional system in microelectronics, antennas, array antennas, optical electronics, energy generation and energy conservation strategies [1-3]. Their material costs when compared to corresponding bulk material, are very small, yet perform the same function when it comes to surface processes. The various physical and chemical methods of fabricating film coating for required thickness are namely pulsed laser deposition, electron beam sputtering, thermal evaporation, vacuum deposition, chemical vapor deposition, co-precipitation, sol-gel, chemical bath deposition, spray pyrolysis etc. Spray pyrolysis doesn’t need high vacuum environment making it very much suitable for use when low complexity, low cost is needed. Precursors used for this spray pyrolysis isn't expensive comparatively [4-5].

The properties of a film are generally sensitive to their structure, thickness, surface states and morphology. In spray pyrolysis, controlling of spray time and substrate surface temperature during deposition results in variation of properties of the deposited film [6]. A microcontroller system, low cost and with almost nil mechanical arrangement along with a display and keyboard unit ensures

---

**Mail address: Divakara S G, Assistant Professor, Department of Chemistry,*
RV College of Engineering®, Bengaluru – 59,
Email: divakarsg@rvce.edu.in, Ph.: +91 8660159619

reasonable control over the spray parameters [7]. In the last 10 years, Spray pyrolysis technology has developed substantially, attracting many researchers to synthesize a wide range of complex materials for various applications. Flexibility in producing nano structured powder and films of pure or mixed metal oxides have enabled advancements in spray pyrolysis equipment, reaction engineering and precursor chemistry. In order to prepare new materials and with unique material morphologies, custom designed low cost spray pyrolysis equipment is proposed. In this paper, fabrication of flame assisted liquid spray pyrolysis equipment and synthesis of ZnO powders or films through a pyrolysis process is presented. The aerosols of the precursor solution is generated by pneumatic system and used during the spraying process. The phase and surface morphology were studied using X-ray diffraction (XRD) and scanning electron microscope (SEM) measurements respectively.

2.0 Spray Pyrolysis System

The spray pyrolysis technique mainly involves the aerosol generation from various precursor solution of chemical compounds and very rapidly passing through a hot zone or spraying on to a hot substrate in a furnace. It consists of two basic steps, an atomizer, which creates the droplets, after that those droplets fall of on the heated substrate and evaporates the solvents with solid particles left behind. In flame assisted liquid spray pyrolysis technique, deposition of a film is performed by passing of precursor's flux across a direct flame and directing on to the surface of the substrate. Spraying droplets of precursor solution at high temperature onto the substrate creates a coating on the substrate surface [8]. The high temperature of single / dual flame is also used for evaporation and decomposition of sprayed liquid precursors to achieve the gas-phase reaction to form particles in nanometers range [4, 8]. Fig. 1 demonstrates the schematic diagram of spray pyrolysis system having temperature controlling unit, electronic unit, flow and pressure controlling units. Equipment was fitted with accessories required for controlling the flame during the process. Spray nozzle unit is fitted onto a motorized linear movement stage.

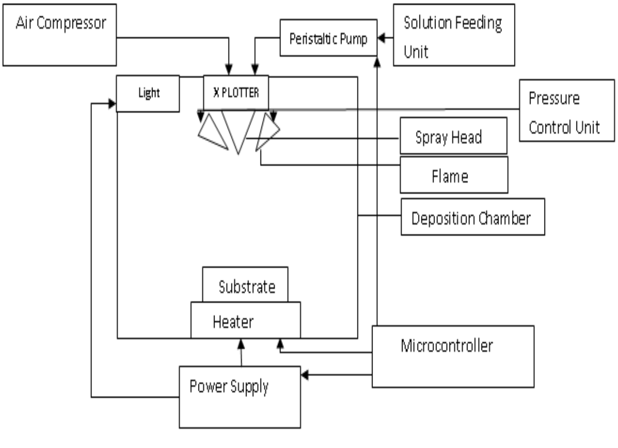

Fig. 1. Schematic representation of Spray pyrolysis system

Hot plate with temperature controlling arrangement and control units for gas and liquid flow were fixed in a stainless steel box.

The process of spraying a nano or sub-micron size particle involves 3 steps, out of which the first step is atomization. Their material costs when compared to corresponding bulk material, are very small, yet perform the same function when it comes to surface processes. Out of the various type of available atomizers, easiness of control and less cost involved resulted in selection of air blast atomizer (pneumatic) for the system. The limitation of this unit is in producing the droplets of uniform micrometer or nanometer size and control on the distributions of the droplets [8]. The solution spray using ultrasonic nebulizer instead of traditional atomizers enables production of good quality of films or monodispersive nanomaterials in the form of fine powders. But due to high cost involved, an air blast atomizer was used [9]. The second step of the process is on control over the spray. As the spray time increases, amount of droplets that would be deposited on the substrate from the spray head increases. For this, the atomizer itself has an air and solvent controlling option so that we can control the droplets. Temperature control is the final part of the process. The burner which produces flame using an oxy-LPG gas mixture was mounted near to the spray nozzle and normal heater which heats up to 400^{o}C was kept inside the chamber. Additional burner was also mounted near nozzle to provide required temperature and used depending on the application. As the droplets reach the heated substrate, the solvent is evaporated and the residual chemical compound sits on the surface of the substrate.

The air compressor and peristaltic pump used is shown in Fig. 2. The spray nozzle gets predetermined pressurized air and precursor solution using the control accessories. X direction movement of the spray gun was used to ensure uniform coating and is controlled by a unit consisting of a microcontroller [10]. A heater, heats the substrate and its temperature control is done using a thermocouple which senses the temperature of the surface of the substrate and flame is turned ON if required. The complete system is housed inside a stainless steel chamber. The exhaust fan was used to flush out the gasses in the chamber which are produced during the synthesis of material.

A. Flow and Pressure Control

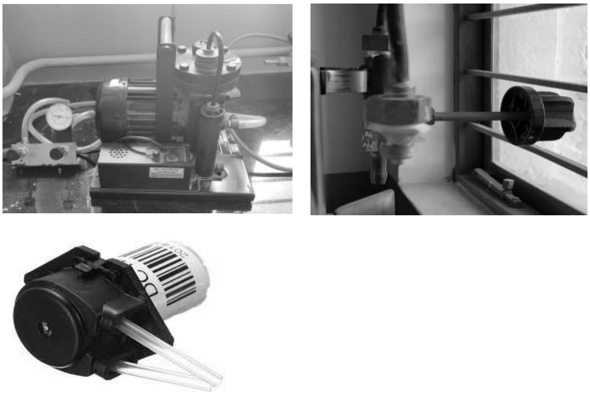

Fig. 2. Air compressor, gas control and peristaltic pump

Air compressor supplies pressurized air and peristaltic pump supplies precursor solution to the spray atomizer nozzle [11]. The high pressured air from compressor was regulated and was measured using the meter before it was supplied to the spray nozzle. The precursor solution was supplied to mixing chamber using a positive displacement pump which pumps from 0-50 ml/min depending on the voltage supplied to it. Finally the spray nozzle at predetermined constant pressure and flow rate of air and solution was sprayed on to substrate.

B. Temperature Controlling Unit

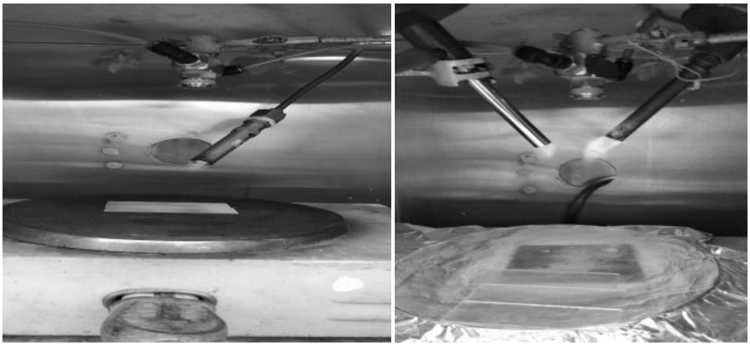

Fig. 3. Single and double flame unit fitted next to spray nozzle inside the chamber

One of the most important parameters to be controlled during the processes is the temperature inside the furnace because droplets drying, decomposition, crystallization, and grain growth strongly depend on this parameter [12]. Fig. 3, shows the temperature controlling unit with a normal heater which heats up to 400^{o}C and mounted flame burner units for the synthesis. The temperature of the hot plate surface was sensed using thermocouple and was controlled to desired level using a dedicated controller unit. The required intensity level of the flame was manually controlled using the control accessories fitted with the equipment. Depending on the application and precursor solution, we used only heater or flames for conversion of the salt into the metal oxide which occurs through pyrolysis reaction.

C. Electronics unit

Electronics unit had two parts namely microcontroller and x plotter. X plotter moves the spray head in x direction to achieve uniform coating on the substrate. The x plotter had a thread rod, spray head holder, stepper motor. To control the stepper motor, the microcontroller unit was designed and fabricated. The stepper motor was made to rotate in clockwise or counter clockwise direction to control the linear motion of a spray nozzle. The required power was supplied to peristaltic pump, microcontroller, heater, light, air compressor and stepper motor by power supply unit.

D. Complete Setup

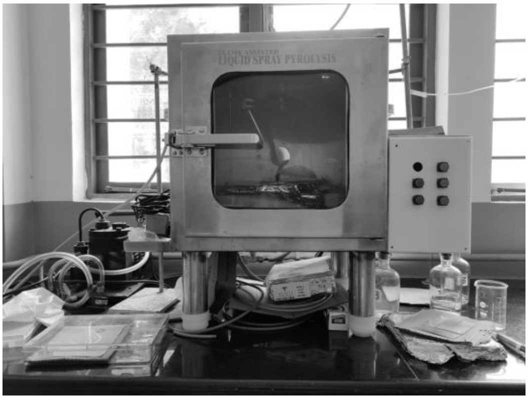

Fig. 4. Flame assisted liquid Spray pyrolysis chamber

All the units were fixed in a stainless box whose dimension is 15.5 X 15.5 inch. Fig.4 shows the front view of the complete set up.

3.0 Experimental Details

3.1 Material preparation

Synthesis and characterization of ZnO thin films were carried out to study the reaction parameters influence in a spray chamber with flame. A detailed design and experimental setup were discussed previously. Experimental apparatus consists of a spray nozzle containing a capillary tube (0.3 mm diameter), a furnace and an atomizer. An amount of 8 g of Zinc acetate dihydrate (ZnAc) dissolved in 75mL of methanol and 25 mL of water at room temperature and stirred for 20 min till solution becomes transparent. Few drops of acetic acid were added. The precursor solution fed using a voltage controlled peristaltic pump through the capillary, thus allowing the system to spray ultrafine droplets. The spray was ignited with flame with (propane (C_3H_8, 99.5%)) fuel and O_2 oxidizer. Propane was fed at 1 lpm and the amount of oxygen for its combustion in 6 lpm. Deposition time, substrate temperature, and air flow rate were kept constant during the whole deposition process at 10 minutes (3 ml/min flow), 300°C, and 25 ml min^{-1} respectively. The compressed air with controlled pressure was used to deliver aerosols to the substrate. Microscope glass slides were used as substrates, which were cleaned in acid and alcohol and then dried under air stream. The distance between the spray nozzle and the substrate was 17 cm. Finally, the material was annealed at 200 ºC for 1hour.

3.2 Characterization

XRD characterization (Shimadzu MAXima XRD -7000) gave the crystallinity of synthesized samples with Cu Kα radiation(λ = 0.1541 nm) at Bragg's angle ranging from 20^{o} to 80^{o} with 1^{o} per minutes for better resolution. The morphology of such samples was observed on a scanning electron microscopy (TESCAN-VEGA3 LMU).

4.0 Results and Discussion

Aerosols of the prepared ZnO precursor solution were sprayed as a fine mist into a flame from the nozzle and deposited onto the heated substrate. Initially, ZnO powders were prepared with Zinc acetate dihydrate precursor in order to understand how the chamber conditions, gas flow, and precursor solution flow affect morphology, particle size distribution, and crystalline phases of the deposited film or powder. Morphology and phase structure of ZnO was studied in single and double flame keeping all other conditions constant.

Using the spray head, an aqueous Zinc acetate dehydrate metal salt solution was sprayed as a fine mist pointing to the flame. As the solvent burns inside the flame, small droplets were formed. The conversion of the salt into the metal oxide occurs upon the pyrolysis reaction and Zinc metal oxide atoms aggregate into nanoparticles, which were then collected on a heated glass substrate. Very short residence times, typically a few seconds was enough for the formation of spherical nanoparticles. Fig. 5, shows scanning electron microscopy (SEM) image of the sample synthesized with a single flame. It demonstrates that the typical products consist of a large quantity of dispersed spherical shaped nanoparticles. The size of the nano structure was with a diameter of about 40-50nm. The phase structure of the as-synthesized samples was further characterized using powder XRD. Fig. 6, shows the XRD patterns of the ZnO synthesized under single flame. The XRD results represented that the zinc oxide nanoparticles exhibits high crystallinity of hexagonal Wurtzite crystal structure. The diffraction peaks located at 31.84°, 34.52°, 36.33°, 56.71°, 62.96°, 68.13°, and 69.18° have been keenly indexed as hexagonal Wurtzite phase of ZnO(JPCDS card number: 36-1451) [13].

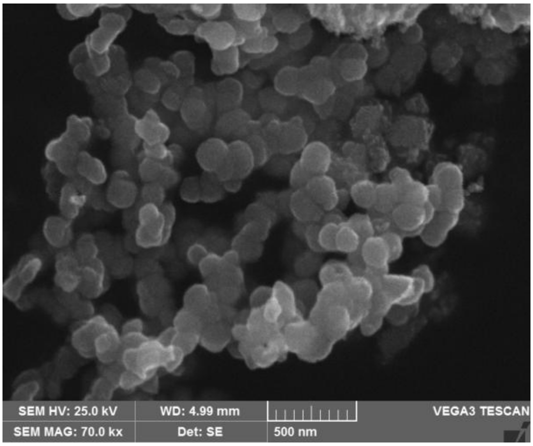

Fig. 5. SEM images of the ZnO films prepared using 0.35M Zinc acetate solution

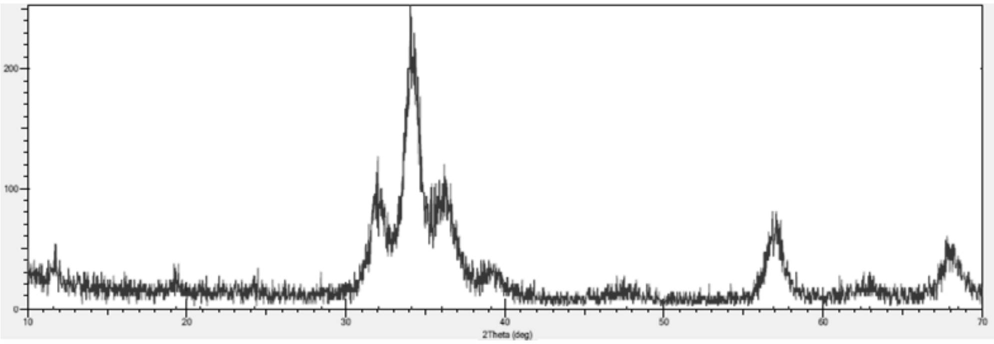

Fig. 6. XRD spectra of ZnO films with a thickness of around 500 nm.

An in house built spray pyrolysis deposition system consists of stainless steel chamber, a door with see through glass, substrate holder with heater, motor for linear motion, temperature controller, spray gun, peristaltic pump, air and solution flow control meters. It is observed that often the properties of deposited thin films depend on the preparation conditions. The system allowed variation of process parameters namely (i) spray gun nozzle to substrate distance, (ii) carrier gas flow rate, (iii) deposition time, (iv) solution flow rate, (v) substrate temperature, (vi) spray gun nozzle diameter and (vii) spray solution concentration. The quality of the thin/thick films and powder can be tuned by the optimizations of above process parameters. The reaction parameters such as temperature of substrate, flame temperature and the precursor solution composition also play crucial roles in controlling the size and morphology of the ZnO products. The influence of many operating conditions of the synthesis apparatus were optimized or kept constant and only the role of flame units upon the morphology of the nanostructured material has been preliminarily studied. To investigate the influence of flame in the formation of ZnO nanostructures, samples were also synthesized with participation of two flames under the same conditions. Fig. 7, shows the SEM images ZnO nanoparticles in the diameter range of 40 to 60 nm. The sample was found to be agglomerated compared to film prepared under single flame.

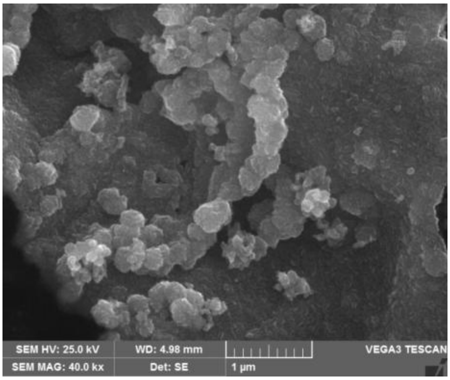

Fig. 7. SEM images ZnO nanoparticles prepared under use of dual flame.

4.0 Conclusions

Spray Pyrolysis equipment was designed and implemented, used for coating of ZnO thin films. This is a low cost though an efficient method that can be used for the deposition of films or synthesis of various nanopowders. The employment of an ultrasonic nebulizer instead of a conventional nozzle in the experimental set-up will shows good stability and reproducibility of the films or the powder produced. Further, interfacing with the computer will also increase its accuracy and control. In the preliminary tests of the equipment, deposited ZnO thin film showed size variation between 35 and 60 nm. Through XRD and SEM, the presence of wurtzite ZnO structure was evidenced which is suitable for photo catalysis applications, solar cell fabrication etc. The obtained results are promising and encourage the use of the designed experimental apparatus for future work in the field of controlled nanomaterial's synthesis and allow the investigation of a wide variety of nanostructured metal oxides.

Acknowledgement

Authors would like to acknowledge Interdisciplinary Research Center (IDRC) and Department of Chemistry, R. V. College of Engineering, Bengaluru for their help in the implementation of the Spray Pyrolysis equipment and characterization of the thin films.

References

1. Ciro Falcony, Miguel Angel Aguilar-Frutis, Manuel García-Hipólito, Spray Pyrolysis Technique; High-K Dielectric Films and Luminescent Materials:A Review, *Micromachines*, 9 (8), 414, 2018
2. J Park, J K Kim, J H Hong, J S Cho, S Park, Y C Kang, Advances in synthesis and design of nanostructured materials by aerosol spray processes for efficient energy storage, *Nanoscale*, 1-44, 2019

3. Leng, Jin, Wang, Zhixing, Wang, Jiexi, Wu, Hong-Hui, Yan, Guochun, Li, Xinhai, Guo, Huajun, Liu, Yong, Zhang, Qiaobao, Guo, Zaiping, Advances in nanostructures fabricated via spray pyrolysis and their applications in energy storage and conversion, *Chem. Soc. Rev.*, 48, 3015-3072, 2019
4. A S Enigochitra, P Perumal, C Sanjeeviraja, D Deivamani, M Boomashri, Influence of substrate temperature on structural and optical properties of ZnO thin films prepared by cost-effective chemical Spray Pyrolysis Technique, *Superlattices and Microstructures*, 90, 313–320, 2016
5. M Langlet, J C Joubert, Chemistry of Advanced Materials; Rao, C.N.R., *Ed.; Blackwell Science: Oxford, UK,* 1993; Chapter 4; ISBN 0-632-03385-1.
6. S S Omprakash, S K Naveen Kumar, Fabrication of Custom-Designed and Cost-Effective Spin-Spray Pyrolysis Unit, *International Journal of Engineering and Advanced Technology*, 9 (1), 2249 – 8958, 2019
7. M A Munjer, M F Usain, M H Rahaman, M Z Rahaman, Fabrication of cost effective automatic controller for spray pyrolysis technique to deposit thin films, *2012 7th International Conference on Electrical and Computer Engineering*, date:20-22-2012.
8. Saeed Rahemi Ardekani, Alireza Sabour Rouh Aghdam, Mojtaba Nazari, Amir Bayat, Elnaz Yazdani, Esmaiel Saievar-Iranizad, A comprehensive review on ultrasonic spray pyrolysis technique: Mechanism, main parameters and applications in condensed matter, *Journal of Analytical and Applied Pyrolysis*, 141, 2019, 104631, ISSN 0165-2370.
9. V Kumari, A Mittal, J Jindal, S- N- and C-doped ZnO as semiconductor photocatalysts: A review, *Front. Mater. Sci.* 13, 1–22, 2019
10. L Filipovic, S Selberherr, G C Mutinati, E Brunet, S Steinhauer, A K¨ock, J Teva, J Kraft, J Siegert, F Schrank, Modeling Spray Pyrolysis Deposition, *Proceedings of the World Congress on Engineering*, 2, July 2013
11. M D Sifuthal Muktadir, Fabrication of a low cost microcontroller based on spray pyrolysis system for thin film deposition, *3rd international conference on electrical engineering and information communication technology*, 22-24-sept, 2016
12. B W Mwakikunga, Progress in Ultrasonic Spray Pyrolysis for Condensed Matter Sciences Developed From Ultrasonic Nebulization Theories since Michael Faraday, *Crit. Rev. Solid State Mater. Sci.* 39, 46–80, 2014
13. A Ashour, M A Kaid, N Z El-Sayed, A A Ibrahim, Physical properties of ZnO thin films deposited by spray pyrolysis technique, *Applied Surface Science*, 252 (22), 7844-7848, 2006

Theoretical Analysis for Separation of Coagulant Proteins from *Moringa Oleifera* using Nano Structured Alumina

G Vijaya Kumar[1]*, Pushpa Agrawal[1], Thippa Reddy[1], Trilokchandran B[1]
[1]Department of Biotechnology, RV College of Engineering®, Bengaluru, India

Abstract

Coagulant protein was separated from extract of *Moringa oleifera* seeds using nano alumina as a bio-adsorbent material by conducting batch and continuous adsorption based on the Isoelectric Point (pI) of nano alumina and *Moringa oleifera*. Characterization of alumina was carried out by SEM and XRD. Adsorption of coagulant protein was observed experimentally by batch adsorption at different pH of adsorbate medium and adsorbent concentration. The results obtained followed the Freundlich adsorption isotherm model. Continuous column test results were performed to determine the breakthrough curves, mass transfer coefficient and number of mass transfer units at different bed height. The overall results indicated that the nano alumina can be used has a adsorbent to separate coagulant proteins based on pI effectively.

Keywords: *nano alumina, fixed bed, coagulant proteins, SEM, XRD, Isoelectric point*

1.0 Introduction

In search of natural coagulants in waste water treatment in place of chemical coagulants is not new, because the natural coagulants originated from plants are not harmful and also results in biodegradable waste which can be easily disposed into the nature without any harmful effects. Knowledge of water treatment using natural coagulants was known to mankind is centuries old [1]. Most investigated plant for extract of natural coagulants is *Moringa oleifera* whose seeds were used for water treatment in the rural areas of Sudan [2] because, *Moringa* seed powder can decrease around 90% of the bacterial load from raw water samples. This coagulant present in the form of protein in the seeds of *Moringa oleifera* is water soluble cationic peptide [14] with Isoelectric Point (pI) above 10 and molecular mass 6.5 Kda [3].

Various protein purification methods have been used to isolate proteins from *Moringa oleifera* seeds depending upon the protein size, shape, charge, hydrophobicity, solubility and biological activity to get good quality products. In general, the initial step involves preparation of crude in salty or buffer solution [4]. Since from the crude, the protein can be separated by various methods. Usually the protein from seeds can be separated by ion exchange [5],

---

**Mail address: G. Vijay Kumar, Associate Professor, Dept. of Biotechnology,*
RV College of Engineering®, Bengaluru, India
E-mail: vijayakg@rvce.edu.in, Ph: 9886272998

gel filtration [6] and affinity chromatography techniques, in all these techniques ion exchange (IEX) chromatography stands in the front for purification. In IEX the separation will be based on the adsorption of proteins to immobilized functional groups. These functional groups can be either positively or negatively charged. The most commonly used functional groups are DEAE and CM respectively. In the present purification studies, we have used nano alumina in behalf of functional groups and charged with positive based on the pH of the aqueous solution and pI of the nano alumina [7]. All the oxides can be characterized by their (pI) surface charge, if the pH of aqueous solution in contact with oxide material is below the pI of oxide material the oxide will acquire positive surface charge, if the pH of aqueous solution is above the IEP of oxide material the surface of material will acquire negative charge. The pI of silica, titanium, zirconia and alumina are near to 2, 5, 7 and 9. Alumina particles at neutral pH (around 6) will be meagerly positive charge in aqueous solutions, if the pH is lower than 6.0 the alumina powder is strongly positive charge. This result proposes that alumina materials will undergo DE- flocculation in basic and acidic medium.

In this context, nano alumina can be employed as a bio adsorbent material to separate coagulant proteins from *Moringa oleifera* seeds. The experimental parameters such as, adsorbent material, adsorbent concentration and pH for adsorption using batch adsorption studies were optimized initially, for the optimized batch adsorption studies Freundlich adsorption mathematical model [8] was used to validate the results.

2.0 Experimental Details

2.1 Materials and methods

Nano alumina used as adsorbent, was synthesized by spray pyrolysis method using a precursor. *Moringa oleifera* procured from local market in Bengaluru, was dried in oven, de shelled and powdered and used for experimentation.

The synthesized alumina powder was heat treated at 600^0C for a period of two hours to remove the moisture and other trapped gases etc., and was characterized using XRD and SEM respectively.

2.2 Crude protein extraction

The crude protein was extracted according to Ghebremichael et al. [12], dried *Moringa oleifera* seeds were De-shelled and the core obtained was crushed using a crusher. Oil obtained during crushing was removed by adding the 90% of acetone to the crushed material and centrifuged for 30 min at 10000 rpm at 10^0 C. The solids obtained was dried at 26^0C, after drying the solids were suspended in 5% (w/v) acetate buffer of ammonia (10 mM, pH 7.0) and then vacuum filtered, the filtrate attained was named as crude extract.

2.3 Theoretical Analysis

To study the adsorption behavior and effective adsorption, theoretical analysis is carried out for experimental values obtained from batch adsorption and continuous adsorption. The studies on the adsorption isotherms was to determine the effective rate of adsorption for the batch adsorption studies and mass transfer co-efficient is determined for continuous adsorption studies.

2.4 Batch adsorption

Nano alumina powder was taken in different conical flasks varying from 0.2 to 1.2 g separately, in each conical flask a 15 ml of crude is taken. Each conical flasks were incubated at 26^0C for 45 min with continuous shaking and filtered using vacuum filtration (250 mm Hg) unit. The filtrate obtained was analyzed for protein content using standard Lowry's method.

The results obtained were used to fit the Freundlich adsorption isotherm model for all the systems investigated.

Freundlich Isotherm

$\ln C^*$ vs $\ln v(C_0 – C^*)$

Where, C^* represents concentration of crude extract after adsorption,

C_0 initial concentration of crude extract,

v is the ratio of volume of crude extract to amount of adsorbent,

To determine Freundlich isotherms [8] $\ln C^*$ v/s $\ln v^*(C_0 – C^*)$ is graphically represented by considering the $\ln C^*$ in Y-axis and $\ln v^*(C_0 - C^*)$ in X-axis, the slope n and intercept k is obtained from the graph, where k and n are Freundlich adsorption parameters.

For the determination of mass transfer coefficient the method described by Vukojevic M [9] et al., is used based on the result from the breakthrough curve. The overall mass transfer coefficient, Ka, for continuous adsorption for the known bed height were evaluated using the following equation

$K_a = (NG_w / H)$ ------------------(1)

Where: G_w is the mass flux of solution, kg/min mm^2

K_a is the overall mass transfer coefficient, kg/min mm^3

N is the number of mass transfer units

H is the bed height, m

The Mass flux of solution in the packed column can be evaluated by the following relation:

$G_w = (Q\rho) / (A\epsilon)$ ------------------- (2)

Where Q is the flow rate of solution through the column, m^3/min

ρ is the density of the liquid solution passing through the column, kg/m^3

ϵ is the porosity of the bed

A is the area of the column, m^2

Number of transfer units (NTU) was determined using a graphical representation between ln C^*/C_0 vs 1+ ln C^*/C_0 which was explained by Vukojevic M [9] et al. The value of 1+ ln C^*/C_0 at 0.05 ln C^*/C_0 is evaluated (Fig 8) and used in the following equation to evaluate N

$1 + C^* / C_0 = N (T -1)$ ------------------(3)

Where T can be evaluated by knowing the break point and exhaust point in the breakthrough curve.

2.5 Column test

The column test was carried out at an ambient temperature in a glass column (Inner diameter ID=18 mm, length l = 100 mm). The nano alumina with known amount was randomly packed in the column for a bed depth of known arbitrary height. The tap density and the void fraction were found to be 74kg/m^3 and 0.467 respectively and were maintained constant. *Moringa Oleifera* crude of concentration 2.12 mg/ml at normal pH was constantly fed from top of the adsorption column at 60 ml/hr until exhaust point of the adsorption was reached. From the bottom of the column for every fraction of 5 min the effluent samples were collected and analyzed for protein concentration. The conditions maintained in the column for different experimental trials are given in Table 1.

Table 1 Column conditions for different trials

Experimental conditions	Run 1	Run 2
Porosity nano alumina	0.467	0.467
Density of nano alumina kg/m^3	74	74
Bed depth mm	15	25
Flow rate ml/hr	60.0	60.0
Dia of the column mm	18.0	18.0
Initial concentration of protein mg/ml	2.12	2.12

3.0 Results and Discussion

3.1 SEM

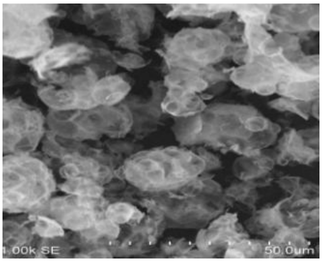

Fig 1 SEM of nano alumina powder

Fig 1 displays the nano-structured alumina particles with hollow, porous morphology, agglomerated with spherical in shape. The spherical shape indicates the salts are completely evaporated and nucleated to the perfect shape, this is in line with the, SEM images of the produced composites reported by Kim [11] which displays spherical, loosely aggregated particles which is due to the low evaporation the solid particles are nucleated.

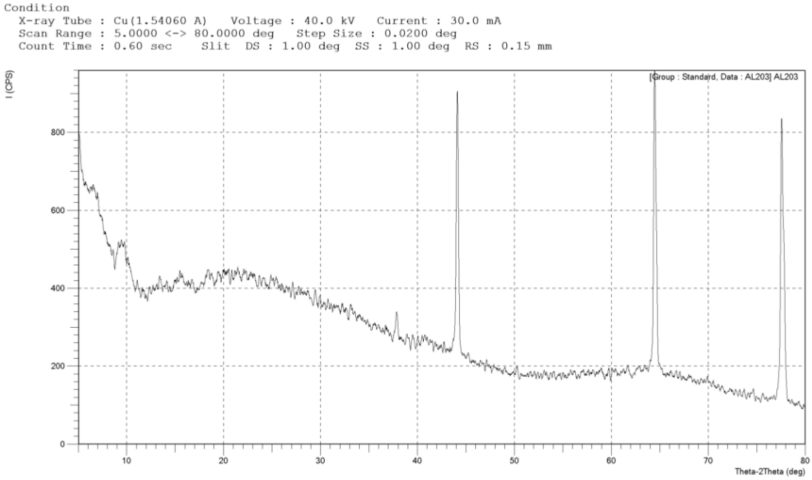

Fig 2 XRD (two theta) plot of nano alumina powder

3.2 XRD

The XRD image of nano alumina (Fig 2) displays 3 peaks at 44°, 64 ° and 77 °, which is as per ICDD (Standard ICDD 29-0063) this is in line with the Martin et al., [10] reported the XRD results for thermally treated nano alumina with well-defined peaks at 45°, 67° and 77.61° and XRD patterns reported by Shighehiro et al., [13] showed 2 peaks at 47° and 65°.

3.3 Study on Adsorption Isotherms

For the results of batch adsorption studies, Freundlich adsorption isotherm mathematical model were used. From the nature of the graph it is confirmed the cationic proteins were adsorbed on nano alumina with a slope of 1.23.

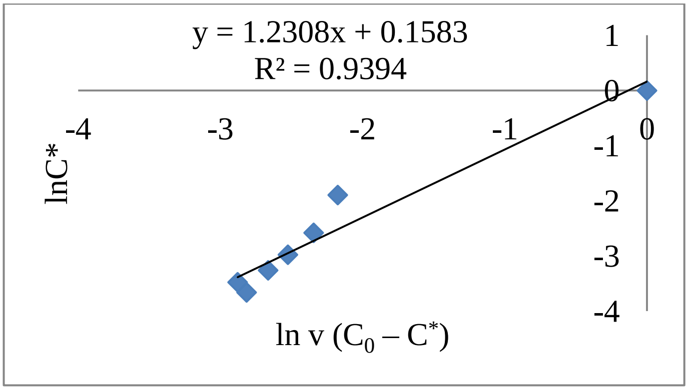

Fig 3 Freundlich isotherm model for adsorption of protein on nanostructured alumina

The Freundlich isotherm constant for alumina is 1.23 (Slope value), which indicates that the alumina is good adsorbents to adsorb the desired proteins.

3.4 Effect of adsorbent

Nano alumina powder were taken in different conical flasks varying from 0.02 to 0.12 g separately, in each conical flask a 15 ml of crude is taken. Each conical flasks were shaken well for 45 min at pH 7.0 and centrifuged for 25 min at 10,000 rpm, the supernatant obtained was subjected for total protein content at 660 nm.

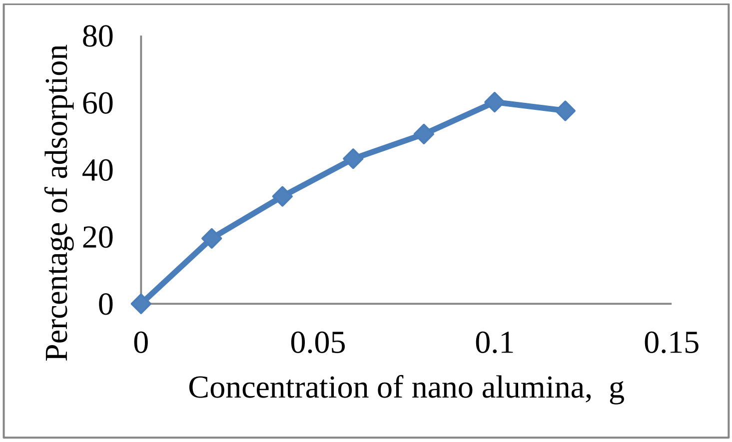

Fig 4 Effect of adsorbent concentration on adsorption of proteins

The graphical representation of effect of adsorbent (Fig 4) represents the increase in adsorption for increased in adsorbent. The adsorption was maximum (60%) when the concentration of the adsorbent was 0.1 g, still further increase in the adsorbent concentration the adsorption of protein was dropped to 56%. This may due to the binding the active site of the adsorbent.

3.5 Effect of solution pH

0.1 g of nano alumina was taken in each of the 4 conical flasks and equal amount of crude proteins were taken in each of the flasks. The pH in each of the conical flask was varied from 2 to 9 (2, 4, 6 and 9). The mixture was mixed well for 45 min and filtered the filtrate obtained was analyzed for adsorption of protein. The results is graphically represented in Fig 5.

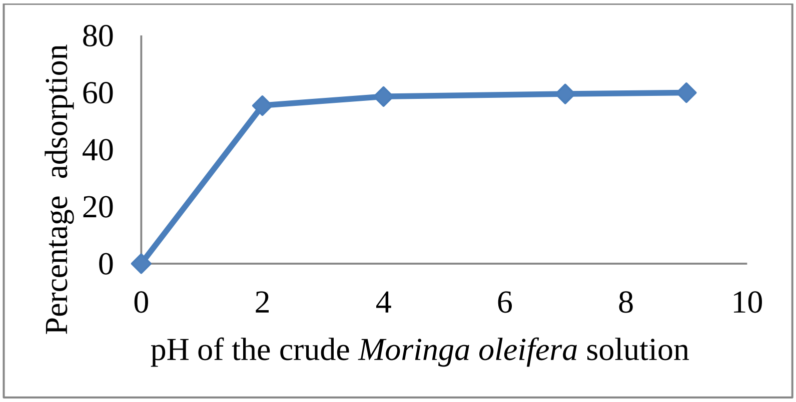

Fig 5 Effect of pH on adsorption

From the above Fig 5 the adsorption of protein was 56% at pH 4.0 and there was a nominal increase in adsorption from 56% - 59% of protein with increase of pH from 4.0 to 9.0 in case of alumina. This was due to the surface charge on nano alumina becomes positive charge (pI 9.0) at pH 7.0 and coagulant protein also gets positive charge and there was a adsorption of anionic charge proteins on nanostructured alumina. The coagulant protein fundamentally a cationic charge at pI 9.6 will not be attracted by the surface of the nano alumina, gets separated due to non-affinity toward nanostructured alumina.

3.6 Break through curves for 15 and 25 mm bed height

Graphical representation of C^*/C_0 V/s time obtained (Fig 6) from the results of continuous adsorption of M*oringa oleifera* proteins over the nano alumina particles at a rate of 60 ml /h for different bed heights, shows the similar pattern of S shaped curve with increase in bed height with increase in break thorough curve. The results of the graph is presented in Table 2.

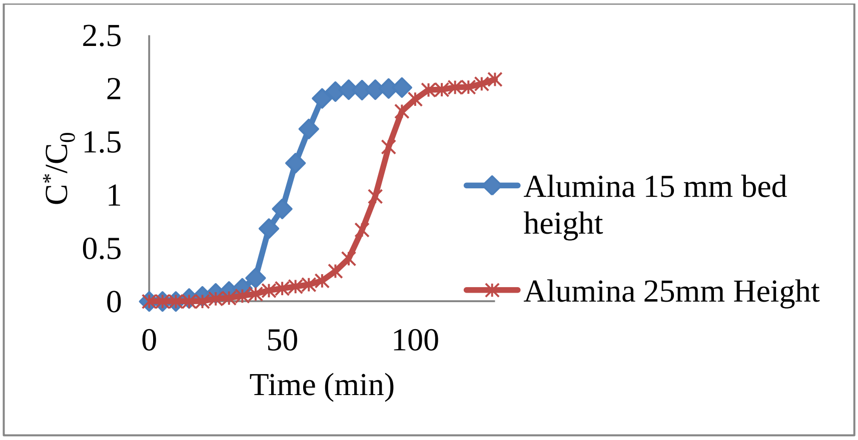

Fig 6: Break through curves for 15 and 25 mm bed height

Fig 6 indicates the break point (Value of X axis for the 0.05 value of Y axis, which refers to 95% of adsorption) for adsorption of protein on nano alumina is 43 min (15 mm Bed), 78 min (25 mm Bed height) and exhaust point (Value of X-axis when the curve in the graph becomes constant) is 65 min (15 mm Bed height), 105 min (25 Bed height), this was due to the rise in bed height and the contact time between nano alumina and crude protein, break time rises by 44% and exhaust time rises by 40%, which indicates rise in height rises percentage of adsorption.

3.7 Evaluation of Mass transfer coefficient through break through curves

Evaluation of mass transfer coefficient the graph of C^* / C_0 vs $1+\ln C^*/ C_0$ (Fig 7 & 8) is plotted, the value of X-axis is evaluated for the 0.05 value of Y-axis. The results obtained from the graphs is used to evaluate the mass transfer coefficient (Table 3)

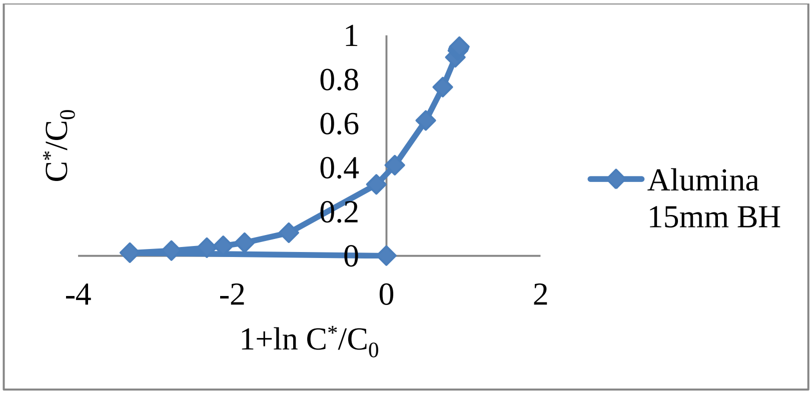

Fig 7 C^*/C_0 vs. $1+\ln C^*/C_0$ to determine the mass transfer coefficient for 15mm BH

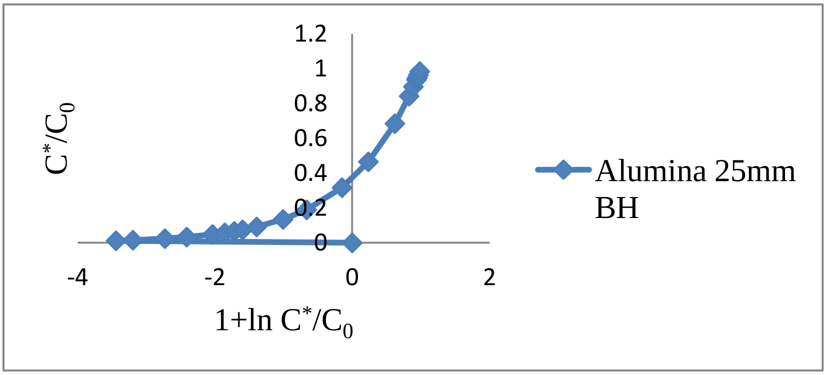

Fig 8 C^*/C_0 vs $1+\ln C^*/C_0$ to determine the mass transfer coefficient for 25 mm BH

Table 2.0: Results of break through curve and determination of T, from the graph Fig 6

Mate-rial	Bed height H meter	Break point T_B min	Exhaust point T_E min	$\tau = T_B/T_E$	Q m^3/min	Diameter of the column Meter	Area m^2	Porosity	Density of crude protein kg/m^3
Nano Alumina	0.015	43	65	0.661	$1x10^{-6}$	0.018	$2.5x10^{-4}$	0.466	970
	0.025	78	105	0.742	$1x10^{-6}$	0.018	$2.5x10^{-4}$	0.466	970

Table 3.0: Determination of Mass transfer coefficient from the graphs Fig 7 & 8

Material	Value of x-axis when the y-axis value = 0.05 (Fig 7 & 8)	NTU in adsorption column N	Mass transfer flux $G_W = (Q*\rho)/A*€$ kg/ m^2 min	Mass transfer coefficient $K_{La} = (N*G_W)/H$ kg/min m^3
Nano Alumina	-2.0	3.7	8.326	2053
	-1.8	6.9	8.326	2297

The results presented in Table 3, indicates the rise in mass transfer coefficient with rise in bed height of nano alumina. Mass transfer coefficient for nano alumina is 34 and 38 kg/s m^3 for 15 mm and 25 mm bed height. From the results the mass transfer coefficient rises with rise in bed height, this may be due to the NTU which rises the adsorption of proteins.

4.0 Conclusion

For adsorption process in which nano alumina, with low density, hollow morphology and spherical in shape can be used as an adsorbent material to separate the proteins. The slope value obtained (1.23) from the Freundlich equation indicates the adsorption process is feasible and the process can be scaled up for commercial purification of the proteins. The results of the continuous adsorption studies predicts the breakthrough curves were in good arrangement and the mass transfer coefficient were independent of bed depth and rises with rise in NTU.

References

1. Shilpa Tripathi, Vineet K Rathore, Jahnavi Gokhale and Parag Agrawal, Some study on *Moringa Oleifera* (Drum stick) seed as natural coagulants for treatment of distillery waste water, International Journal of Applied Engineering and Technology, 2(2), 24-30, 2012.
2. Jahn SAA, Hamid D, Studies on Natural Water Coagulant in Sudan with Special Reference to *Moringa oleifera* Seeds, Water S.A., 5, 90-97, 1979.
3. Gassenschmidt U, Janny KK, Tauscher B and Niebargell H, Isolation and characterization of floculating protein from *Moringa oleifera* lam, BBA Biochemica et Biophysica Acta 1234, 477-484, 1995.
4. Kennedy JF, Paiva PMG, Correia MTS, Cavalcanti MSM, Coelho LCBB, Lectins, versatile proteins of recognition: a review, Carbohydr Polym, 26, 219–30, 1995.
5. YanQ, JiangZ, Yang S, DengW, HanL, A novel homo-dimeric lectin from Astragalus mongholicus with antifungal activity, Arch Biochem Biophys, 442:72–81, 2005.
6. Rego EJL, Carvalho DD, Marangoni S, Oliveira B, Novello JC, Lectins from seeds of Crotalaria pallida (smooth rattlebox), Phytochemistry, 60, 441–446, 2002.
7. Xu Hong Wang and Yoshihiro Hirata, Electrical and rheological properties of colloidal alumina suspensions, Ceramic processing research, 1, 64 – 68, 2000.
8. Robert R Treybal, Mass Transfer operations, 3rd edition, Mc Graw Hill Publication, 2000.
9. N. Vukojeviæ Medvidoviæ, J. Periæ, M. Trgo, I. Nuiæ, and M. Ugrina, Design of Fixed Bed Column for Lead Removal on Natural Zeolite Based on Batch Studies, Chem. Bio-chem. Eng, 27 (1) 21–28, 2013.
10. Martin MI, Gomex LS, Milosevie O, Rnabanal ME, Nanostructured alumina particles synthesized by spray pyrolysis method: Microstructural and morphological analyses, Ceramic International, 36, 767-772, 2010.
11. Kim SH, Liu BYH, and Zachariah MR. Synthesis of Nanoporous Metal Oxide Particles by a New Inorganic Matrix Spray Pyrolysis Method. *Chem. Mater.*, 14, 2889-2899, 2002.

12. Ghebremichael KA, *Moringa* seed and pumice as alternative natural materials for drinking water treatment, KTH Land and Water Resource Engineering, ISBN 91-7283-906-6, 01-70, 2004.
13. Shigehiro Arita, Nobuyoshi Aoyagi, Kenji Ohshita, Yasuhiro Tsubota and Takashi Ogihara, Synthesis and characterization of spherical alumina nanoparticles by spray pyrolysis using radiofrequency plasma, Journal of ceramic society of japan, 125 (6), 539-542,2017.

Electrical Resistivity for Assessing Durability of Fiber Reinforced Concrete

Sonali Kumari[1], Tarun Chaudhary[1], Subhangi Pati[1], K. Shastry[2*] and Dhanush S[1]

[1]*Civil Engineering, RV College of Engineering®, Bengaluru*

[2]*Dept. of Physics, RV College of Engineering®, Bengaluru*

Abstract

Electrical resistivity in concrete is a key parameter that can be correlated to its durability. The aim of this research is to correlate the relationship between electrical resistivity with the strength and durability characteristics of concrete. The influence of parameters such as grade of concrete, water to cement (w/c) ratio and fiber dosage, at constant degree of saturation and temperature was investigated. Four-probe method was used to measure the resistivity of M40, M30 and M20 grades of concrete with 0.5%, 0.75% and 1% fiber content. It was observed that for a given fiber content, higher grades concrete showed smaller percentage decrease in electrical resistivity as compared to its corresponding lower grade. A decrease in resistivity by 37.5%, 42.5% and 48.8% was observed with the addition of 1% of steel fiber for M20, M30 and M40 grades of concrete respectively. Similar trends were observed for resistivity in 0.5% and 0.75% fiber content mixes. It was observed that mixes with higher resistivity possessed greater strength and durability.

Keywords: *Electrical Resistivity in concrete, Durability Characteristics, Steel Fiber, Four-probe method*

1.0 Introduction

One of the key factors in serviceability of a structure is quality control. Concrete being a heterogeneous material, it is harder to assess its durability characteristics and use it as a quality control variable [1]. However, research suggests that the durability of concrete can be expressed as a function of its microstructure properties like porosity and electrical resistivity [2]. These microstructure properties are closely associated with interconnected channels within the hydrated composite and can be linked to porosity and electrical resistivity parameters. Strong inverse correlation exists between electrical resistivity and characteristics like corrosion, crack width, etc [3]. Attempts have been made to develop quantifiable non-destructive testing methods based on electrical resistivity measurements utilising the various quality control variables and their correlation with resistivity [4]. Presence of pore connections in concrete can be attributed to the porosity, which in turn can be used as a

---

**Mail address: K. Shastry, Assistant Professor, Dept. of Physics, RV College of Engineering®, Bengaluru-59*

Email: karthikshastry@rvce.edu.in, Ph.: +91 8897920216

parameter to quantify its durability [5]. Electrical resistivity of concrete is defined as the ability of concrete to resist the flow of ions within the hydrated interconnections. Experimental studies suggest that concrete has a range of resistivity between 10-10^6 Ohm-m [6]. This suggests that electrical conductivity is caused due to the presence of interconnected channels in the concrete matrix. Thus, depending on the degree of saturation of these interconnected paths in the matrix, a range of corresponding resistive properties is exhibited.

Cement composition, its content, water cement ratio, temperature, admixtures, and additional cementitious materials in concrete are some factors that influence its electrical resistivity [7]. Electrical resistivity is also affected by the quality and composition of water used for mixing concrete and the age of the sample [8]. This measurement, in practice, is used as an indicator for degree of corrosion in the Reinforced Cement Concrete (RCC) structure. The greater the resistivity, lower the current passing between the cathodic and anodic areas of the reinforcing steel and thus lowering the extent of corrosion [9]. Of the two methods employed in measuring the resistivity in a concrete specimen; the use of two-probe technique in measurements is avoided in order to minimize the possibilities of error arising due to electrode polarization potentials [10]. Therefore, in the current study the Wenner probe method (Four-Probe Method) was used to measure the electrical resistivity of the specimens.

2.0 Methodology

2.1 Materials

Concrete samples of grade M20, M30, M40 were made using Ordinary Portland Cement (Grade 53) conforming to the specifications of IS 12269: 2013 as shown in Fig. 1. Coarse and fine aggregates conforming to IS 383: 2016 were used and were tested for water absorption and specific gravity. Hooked end steel fibers of length 35 mm, diameter 0.65 mm and an aspect ratio of 64 and a specific gravity of 7.75 were used as functional fillers. Ingredients for the concrete mix were proportioned as per the mix design as shown in Table 1 and subsequently cast into beams. The samples were tested for electrical response at 15 and 28 days.

Fig. 1. Beams left to dry after curing

Table 1. Concrete Mix Proportion Table

Sl. No.	**Mix**	**Water (kg/m^3)**	**Cement (kg/m^3)**	**CA (10 mm) (kg/m^3)**	**CA (20 mm) (kg/m^3)**	**FA (kg/m^3)**	**Admixture (kg/m^3)**
1	M20	200	333	437.52	291.68	1062.62	1.67
2	M30	200	400	423.78	282.52	1029.26	2
3	M40	200	500	403.18	268.79	1009.51	2.5

Note: Fiber dosage was taken as x% by weight of cementitious content. CA: Coarse Aggregate, FA: Fine Aggregate

2.2 Sample Geometry and Layout of Electrodes

Beams of dimensions 500 mm (length) X 100mm (width) X 100mm (depth) were used for experimentation in accordance with IS 10086-1982. The configuration of the electrodes has a significant effect on the electric field distribution in the concrete and on the electrical resistivity [11]. Electrodes were placed as shown in Fig. 2 (a:187.5mm, b: 10mm, 105mm, c:105mm). The location of electrodes is in the region of maximum bending moment and minimal shear force. Further, the electrodes are embedded deep into the concrete block for ensuring maximum integrity with the concrete.

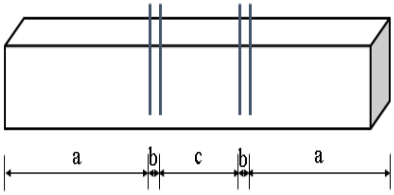

Fig. 2. Layout of electrodes used in experimentation (All dimensions are in mm a: 187.5mm, b: 10mm, c:105mm)

Fig. 3. Experimental set-up for measurement of electrical resistivity

2.3 Experimental Set-up

The Wenner probe method (Four-Probe Method) was used for the current setup to minimize the contact resistivity and concrete and polarization potentials between the electrodes as shown in Fig. 3. [12]. When DC current is applied during the measurement of voltage, the movement and concentration of the ions in the concrete matrix results in polarization [13], which causes fluctuations in the measured voltage values. The measurements reported in this paper were carried out at constant temperature and stable testing conditions. Various dosages of steel fibers (0.5%, 0.75%, 1%) were used within the mix design to establish a relation between functional filler dosage and electrical resistivity. The voltage readings were taken at the dry condition of the concrete specimen to mitigate the effect of water content within the sample during 15 and 28 days testing. In order to mitigate the effects of temperature variation in the concrete matrix [14], the experiment was performed in a uniform temperature environment.

3.0 Preliminary Results and Discussion

3.1 Voltage-Current (V-I) Characteristics of Samples

As the initial current is passed through the concrete specimen, the ensuing polarization mechanism causes fluctuations in the voltage measurements due to its sensitivity to temperature and degree of saturation. In order to maintain near equal levels of hydration and uniform temperature, all the samples were tested exactly after 28 days of curing under similar conditions. The V-I characteristics thus obtained for various grades of concrete with varying fiber dosages are shown below. It can be seen from Fig. 4 - 7 that the slope of the V-I curve increases with grade of the concrete. This can be attributed to the reduction in water to cement ratio of the concrete mix, which narrows the interfacial transition zone of the matrix and thus reducing the porosity.

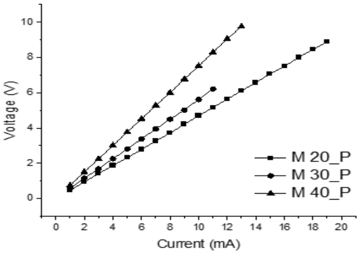

Fig. 4. V-I Characteristics for Control Mix i.e., M20, M30 and M40 grades of concrete

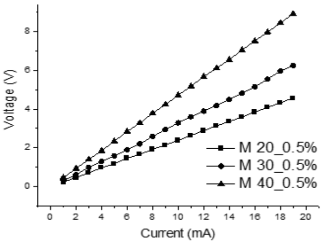

Fig. 5. V-I Characteristics for M20, M30 and M40 grades of concrete with 0.5% fiber dosage

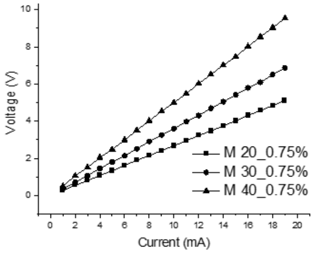

Fig. 6. V-I Characteristics for M20, M30 and M40 grades of concrete with 0.75% fiber dosage

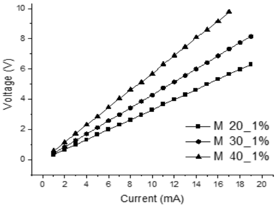

Fig. 7. V-I Characteristics for M20, M30 and M40 grades of concrete with 1% fiber dosage

3.2 Resistivity vs Fiber content

The V-I characteristic of concrete generally follows an Ohmic trend. By addition of 0.5% of steel fiber, a decrease of 37.5%, 42.5% and 48.8% in electrical resistivity was observed for M20, M30 and M40 grades of concrete respectively. A similar trend is followed by the specimens with 0.75% and 1% fiber dosage, as shown in Table 2. The variations obtained in the resistivity values with respect to the varying grades of concrete and fiber contents is due to the dispersion and orientation of fiber in the matrix. In order to observe the effect of water to cement ratio on electrical resistivity, various grades of concrete were tested with water to cement ratio 0.6, 0.5 and 0.4. It was observed that as the water to cement ratio increases, the resistivity decreases as shown in Table 2. Fig. 8 shows the direct relationship between the electrical resistivity of concrete and its characteristic compressive strength. From Fig. 9, it can be seen that the change in electrical resistivity directly varies with the grade of concrete. This direct relationship between electrical resistivity, characteristic compressive strength is due to the reduction in the water to cement ratio of the concrete mix, which further narrows the interfacial transition zones of the matrix; thereby reducing its porosity leading to increase in strength.

Table 2. Change in electrical resistivity with varying fiber dosage for various grades of concrete

Fiber Dosage	**Change in Electrical Resistivity for different grades of concrete**		
	M20	**M30**	**M40**
0.5	23.70	23.90	29.30
0.75	33.22	36.06	42.80
1	37.50	42.50	48.80

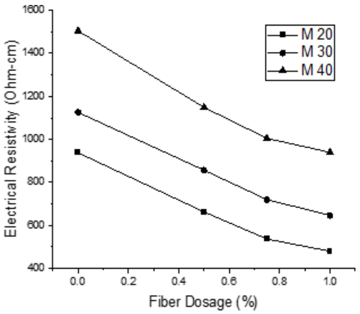

Fig. 8. Resistivity v/s fiber dosage for various grades of concrete

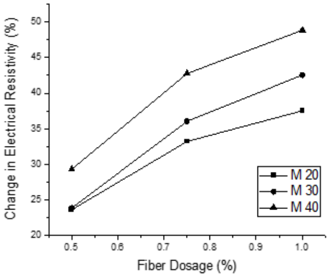

Fig. 9. Change in electrical resistivity v/s fiber dosage for various grades of concrete

3.3 Effect of Age of Concrete on Electrical Properties

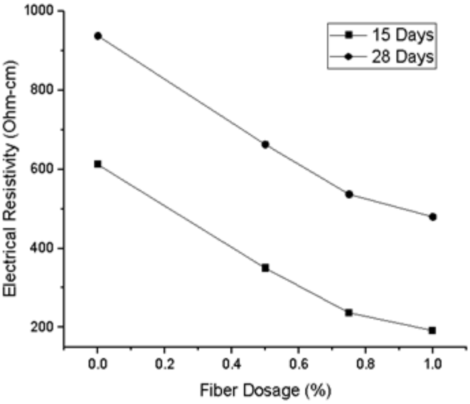

Fig. 10. Resistivity vs. fiber dosage of M20 grade of concrete after 15 and 28 days of curing respectively

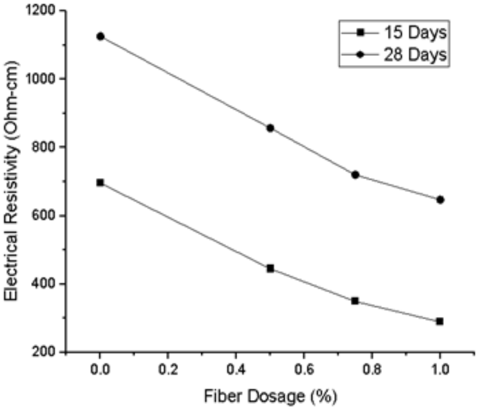

Fig. 11. Resistivity vs. fiber dosage of M30 grade of concrete after 15 and 28 days of curing respectively

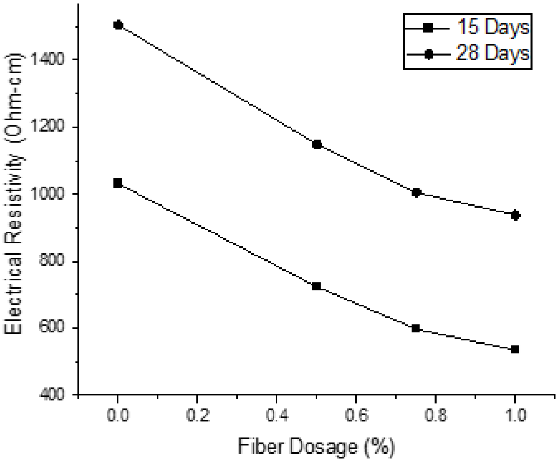

Fig. 12. Resistivity vs. fiber dosage of M40 grade of concrete after 15 and 28 days of curing respectively

Another interesting observation is the increase in electrical resistivity with the age of the concrete sample as shown in Fig. 10-12. An average increase of 52.59%, 48.28% and 38.63% was observed in the electrical resistivity for M20, M30, and M40 grade respectively at 28 days as compared to measurements at 15 days. This variation is because of the increase in the gel space ratio with the age of concrete; the volume occupied by the hydration product also increases. This increase in volume restricts the flow of electrons or ions through interconnections in the composite and inhibits electrical conductivity. After 28 days of curing, 99% hydration reaction is achieved and no further significant increase in electrical resistivity is observed.

4.0 Conclusions

The increase in the volume of functional fillers causes a drop in the electrical resistivity values in the concrete matrix. By addition of 0.5%, 0.75% and 1% of steel fiber, a decrease of 23.7%, 33.22% and 37.5% in electrical resistivity was observed for M20, 23.9%. 36.06%, 42.5% for M30 and 29.3%, 42.8%, 48.8% for M40 grades of concrete respectively. Owing to the direct correlation between the presence of hydration products with the age of the concrete, it was also observed that there is an increase in the electrical resistivity with respect to the age of the specimen. At 28 days, an average increase of 52.59%, 48.28% and 38.63% was observed in the electrical resistivity for M20, M30, and M40 grade respectively, at different fiber dosage, compared to 15 days measurements. The trends observed in this paper indicate the presence of hydration products in the concrete specimen leading to larger gel space ratios, which ultimately increases electrical resistivity.

Future work would involve a flexure test on the specimen during conduction of electricity in a load-controlled environment to establish electrical resistivity as a viable structural health monitoring parameter. Attempts will be made to correlate electrical resistivity measurements with strain developed in the specimen.

References

1. O Sengul, Use of electrical resistivity as an indicator for durability, *Construction and Building Materials,* 73, 434–441, 2014
2. W Morris, A Vico, M Vazquez, S R De Sanchez, Corrosion of reinforcing steel evaluated by means of concrete resistivity measurements, *Corrosion Science*, 44, 81–99, 2002
3. K. Hornbostel, C. K. Larsen, and M. R. Geiker, “Relationship between concrete resistivity and corrosion rate—a literature review,” Cement and Concrete Composites, 39, 60–72, 2013
4. C Andrade, C Alonso, Corrosion rate monitoring in the laboratory and on-site, *Construction and Building Materials,* 10(5), 315–328, 1996
5. A Q Nguyen, G Klysz, F Deby, J P Balayssac, Evaluation of water content gradient using a new configuration of linear array four-point probe for electrical resistivity measurement, *Cement and Concrete Composites*, 83, 308-322, 2017
6. D A Whitting, M A Nagi, Electrical Resistivity of Concrete, *Portland Cement Association*, Skokie, Ill, USA, 2003
7. A Ramezanianpour, A Pilvar, M Mahdikhani, F Moodi, Practical evaluation of relationship between concrete resistivity, water penetration, rapid chloride penetration and compressive strength, *Construction and Building Materials*, 25, 2472–2479, 2011
8. J Hoheneder, I Flores-Vivian, Z Lin, P Zilberman, K Sobolev, The performance of stress-sensing smart fiber reinforced composites in moist and sodium chloride environments, *Composites Part B: Engineering*, 73, 89–95, 2015

9. B B Hope, A K Ip, D G Manning, Corrosion and electrical impedance in concrete, *Cement and Concrete Research*, 15(3), 525–534, 1985
10. Maria S Konsta Gdoutos, Chrysoula A Aza, Self-sensing carbon nanotube (CNT) and nanofiber (CNF) cementitious composites for real time damage assessment in smart structures, *Cement & Concrete Composites*, 53, 162–169, 2014
11. C T Chen, J J Chang, W C Yeih, The effects of specimen parameters on the resistivity of concrete, *Construction and Building Materials*, 71, 35–43, 2014
12. S Wen, D D L Chung, Electrical-resistivity-based damage self-sensing in carbon fiber reinforced cement, *Carbon*, 45(4), 710–716, 2007
13. H Layssi, P Ghods, A R Alizadeh, M Salehi, Electrical resistivity of concrete, *Concrete International*, 41–46, 2015
14. R B Polder, Test methods for onsite measurement of resistivity of concrete - a RILEM TC-154 technical recommendation, *Construction and Building Materials*, 15(2-3), 125–131, 2014
15. IS 12269 (2013) Ordinary Portland cement, 53 grade-specification (second revision). Bureau of Indian Standards (BIS), New Delhi, India
16. IS 383: 2016 Indian Standard Coarse and Fine Aggregates for Concrete (Third Revision). Bureau of Indian Standards (BIS), New Delhi, India
17. IS 10086: 1982 Specification for moulds for use in tests of cement and concrete. Bureau of Indian Standards (BIS), New Delhi, India

Efficient Aerodynamic System of Rear and Front Wings for an FSAE Car

A Siddharth Reddy[1], Atheeq Ur Rehman[1], Sathvik Shetty[1],
Shashank Vivek, Gajanan[1*]
[1]Department of Mechanical Engineering, RV College of Engineering®,
Bengaluru

Abstract

In the early 1980s, the motor sport industry came up with a new way of enhancing the performance without compromising on the efficiency through the concept of aerodynamics - generating very high down force thereby increasing traction, with no reduction in efficiency. Although motor sport industries are engaged in research on automotive aerodynamics, open literature on the same is limited. This research presents design and development of front and rear wings for an existing FSAE prototype which can generate a down force of 25 to 30 kgf i.e. 1/8 of the weight of the existing prototype at an average speed of 14 m/s increasing the cornering efficiency of the car. Based on motorsport racing aerodynamic requirements and constraints, a high lift to drag ratio aerofoil S1223 was selected. Simulations were carried out in ANSYS Fluent on aerofoil wings designed using SOLIDWORKS. At Reynolds number 1.84 x 10^5, a total down force of 34.8 kgf and a total drag force of 8.317 kgf was generated using simulation.

Keywords: *Aerofoil - S1223, Multi-element wing, CFD analysis, FSAE prototype, Downforce, Drag-coefficient*

1.0 Introduction

Over the past few decades, motorsport racing has evolved rapidly due to the intense competition amongst motorsport racing companies. Key design directions for the cars include reduction of weight, increase in engine power within the competition restrictions, and enhancing cornering performance by incorporating aerodynamic surfaces [1]. The main purpose for using aerodynamic devices in cars is to increase the down force experienced by the car to ensure greater traction between the tyres and the ground especially during cornering so that the car can approach the corner at greater speed. This needs to be achieved while ensuring that the drag contributed by these devices is at its minimum to mitigate the negative effects of engine losses in overcoming drag. There are different types of aerodynamic attachments such as wings (both front and rear), diffusers, Gurney flaps, end plates and active aerodynamic devices like spoilers, active rear wing and active grille shutter [2].

**Mail address: Gajanan, Assistant Professor, Dept. of Mechanical Engg.,*
RV College of Engineering®, Bengaluru – 59
E-mail: gajanan@rvce.edu.in, Ph: 8867550078

Wings used in motorsport racing are synonymous with the ones used in airplanes, with the major difference being the wings used in motorsports use inverted airfoils. One of the key aspects of a motorsports wing is that it operates in high ground effect. Peters et al [3] carried out wind tunnel studies on NACA0012 and DHMTU airfoil in ground effect and reported that that L/D ratio is superior at low angles of attack. Kaviem and Chelven [4] carried out an experimental study on NACA4412 airfoil in ground effect and reported that the performance is superior for angles of attack 4^0 to 8^0.

Wordley and Sanders [5] based on the work on aerodynamic package of an FSAE race car presented the down force calculations along with the understanding of balancing of the aerodynamic forces provided by the front and rear wings. Dalhberg [6] introduced the concept of inverse airfoil design for FSAE car. Zhang and Zerihan [7] presented comprehensive study of double element wing and different configurations of the wings to provide high down force. Review of literature indicated that aerofoil design, manufacturing processes and simulation parameters are not comprehensively reported. The present work was focussed on design and development of front and rear wing for an existing FSAE prototype car.

2.0 Detail Design with Computations

Initially, design of an airfoil that should cater to the motorsport aerodynamic requirements was carried out. During the design phase, multiple airfoil designs were considered and the best suited was selected after considering the characteristics and simulations were carried out for the desired result. Final wing configuration on the prototype with respect to rule constraints and number of wing elements was designed. After finalising the airofoil configuration, the wing configuration which included placement, angle of attack and chord length was fixed based on simulation. This phase included structural designing of the mounting and attachment points of the wings to the prototype’s chassis.

2.1 Geometry

Direct method of designing is a process in which airfoil shape is selected from a set of airfoil library for motorsport application which involves low Reynolds number high lift wings. Coefficient of lift to drag vs. angle of attack and coefficient of lift with angle of attack was compared for different airfoils. After comparison, S1223 was selected as the desired airfoil. The selected airfoil (Fig. 1) is a high lift airfoil and has the highest lift to drag ratio at low Reynolds number.

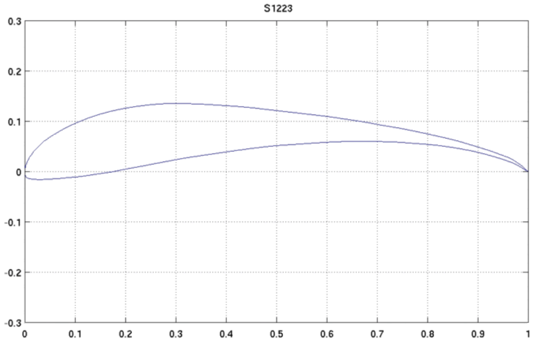

Fig. 1. S1223 Airfoil Geometry (scale: one unit is 0.1 unit length)

The operating velocity was chosen as 14 m/s which is the target speed of an FSAE prototype for entering a corner or a turn with the aerodynamic wings without losing traction at the wheels.

Calculation of Reynold's number:

$$Re = \frac{\rho V L}{\mu} \ldots\ldots\ldots\ldots\ldots\ldots\ldots\ldots (1)$$

The fluid flowing is air

μ= Dynamic viscosity = 18.6 x 10^{-6} Pa s

ρ= Density of fluid = 1.225 kg/m^3

V= velocity = 14 m/s

L= Chord length of wing = 0.2 m

$$Re = \frac{1.225 * 14 * 0.2}{18.6 * 10^{-6}} = 184408$$

The Reynolds number is within the limit of motorsport application and the chosen airfoil is suited for this.

For the overall wing assembly, the total downforce of 30kgf was kept as reference. S1223 airfoil of various chord lengths and various angle of attacks were used depending on the position of the elements of assembly were used to make the front wing and the rear wing.

For front wing, 3 segments with maximum of 2 elements were made to accommodate the wings as per FSAE rule book and rear wing was a 3-element assembly with the width complying the FSAE rulebook was designed. Fig. 2.a and 2.b shows the drawing of front and rear wing. Fig. 3 and 4 represents the Cad drawings of front and rear wing assembly respectively.

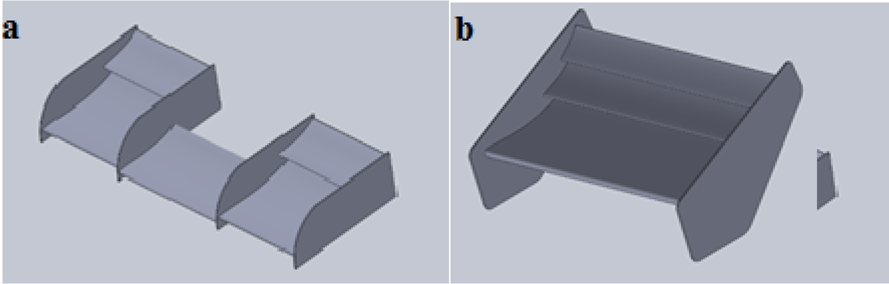

Fig. 2 a). Front Wing Assembly and **b).** Rear Wing Assembly

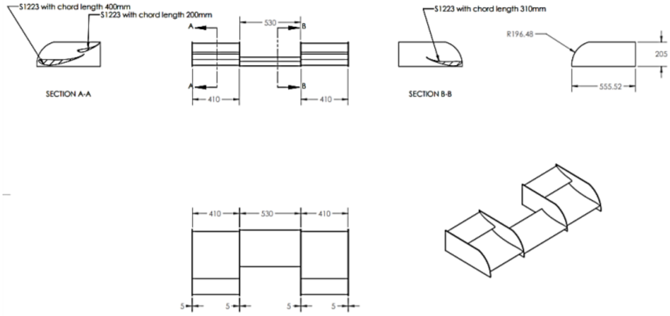

Fig. 3. Drawing of front wing

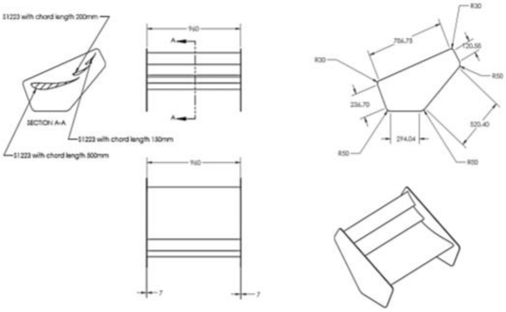

Fig. 4. Drawing of rear wing

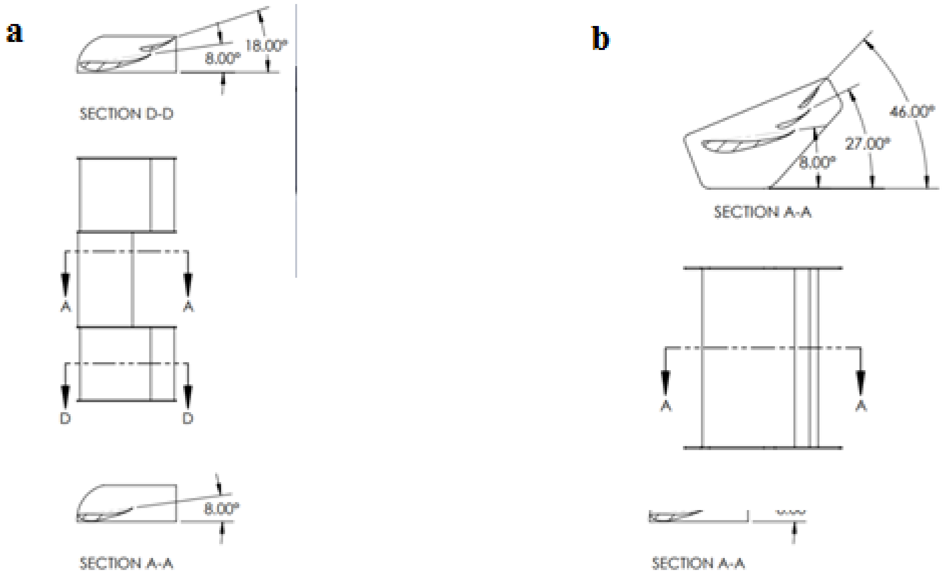

Fig. 5 a). Front wing Angle of Attack and **b).** Rear wing Angle of attack

Fig. 5.a and 5.b shows the angle of attacks for the two elements of front wing and three elements of the rear wing.

2.2 Meshing

Fig 6.a and Fig 6.b shows the mesh for the front wing and rear wing elements. Meshing was carried out in ANSYS Fluent meshing. For the mesh generation, a fine mesh setting was chosen. Further, inflation layer was added in order to capture boundary layer effects. Ten inflation layers were added by choosing a y+ factor of 1. The aspect ratio achieved for the front wing was 58.9 and that of the rear wing was 62.7 with a maximum skewness ratio of 0.958 for front wing and 0.907 for rear wing. These are within the limit of good mesh requirements of ANSYS Fluent. Table 1 shows the various meshing parameters and their corresponding values.

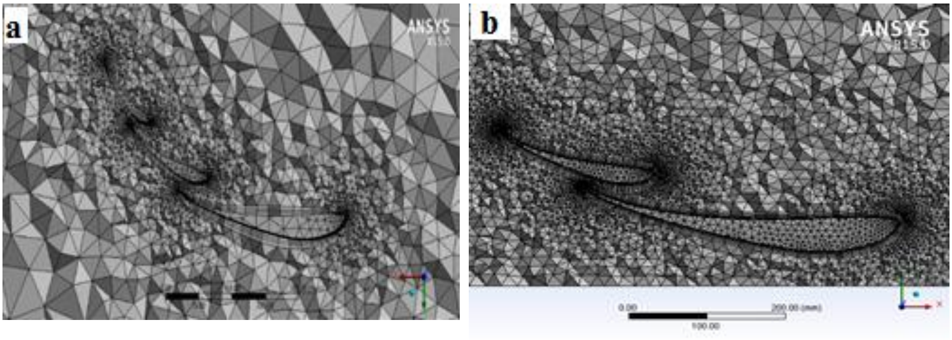

Fig. 6 a). Rear Wing Mesh and **b).** Front Wing Mesh

Table 1. Meshing parameters

Parameter	**Value/Condition**
Mesh sizing	Fine mesh
Y+	1
Number of Inflation Layers	10
Aspect Ratio – Front Wing	58.9
Aspect Ratio – Rear Wing	62.7
Skewness ratio – Front wing	0.958
Skewness ratio – Rear wing	0.907

2.3 Mesh independence test

The mesh independence test was performed with three different mesh sizes. The results are shown in Table 2 and table 3. The downforce and drag were considered as the variables which was used to determine if the mesh had converged. It is seen that the quantities vary considerably when comparing the coarse with medium mesh. However, there is no significant variation between the medium and fine meshes. Hence, the mesh with 5.2 million elements in the front wing and 6.2 million elements in the rear wing was considered for the study, as that was significantly faster to compute.

Table 2. Mesh independence study

Mesh elements			**Downforce (N)**		**Drag (N)**	
Front wing	Rear wing	Mesh type	Front wing	Rear wing	Front wing	Rear wing
3654889	4825974	Coarse mesh	155.2	169.4	25.9	42.5
5255694	6212394	Medium mesh	163.69	177.71	28.2	49.7
7845958	8745934	Fine mesh	163.91	177.96	28.5	49.9

Table 3. Percentage variation with mesh size

Mesh	Percentage variation			
	Downforce		Drag	
	Front wing	Rear wing	Front wing	Rear wing
Coarse and medium mesh	5.5%	4.9%	7.8%	14.4%
Medium and fine mesh	0.13%	0.14%	1.05%	0.4%

2.4 Analysis

The analysis was carried out on ANSYS Fluent. A steady state flow simulation was done as the car is not in acceleration condition and is considered as cruising condition. All the states of the dynamic system have reached the equilibrium levels. This means that the steady state values are the values that will be maintained as its after the time passed is tending to infinity. Table 4 depicts various analysis parameters chosen in Fluent.

For analysis, initially an enclosure was created around the wing assembly to simulate the surrounding environment.

Table 4. Analysis Parameters

Parameter	Value/condition
Viscous Model	K-Omega-SST
Solution method	COUPLED scheme
Initialization method	Hybrid initialization
Inlet Velocity	14 m/sec
Outlet Pressure	Zero Gauge Pressure
Condition for walls	No-slip and smooth

During analysis a velocity inlet, pressure outlet was chosen as those conditions are stable and are solvable. A velocity of 14m/s is chosen as that is a general cornering speed, and a zero-gauge pressure is chosen at the outlet. Further, a moving ground was chosen in order to capture ground effect for the front wing.

A viscous k-omega SST model is used for the simulation with curvature correction and production limiter as it captures the flow regime close to the wall as well as far away from it with the most accuracy. The SST model uses a mixing function value to automatically switch between k - ω (k-omega) and k - ε (k-epsilon) when close to or far away from a wall, respectively. The use of k - ω near the wall, where there would be boundary layer formation, makes the model directly usable all the way down to the wall, including the viscous sublayer. Hence, the SST model can be used as a Low-Reynolds turbulence model as well. Switching to k - ε away from the wall avoids the common problem associated with k - ω, that is the high sensitivity of the model in free-stream regions to inlet free-stream turbulence properties. The below equations model the turbulence of flow according SST theory: Equation 1 takes care of the kinetic energy k of the fluid and the equation 2 gives rate of dissipation. Also, COUPLED scheme solution method was chosen as it is suitable for our requirement. A hybrid initialization was chosen as the solution initialization methods. The simulations were run until a residue value of 10^{-6} for mass and momentum.

$$\frac{\partial(\rho k)}{\partial t}+\frac{\partial(\rho u_j k)}{\partial x_j}=P-\beta^{*}\rho\omega k+\frac{\partial}{\partial x_j}\left[(\mu+\sigma_k\mu_t)\frac{\partial k}{\partial x_j}\right] \quad \text{.........} \quad (2)$$

$$\frac{\partial(\rho\omega)}{\partial t}+\frac{\partial(\rho u_j\omega)}{\partial x_j}=\frac{\gamma}{v_t}P-\beta\rho\omega^{2}+\frac{\partial}{\partial x_j}\left[(\mu+\sigma_\omega\mu_t)\frac{\partial\omega}{\partial x_j}\right]+2(1-F_1)\frac{\rho\sigma_{\omega2}}{\omega}\frac{\partial k}{\partial x_j}\frac{\partial\omega}{\partial x_j} \quad \text{....} \ (3)$$

Fig. 7 a and 7 b represents the static pressure and velocity contour around the rear wing. As it can be seen, the upper surface is at a higher pressure in comparison with the bottom surface, this pressure difference creates the down force required for increasing the traction

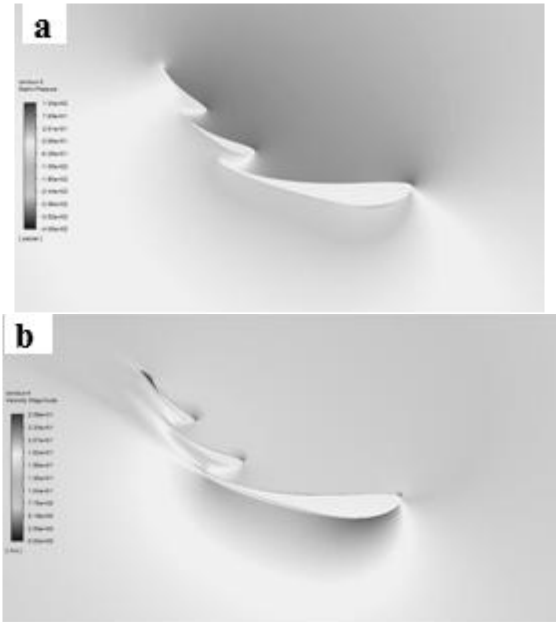

Fig. 7 a). Rear wing pressure contour and **b).** Rear wing velocity contour

3.0 Results

During the design phase, different aerofoils where considered initially with varying angle of attack and varying chord in order to achieve the desired downforce. Table 5 depicts the design methodology which is a highly iterative procedure. Multiple iterations were carried out to get to the final result. The simulations were carried out on ANSYS Fluent.

Table 5. Results of multiple iterations during design phase

Wing Elements		**Angle of attack (□, deg)**		**Chord Length (mm)**		**Downforce and Drag (N)**	
Front Wing	**Rear Wing**	**Front Wing**	**Rear Wing**	**Front Wing**	**Rear Wing mm**	**Front Wing**	**Rear Wing**
NACA2415	FX74	5.5,7.5	8, 27,38	400, 250	400,250,200	108.4, 18.3	149.2,25.6
NACA2415	E423	5.5, 9	8, 27,38	450, 250	400,250,200	113.2,20.3	140.5,36.5
E423	E423	9,15	8,30,45	400,250	300,250,150	119.2,21.6	143.2,41.3
E423	E423	9, 15	8,30,39	400,275	350,250,150	121.2, 26.3	149.2,39.5
S1223	S1223	8, 15,	8, 28,43	400, 250	350,200,150	125.6, 35.6	147.3,47.3
S1223	S1223	8, 14,8	8, 30,45	400,250,310	350,250,150	123.5, 36.7	167.5,46.2
S1223	S1223	9, 15,8	9, 25,40	400,250,250	400,250,200	134.7, 32.4	160.4,43.5
S1223	S1223	8, 15,8	8, 27,40	310,200,200	400,250,150	141.5, 31.7	165.9,45.6
S1223	S1223	8, 18,8	8, 28,46	400,200,310	500,200,150	163.69,29.8	177.7,49.7

3.1. Front wing

Compared to the rear wing, the front wing is very close to the ground, which induces ground effect. This is caused primarily by the ground interrupting the wingtip vortices and downwash behind the wing. The simulations were run till the residual values reaches around 10^{-6}. Table 6 represents the report of drag force and down force for front wing obtained from ANSYS Fluent. It can be seen that a down force of 163.69 N and a drag of 29.84 N was developed on front wing

Table 6. Result report of down force and drag force from ANSYS Fluent

Zone	**Down Force (N)**	**Drag Force (N)**
Wall-enclosure	163.69685	29.835473
Net	163.69685	29.835473

Front wing was simulated first till the desired result is obtained and later moment balancing is performed to obtain the desired rear wing result. This is because, front wing design is heavily constrained by the rulebook and the number of wing elements that can be accommodated. And there are many ways in which the downforce from rear wing can be changed with greater ease as there is more space and scope to make modifications on the rear wing.

The downforce from the front wing is 163.69N. Hence, by performing moment balancing between front and rear wing, the approximate downforce expected for the rear wing can be obtained. The moment balance was done by the following method as described below. Figure 8 shows the side view of the prototype with dimensions used for calculating the down force of rear wing.

1. The front edge of the front wing is at a distance 700mm from leading edge of the front wheel and COG is assumed to be in the middle, i.e. 350mm from leading edge of front tire.
2. The rear edge of the rear wing is at a distance 250mm from trailing edge of the rear wheel and COG is assumed to be in the middle, i.e. 125mm from leading edge of front tire.
3. Radius of tire is 225mm
4. COG of the whole prototype is at the middle of the wheelbase

The moment is balanced about the CoG as the force provided by the wings shouldn't affect the suspension characteristics of the vehicle as the changes in suspension characteristics may cause instabilty in vehicle performance.

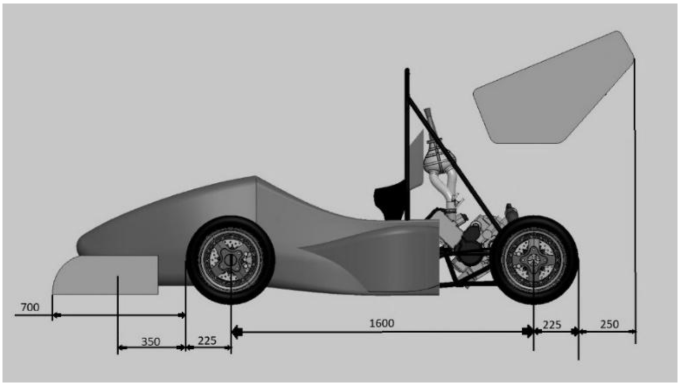

Fig. 8. Side view of the prototype along with its dimensions

Upon balancing the moments about the COG of the prototype, ($F_D$is assumed to be the downforce expected by the rear wing)

$$\left(\frac{700}{2}+255+\frac{1600}{2}\right)(163.69)=\left(\frac{1600}{2}+255+\frac{250}{2}\right)(F_D)$$

$$F_D = 194.90\text{N}$$

3.2 Rear wing

After the moment balancing, multiple iterations are performed to get the desired result. It's easier to make changes to get various results by changing chord length, angle of attack and number of wings. As the rear wing is well above ground, ground effect doesn't play a major role in the same. Table 8 and 9 represents the report of drag force and down force for rear wing obtained from ANSYS Fluent. It can be seen that a down force of 177.73 N and a drag of 51.76 N was developed on rear wing.

Table 7. Result report of down force and drag force from ANSYS Fluent for rear wing

Zone	Down Force (N)	Drag Force (N)
Wall-enclosure	177.73235	51.76918
Net	177.73235	51.76918

Hence the total downforce from front and rear wing was found to be

Front wing downforce + Rear wing downforce = 163.69 + 177.73

Total downforce = 341.42N
= 34.8kgf

The total drag from front and rear wings was found to be

Front wing downforce + Rear wing downforce = 29.83 + 51.76

Total drag = 81.59N
= 8.317 kgf

4.0 Conclusion

Design and development of front and rear wing for an existing FSAE prototype car was carried out successfully. ANSYS Fluent simulations were carried out with different aerofoils and different configurations to achieve the desired down force of around 30 kgf without much increase in drag force at Reynolds number 1.84 x 10^5. S1223 front and rear wing element was successful in achieving a down force of 34.8 kgf with a drag force of 8.317kgf.

References

1. R G Dominy Aerodynamics of Grand Prix Cars, *Journal of Automobile Engineering*, 206(4). 267-274, 1992
2. S S Pakkam, High Downforce Aerodynamics for Motorsports, *Master's Thesis*, North Carolina State University, 2011
3. A J Peters, N Moore and P A Wilson - An investigation into wing in ground effect airfoil geometry, *Proceedings of the Symposium on Challenges in Dynamics, System Identification, Control and Handling Qualities for Land, Air and Sea Vehicles*, Paris, France, 11-20, 2002
4. H. Al- Kayiem and K Chelven, An Investigation on the Aerodynamic Characteristics of a 2-D Airfoil in Ground Collision, *Journal of Engineering Science and Technology,* 6 (3), 369-381, 2011

5. S Wordley, J Saunders, Aerodynamics for Formula SAE: Initial design and performance prediction, *Proceedings of the SAE World Congress and Exhibition, Detroit, U.S.A*, 8-20, 2006
6. H Dahlberg, Aerodynamic Development of Formula Student Race Car *Master's Thesis*, KTH Mechanics University, 2007
7. J Zerihan and X Zhang, Aerodynamics of a Single Element Wing in Ground Effect, *Journal of Aircraft*, 37 (6), 2000

Performance Analysis of Precast Concrete Wall Joints

Ravindra R[1*], Rekha B[1], Nagesh M[2]

[1]Department of Civil Engineering, RV College of Engineering®, Bengaluru - 560059

[2]Research Scholar, NITK, Suratkal - 575025

Abstract

The vulnerabilities of precast concrete structures take place at its connections under lateral loading conditions. Although numerical analysis methods are economically viable for the analysis of structures, there are limited research data available in modelling of precast joints and connections due to the usage of patented elements in precast industry. The motivation of this work is to reduce the existing gap of analytical modeling of precast linkages. In this work, parameter modeling and analysis of precast wall-to-wall interlocking linkage are carried out. Also, three modeling mechanisms for interlocking connections of vertical wall joints - integrated, one link and three link - using ETABS are evaluated. The novelty of study is the identification of an appropriate numerical analytical model to represent wall-to-wall interlocking linkages. It is observed that three link analytical model better suits as a best linkage system in large panel precast construction-system considering in-plane shear, in-plane bending moment, axial force and storey displacements parameters.

Keywords: *Precast walls, Precast large panel, Precast joints, Linking system, Dynamic Analysis*

1.0 Introduction

With the increased pace of population, there is a tremendous demand of rapid quality infrastructure like housing and other amenities. To cater this tremendous demand, industrialized building construction, i.e. precast construction technology is to be adopted [1]. The performance and stability of precast structure depends on the continuity of structural and non-structural elements and their connections [1-2]. The design techniques and approaches should consider the performance of structure under gravity and lateral loading conditions. It should ensure having proper transference of loads to the foundation from the super structures through their structural/ non-structural elements and component connections/joints. Stability and continuity of joints in structure is the vital constituent for the performance of precast structures [2]. Inflexible or plastic behavior at joints limits the load transfer and affects overall structural performance. [1]

In the present study, analysis and behavior of precast structure and joint are carried out by analytical evaluation. The experimental analysis is costlier, and data is not available in academia due to its confidentiality. Numerical methods

---

**Mail address: Ravindra R, Associate Professor, Department of Civil Engineering,*

RV College of Engineering®, Bengaluru-560059

Email: ravindrar@rvce.edu.in, Ph: +91 9448020175

are economically viable for the analysis of structures, but there are limited research data available in analytical modeling of precast joints and connections due to the usage of patented elements in precast industry. The existing mechanisms of wall-to-wall linkages are either by welding or interlocking. The best analytical model suited to these linkage mechanisms is one of the biggest challenges in precast industry. The novelty of this work is the identification of an appropriate analytical model for wall-to-wall linkages mechanism.

The precast concrete structures with load bearing wall panels studied by Bob van Gils [3] recommended as the best suited technology for multistoried residential and commercial buildings and advantageous compared to RCC frame structures. The work describes the practical and economical aspects of designing and constructing of large panel systems structures. The thematic literature survey was carried out on experimental study on precast structures and analytical modeling of precast panels/structures.

The experimental study on exterior and interior was carried out N Rossley et.al [4] to determine behaviour of loop bars connection and crack patterns under shear loading. It was concluded that the loops provided enough ductile resistance and inclined cracks observed near loops at ultimate loading points and recommended for medium rise precast building. The experimental study to evaluate the shear behaviour of vertical joint in precast wall panels was carried out by Aparup Biswal et.al [5]. It was evaluated that the strength and deformability of vertical joint directly affected by transverse reinforcement under load control and displacement control methods. Xueyuan Yan et.al [6] investigated the joints of a precast prestressed concrete frame structure and concluded that the precast prestressed concrete joint and the cast-in-place joint had a similar failure mode. The stiffness, bearing capacity, ductility, and energy dissipation were comparable. The experimental performance behavior of precast reinforced panels under seismic loading was conducted by Alberto Pavese et.al [7]. It was observed that the strong association between wall flexure and shear performance, such as the increased wall length results in enhanced shear resistance. But deformation capacity of the precast wall at failure was practically unchanged.

Folić1. R, et.al [8] indicated the lack of feasibility on holistic modeling of structural behaviour i.e., ductility and shearing of prefabricated structures and proposed mathematical models for sufficiently accurate failure assessment of prefabricated reinforced concrete connections. The storey level impact of gravity and lateral loads for wind and earthquake on twelve storeyed precast building was analyzed by A.Surekha et.al [9], Chaitanya Kumar J.D et.al [10] and R. Uday Kumar et. al [11] using ETABS software and analysis of joints conducted according to IS 11447-1985. The axial force, out of plane moments, storey lateral load, shear force, storey drift, storey shear and tensile force on the shear wall with respect to different storeys were compared. It was concluded that the variation of axial force and out-of-plane moment with storeys were linear in nature whereas the variation of lateral loads, shear force, storey drifts and tensile forces with storeys were non-linear. The comparative analysis of large panel structure and a framed structure of a nine storeyed precast building was carried out by Karthick M et.al [12] using ETABS software. The parameters such as lateral loads, maximum deflection, maximum storey drifts, mode shapes, time periods and base shears were compared under loading conditions - dead load, imposed load wind loads, seismic load. It was concluded that the performance of both structures was satisfied and large panel model behaves better. Absar Khan et.al [13] illustrated large panel as a structural element for low cost frameless housing construction. The comparative study on conventional RCC structure and frameless large panel structure was carried out using ETABS-2015 software on parameters such as base shear, fundamental time period and displacement due to lateral load. Large panel structure showed less displacement as wall panel acts as a shear wall and resist the lateral load.

Engström [14] presented the role of the connection in the structural system, the flow of forces through the connections, and basic force transfer mechanisms. The factors include behaviour at normal loading and dynamic loading, performance of structure during the working condition, structural behaviour during the hazards. Bindurani P et.al [15] conducted an analytical study on the precast multi-storey structure located at Boiwada, Mumbai using ETABS. The study focused on two numerical analysis models for vertical joints analysis - a model adequate in moderate seismic zones having a discrete gap consisting of 20mm wide gap between wall panels, connected by diaphragm constraints and an another integrated conservative model with monolithic joints with a shell strip element of 100mm width, tie reinforcement, shear keys and reinforcing dowel bars. The effects - stress, deformation and absolute plastic strain of lateral ground movement on wall to wall connection in precast concrete structures was studied by Ramin Vaghei et.al [16] using non-linear 3D finite element models in ABAQUS software. Ehsan Noroozinejad Farsangi [17] studied the behaviour of connections in precast concrete structures due to seismic loading using the FEA software LUSAS and SAP2000. Finite element analysis was carried out for four types of precast connections - pinned, rigid, semi rigid and a new proposed connection. The beam to column connections were modelled and analyzed in LUSAS as corbel only model, corbel with bolt on beam top, corbel with plate and bolt on beam top and stiffener, and a new type of connection with 10mm plate and bolt of 22mm. The three storied building was modelled and analyzed in SAP2000. Stiffness of the connection was determined, and it was found to be a semi rigid connection and better when used as 10mm plate and bolt of 22mm. It was concluded from analysis that connection stiffness does have a significant effect to the frame member for moment and shear forces under time history loading.

There are limited data on numerical analysis of wall-to-wall joints. It is observed that the joints between prefabricated components should be engineered and installed properly. The important structural parameters considered for prefabricated building analysis are the bending moments, axial force, storey lateral load, shear force, storey drift, under lateral loads. Analysis and design of joints in the component level and connections in the global level of prefabricated structure using analytical methods is one of the thrust areas in the industry.

2.0 Present Work

In order to have a structurally safe system, it is necessary to know the variations of forces and locations of vertical joints in load bearing precast system by properly modeling the structure which is closer to actual behavior. The performance assessment of wall-to-wall joints is carried out as part of study. The scope of work is to identify a rational numerical analytical model to represent wall-to-wall interlocking linkages. The present work constitutes the following steps.

1. Identification of critical piers at walls without opening and walls with opening subjected to loading conditions - dead load, live load and earth quake load - as recommended in IS 875 part 1[18] & part 2[19] and IS: 1893-2016 [20]
2. Identification and analytical modeling of precast wall-to-wall joints as integrated, one link(1-link) and three links (3-link) using ETAB 2016 software
3. Analysis of axial force, in-plane shear and in-plane bending moments - of critical piers with no-joint, integrated, 1-link and 3-link joint systems between vertical wall panels.
4. Storey displacement analysis of complete structure with no-joint, integrated, 1-link and 3-link joint systems between vertical wall panels

Specifications – Building & Wall Structure

The structure considered is a residential apartment located near Devanahalli, Bengaluru. The location falls under moderate exposure condition and lies in earthquake zone II as per IS: 1893-2016 [20]. The specifications of the building considered are as given in Table 1.

Table 1. Precast Building Specifications

No of stories	9
Storey height	3m
Foundation to plinth height	1.5m
Category	Residential
Type	Precast panel system
Area of each flat	35m^2

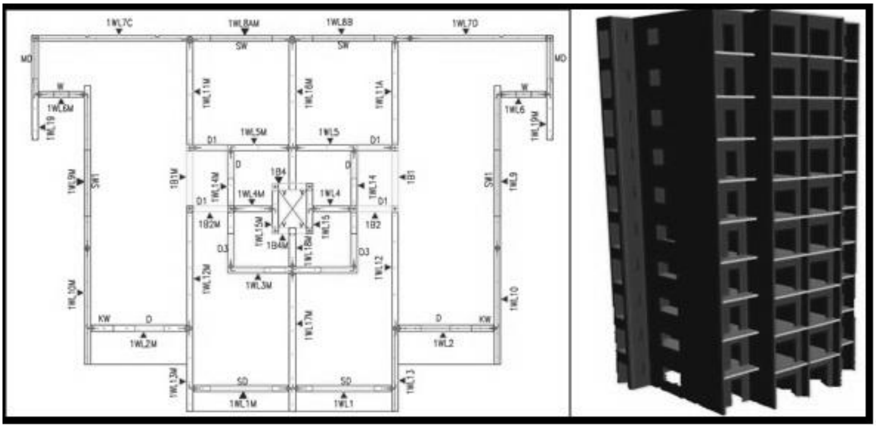

Fig. 1. Precast Building **(a)** Plan and **(b)** 3D View in ETABs

Fig.1a shows the plan of ten storeyed building and Fig.1b depicts its 3D view developed using ETAB Software. Models considered include walls without opening and walls with opening, are considered in the study. The parameters of wall and slab considered in the model are as given in Table 2. In Fig. 2a walls are integrally positioned without any linkage. In Fig. 2b an integrated link having continuous wall-to-wall linkage with 20mm width and 3000mm depth i.e. storey height is shown. Likewise Fig.2c shows a wall-to-wall linkage with single link having 20mm width and 600mm depth at each floor level. Fig. 2c shows wall-to-wall linkage with 3 links of 20mm width and 600mm depth at top, middle and bottom of each storey.

Models with no-link, integrated link, 1-link and 3-link wall-to-wall connection were analyzed under dead load, live load and earthquake load combinations as specified by Indian Standard Codes and the results are compared. The performance of integrated link, 1-link and 3-link wall-to-wall connection were compared with no-link model, which has no wall-to-wall linkage, was considered as a benchmark for results and discussion.

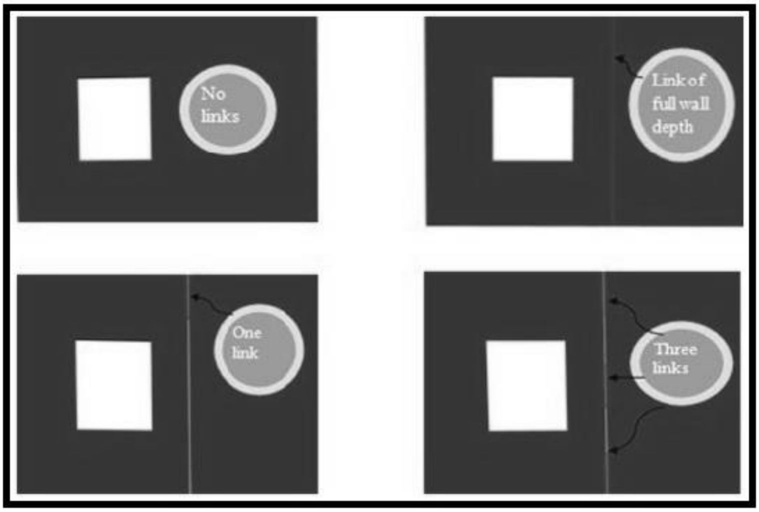

Fig. 2 Wall-to-wall linkage **a)** no-link, **b)** integrated link, **c)** 1-link and **d)** 3-link

Table 2 Wall and Slab Parameters

Section	WALL	SLAB
Material	Concrete	Concrete
Concrete Grade	M40	M40
Steel Grade	Fe 415	Fe415
Type	Shell thin	Membrane
Thickness	160 mm	150 mm

3.0 Results and Discussion

The response spectrum analysis is carried out for analyzing the structure in earthquake zone- II. The analysis is carried out in 3 steps - identification of critical piers, behavior analysis of critical piers in terms of axial force, in-plane shear, in-plane and out-of-plane moments with no-link, integrated-link, 1-link and 3-link wall-to-wall connections and storey displacements.

Step 1: Identification of Critical Piers

Based on the bending moment values observed in analyzed model using ETABs Software, the critical piers are identified for models without opening and with opening. The pier P1, the critical pier of walls without opening, i.e. there is no windows and doors. Similarly, pier P2, the critical pier of walls with opening i.e. with windows and doors fixed in walls.

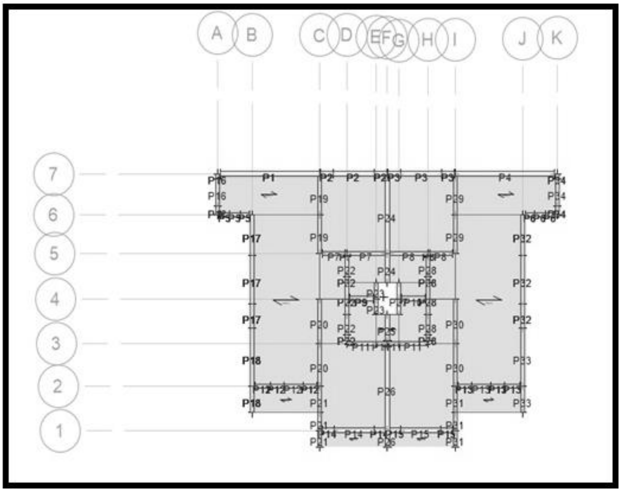

Fig. 3. Precast Building – Critical Pier Identification

Step 2: Behaviour Analysis

The variation of stress variants - axial force, in-plane shear, in-plane bending moment and out-of- plane bending moments are analyzed in this step. The analysis is carried out only on identified critical pier P1 in walls without openings and P2 in walls with openings. The following describes the variations of the stress variants in the walls.

Axial Force

It is observed from Fig.4, that the axial force variation is nearly same in both types of walls at upper floors. But in walls of lower storeys, the variations in axial force upto 19% in integrated link, 17% in 1-link and 25% in 3-link are observed with respect to no-link linkage mechanism of wall-to-wall connections.

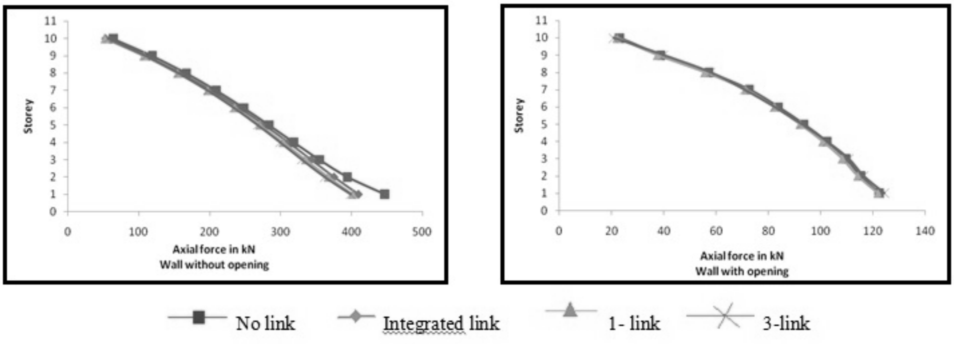

Fig. 4. Axial force variation in critical piers

In-plane shear force

The in-plane shear force variation shown in Fig. 5 for the 3- beam link model, is same in the upper storeys and has lesser variations in bottom storeys in comparison with model without links i.e. upto 39%. Whereas the variations in 1-beam link model is upto 94% and in integrated wall link model is upto 96%.All the variations are compared with respect to no-link linkage mechanism of wall-to-wall connections.

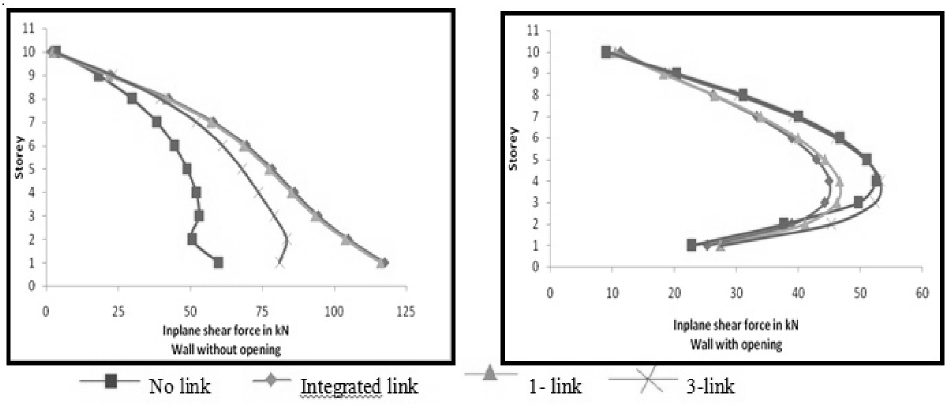

Fig. 5. In-plane shear force variation in critical piers

In-plane bending moment

In-plane bending moment shown in Fig. 6 for the 3-beam link model has variations same in upper storeys and has lesser variations at bottom storeys in comparison with model without links i.e. upto 57%. Whereas the variations in integrated wall link model is upto 110% and in 1- beam link model is upto 109% with reference to the benchmark problem.

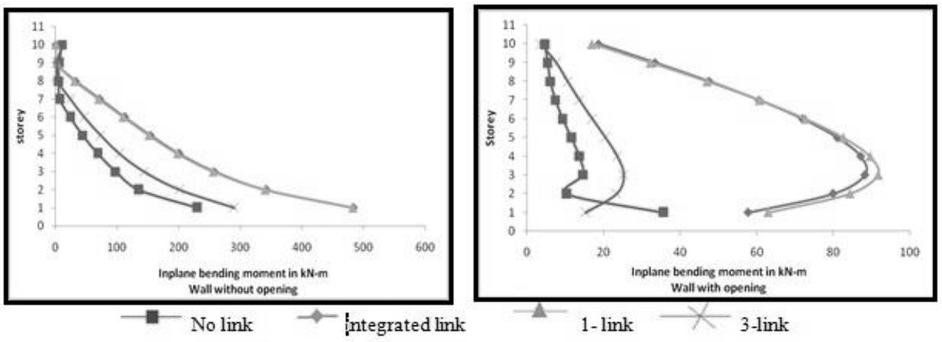

Fig. 6. In-plane bending moment variation in critical piers

Step 3: Storey Displacements

In this step, storey displacements with respect to the base of a structure were assessed. The storey displacements in Fig.7 corresponding to the models with no-link, integrated link, 1-link and 3-link wall-to-wall connections are conservative and do not exceed h/500 where h is building height.

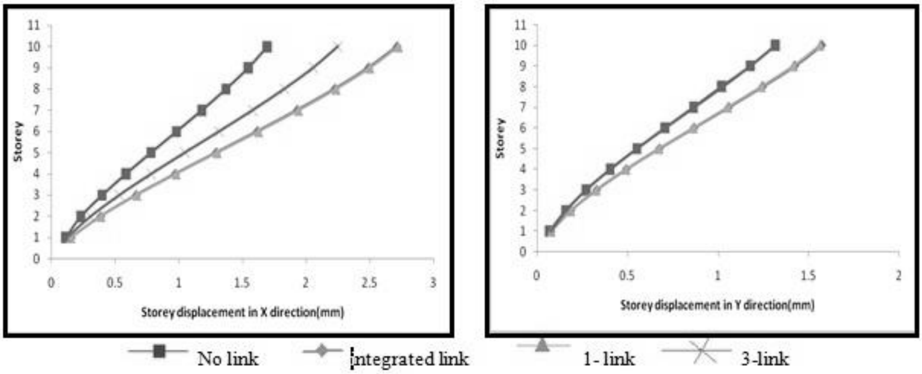

Fig.7. Storey displacement **a)** X-Direction and **b)** Y-Direction

The model with 3-link wall-to-wall connection shows better behavior with a variation of about 32.6% in X direction and matches in Y direction as that of model with no wall-to-wall linkage. Whereas the other linking systems viz, integrated wall link model, 1- beam link model exhibits larger displacements up to 60% in X direction and 20% in Y direction.

4.0 Conclusion

The conclusion of the study on the three types of mechanisms of linkages- integrated, 1- link and 3- link for wall-to-wall interlocking connections are as follows.

It is observed that the 3-link model shows 32%,39% and 57% variation in storey displacements in X-direction, in-plane shear force and in-plane bending moment respectively. It is also observed that the behavior of axial force and storey displacement in Y-direction of 3-link wall-to-wall connection was same as that no-link wall-to-wall connection. Based on the analysis and interpretation of results, wall-to-wall linkage with 3-link is best suited for modeling and analysis of precast wall-to-wall vertical joint compared to integrated wall link model and 1-link model. The outcome of the work will help the structural designer to perform a rational analysis and design of precast concrete walls.

References

1. B Rekha, R Ravindra, Prefabricated Concrete Technology- Perspectives and Challenges, *International Journal of Advances in Scientific Research and Engineering*, 3(1), 444-452, 2017
2. Ivan, Holly, Iyad Abrahoim, Connections and Joints in Precast Concrete Structures, Slovak *Journal of Civil Engineering,* 28(1), 49–56, 2020

3. Bob van Gils, Practical and Economical Design Aspects of Precast Concrete Large Panel Building Structures, *Master builders*, 2010
4. N Rossley, F N A A Aziz, H C Che, Behaviour of precast walls connection subjected to shear load, *Journal of Engineering Science and Technology*, Special Issue, 142 – 150, 2014
5. Aparup Biswal, A Meher Prasad, A K Sengupta, Investigation of shear behaviour of vertical joints between precast concrete wall panels, *The Indian Concrete Journal*, 89(1), 41-47, 2015
6. Xueyuan Yan, Suguo Wang, Canling Huang, Ai Qi and Chao Hong, Experimental Study of a New Precast Prestressed Concrete Joint, *Journal of Applied Sciences*, 8(10), 1-23, 2018
7. Alberto Pavese, Dionysios A Bournas, Experimental assessment of the seismic performance of a prefabricated concrete structural wall system, *Engineering Structures,* 33(6), 2049-2062, 2011
8. Folić1, R Zenunovi, D Rešidbegović Nesib, Strength of connections in precast concrete structures, *Architecture and Civil Engineering,* 9(2), 241–259, 2011
9. A Surekha, J D Chaitanya Kumar, E Arunakanthi, Analysis and connection designs of precast load bearing wall, *International Journal of Research in Engineering and Technology*, 3(9), 449-457, 2014
10. J D Chaitanya Kumar, Lute Venkat, Analysis of multi storey building with precast load bearing walls, *International Journal of Civil And Structural Engineering*, 4(2), 116-122, 2013
11. R Uday Kumar, P. Sai.: Analysis and Design of Precast Load Bearing Walls for Multi-Storey Building, *IJIRT*, 4(8), 341–350, 2018.
12. M Karthick, K Karthikeyan, Comparative Studies on Different types of Precast Structural Systems, *International Journal of Applied Engineering Research*, 10(13), 11660-11666, 2015
13. Absar Khan, P M Kulkarni, Analytical Investigation of Precast Panel and its Utilization in Low Cost Housing, *International Journal of Advance Research and Innovative Ideas in Education (IJARIIE)*, 3(1), 191-195, 2017
14. B Engström, Design of structural connections for precast concrete buildings, BE2008 – Encontro Nacional Betão Estrutural (2008)
15. P Bindurani, A Meher Prasad, A K Sengupta, Analysis of Precast multi storeyed building – A case study, *International Journal of Innovative Research in Science, Engineering and Technology*, 2(1), 294-302, 2013
16. Ramin Vaghei, Farzad Hejazi, Hafez Taheri, Mohd Saleh Jaafar, Abang Abdullah Abang Ali, Evaluate performance of precast concrete wall to wall connection, *Proceedings of Chemical, Biological and Environmental Engineering International Conference*, 9, 285 – 290, 2014
17. Ehsan Noroozinejad Farsangi, Connections behaviour in precast concrete structures due to seismic loading, *Gazi University Journal of Science*, 23(3), 315-325, 2010

18. IS: 875 – 1987 (Part 1) Code of practice for design loads (other than earthquake) for buildings and structures: Dead loads — unit weights of building materials and stored materials.
19. IS: 875 – 1987 (Part 2) Code of practice for design loads (other than earthquake) for buildings and structures: Imposed loads
20. IS: 1893 – 2016 (Part 1) Criteria for Earthquake resistant design of structures-General provisions and buildings.

Vibration and Damping Behaviour of Bamboo/Epoxy Polyurethane Foam Sandwich Structures

M. Krishna*[1], B. S. Suresh[1], Aditya Joshi[1], Ashita Raj[1], Rihan Rajan[1], Soumi Bandyopadhyay[1]

[1]*Department of Mechanical Engineering, RV College of Engineering®, Bengaluru*

Abstract

This research was aimed at fabrication and characterisation of bamboo/epoxy polyurethane sandwich structures for vibration and damping behavior. Sandwich panels with polyurethane foam as core and bamboo/epoxy as facesheets were fabricated using vacuum infusion process. The specimens were characterized for modal and harmonic analyses using FFT analyser and DEWESOFT software. Natural frequency and critical damping increased significantly with increase in foam density. In-plane and out-of-plane vibration characteristics were studied. Fundamental frequency increased exponentially in post-flexural regime. Experimental load vs. deflection and natural frequencies agreed with finite element analysis results.

Keywords: *Sandwich structures, FFT Analyser, Natural frequency, Critical Damping, Finite Element Analysis*

1.0 Introduction

Sandwich structures are used in automotives, aircrafts, submarines, ships and boats, wind blades, etc. [1-3] as they have high strength and stiffness to weight ratios, superior fatigue and thermal properties. If a system vibrates with a frequency equal to that of eigen-frequency of the body, resonance occurs which can cause drastic failure. Damping of a body has the effect of reducing the vibrations in a body. The damping factor describes how the vibrations decay after a period of time. Hence, the vibration and damping analysis of a body is important.

The natural fibre based sandwich structures show good performance under dynamic conditions. Pankaj Charan Jena [4] made samples of different bamboo weight content and conducted mechanical tests. Natural frequencies were seen to increase with the weight content of bamboo. Rajesha et al. [5] studied natural frequency and damping factor of banana and sisal fibres based hybrid composite beam with polyester skins. Fibres are treated with sodium hydroxide. Natural frequency increases initially with increase in fibre content and it decreases for higher fibre loading. [6]. Senthilkumar et al. [7] conducted mechanical and dynamic investigations of composites made from pineapple leaf fibres by studying the influence of the fibre content (25, 35 and 45%) on the properties of

---

**Mail address: M. Krishna, Professor and Head, Department of Mechanical Engineering, RV College of Engineering®, Bengaluru – 59*
Email: krishnam@rvce.edu.in, Ph: 9980480001

the structures. It was observed that the natural frequency increased with fibre content. Chethan et al [8] used urea sheath fibres and epoxy resin. Poly vinyl carbon powder was used as a releasing agent. Rachchh and Trivedi [9] studied mechanical parameters and performed vibration analysis of hybrid sandwich type composite plates made from e-glass / bagasse and polyester resin. It was observed that 9 % bagasse fibre plate showed best vibration and mechanical performance. Vitale et al. [10] studied fibre reinforced honeycomb cores using Vacuum Assisted Resin Transfer Molding with combination of natural fibre cores, PVC foam core and jute reinforced glass fibre skins. Vaswani et al. [11] conducted studies on curved sandwich beam with visco-elastic core (aluminum skin and PVC foam core). Kushwaha et al.[12] conducted experiments on natural fibres such as bamboo, basalt, cotton, flax, hemp, jute, henequen, ramie, sisal, pineapple leaf, kenal, lyocell and wheat straw pulp with different resin types to calculate their interfacial shear strength. Hydrophilic fibre and hydrophobic matrix undergo debonding easily under loading conditions. The objective of the research was to fabricate sandwich structures using bamboo/epoxy as skin and polyurethane foam as core and to conduct vibration analysis on the beam specimens experimentally and using FEM.

2.0 Methodology Adopted

2.1 Surface treatment of fibers

Bamboo fibres were treated using 5% NaOH. Pellets of NaOH were dissolved in water (Fig. 1) and NaOH: fibre in 13:1 wt.% was used. The fibres were soaked for a specific period of time and dried.

2.2 Sandwich Manufacturing

The foam core was cut from a block of foam, having dimensions of 250 x 50 x 8 mm^3. The density of the polyurethane foam used is 70 kg/m^3. Epoxy LY5052 and hardener HY951 (10:1). was applied and bamboo fibres were layed up. The process was repeated for the second layer. Vacuum bagging technique was used to fabricate the specimens. Beams of 250 x 50 x 12 mm^3 were obtained as shown in Fig. 2.

Fig. 2. Beam made with Bamboo epoxy skin and PU foam core

2.3 Vibration Testing

Fast Fourier Transforms (FFT) using DEWESOFT was used for the experimental study. The setup involves the use of an impact Hammer, Accelerometer and an 8 – Channel FFT Analyser. Testing was performed in free-free boundary condition by placing the beam on two low density sponges. Two sets of results for in-plane and out-of-plane vibrations were obtained by placing the accelerometer on the beam(Fig. 3 and 4).

The sandwich beam was marked with four lines for the hammer impact points. Following the test procedure the graph of amplitude and frequency was directly obtained from the software and half power bandwidth method was used to obtain damping factor at the respective points.

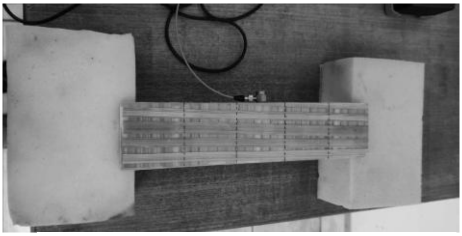

Fig. 3. Accelerometer: in-plane

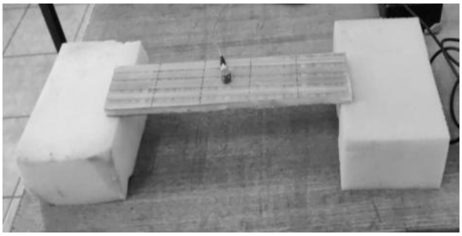

Fig. 4. Accelerometer: out-of-plane

3.0 Experimental Results

From amplitude vs frequency results (Fig. 5 and 6), the natural frequencies of the beam was obtained. The frequency range selected was 0 to 5 kHz. The out of plane vibration denotes that the accelerometer to be attached on the top side of the beam parallel to the ground. Natural frequencies are shown in Fig. 7. The peaks show that the amplitude is maximum at this point. Thus, the corresponding frequencies are the natural frequencies.

The damping factor at each of the peaks are found by first multiplying the peak amplitude by 0.707. The obtained value is then marked on the graph with a horizontal line. The curve meets this line at two points. These two points are then dropped down to find the frequencies f_1 and f_2. The experimental results are plotted Fig. 7 and 8.

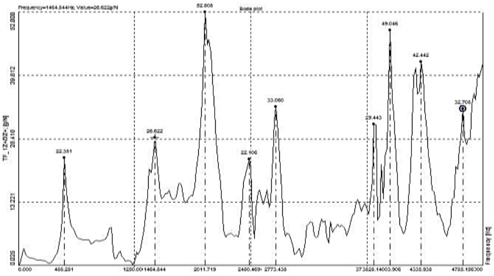

Fig. 5. Out-of-plane vibration Amplitude vs Frequency

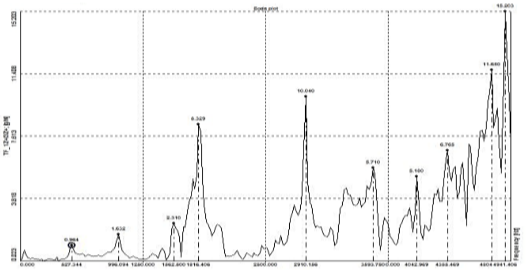

Fig. 6. In-plane vibration Amplitude vs Frequency

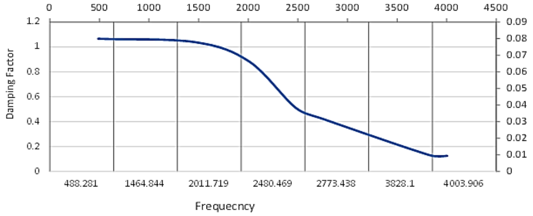

Fig. 7. Damping factor vs. frequency in out of plane vibration of bamboo sandwich structure

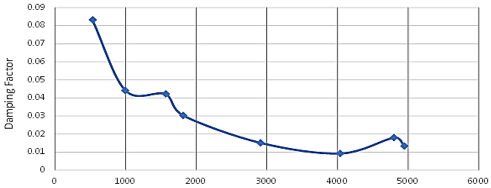

Fig. 8. Damping factor vs. frequency in plane vibration of bamboo sandwich structure

Fig. 9 shows that the three plots are not aligned. The natural frequencies increased with the curvature angle. Variation in natural frequencies in the three beam specimens is due to the change in stiffness of the beams. This pattern is more significant in the higher modes 34 to 50.

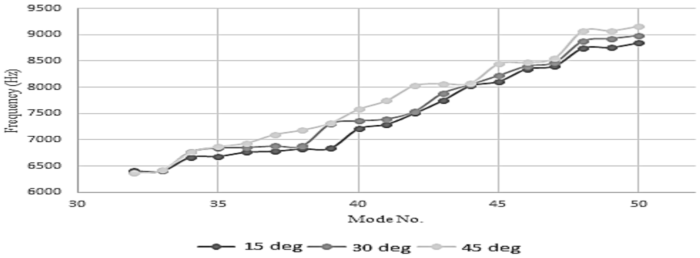

Fig. 9. Higher modes of vibration vs frequency

4.0 Conclusion

- A composite beam was manufactured with bamboo fibres and epoxy resin. The bamboo fibres were treated with 5% NaOH and dried which to enhance their physical properties.

- Vibration analysis was performed using DEWESOFT software with impact hammer method under free-free condition and two sets of results were obtained through in-plane and out-of- plane vibration. The results of in-plane natural frequencies match with that of the Finite Element Analysis.
- Damping factor was computed using half power bandwidth method. The damping factor reduced with increase in frequency.
- Vibration analysis on curved beams having end face angle as 15 degree, 30 degree and 45 degree show that there is a change in the natural frequencies when compared to each other. The natural frequencies tend to increase with curvature which is more significant in higher modes of vibration.

Reference

1. R Jeyapragash, V Srinivasan, S J M T P Sathiyamurthy, Mechanical properties of natural fiber/particulate reinforced epoxy composites–A review of the literature, *Materials today*:Proceedings (article in press) 2020
2. W Ng, M. Johar, H. Israr, K Wong, A review on the interfacial characteristics of natural fibre reinforced polymer composites, *Interfaces in Particle and Fibre Reinforced Composites: Elsevier*, 163-198, 2020,
3. B O Baba, S J C S Thoppul, Experimental evaluation of the vibration behavior of flat and curved sandwich composite beams with face/core debond, *Composite Structures*, 110-119, 2009
4. P C J M T P Jena, Free vibration analysis of short bamboo fiber based polymer composite beam structure," *Materials Today*, 5(2), 5870- 5875, 2018
5. M Rajesh, J Pitchaimani, N J P E Rajini, Free vibration characteristics of banana/sisal natural fibers reinforced hybrid polymer composite beam, *Materials Today* 1055-1059, 2016
6. P Lokesh, T S Kumari, R. Gopi, G B J M T P Loganathan, A study on mechanical properties of bamboo fiber reinforced polymer composite, *Materials Today*: 2019
7. K Senthilkumar Evaluation of mechanical and free vibration properties of the pineapple leaf fibre reinforced polyester composites, *Construction and Bulding Materials*. 423-431, 2019
8. M Chethan, P S N Venkat, G G Krishna, R Chennakesava, P J M T P Vijay, Dynamic Vibrational Analysis on Areca Sheath fibre reinforced bio composites by Fast Fourier Analysis, *Materials Today*, 19330-19339, 2018
9. N Rachchh, D J M T P Trivedi, Mechanical characterization and vibration analysis of hybrid E-glass/bagasse fiber polyester composites, *Materials Today*, 5 (2). 7692-7700, 2018
10. J P Vitale, G Francucci, J Xiong, A J C P A A S Stocchi, Manufacturing, Failure mode maps of natural and synthetic fiber reinforced composite sandwich panels, in *Composites Part A: Applied Science and Manufacturing* (94), 217-225, 2017

11. J Vaswani, N Asnani, B J C s Nakra, Vibration and damping analysis of curved sandwich beams with a visoelastic core, in *Composite Structures 10 (*3), 231-245, 1988
12. P K Kushwaha, R J P-P. T Kumar, Engineering, Studies on water absorption of bamboo-polyester composites: effect of silane treatment of mercerized bamboo, in *Polymer-Plastics Technology and Engineering* 40 (1), 45-52, 2009

Facility Redesign using Systematic Layout Planning

Ramaa A*[1], Vikram N B[1], Nandini B[1]

[1]Department of IEM, RV College of Engineering

Abstract

This paper presents facility redesign of Glazing and Metal Works using systematic layout planning. Process sequence, material flow and activity relationship were studied. The lay-out was designed and simulated. The new layout showed reduced material flow distance by 33%, waiting time by 30% and increased space utilization by 14%.

***Keywords**: Systematic Layout planning, Facility Layout design, Simulation.*

1.0 Introduction

Block layout of facility is designed considering the relationship amongst the departments. Internal layout design deals with placement of equipment, storage space, paths, etc. within the departments [1]. A methodology to redesign plant layout starts with collection of relevant data and information, performing flow analysis along with identifying the supporting services, and ending with implementation of the redesigned plant layout. Flow process charts, flow diagrams and operation process charts are commonly used for studying the existing layout. The common storage rack systems like flow rack system, single deep rack, double deep rack, push back rack can be considered while designing layout of warehouse [2]. For developing alternatives for redesigning the existing facility, factors such as ease of access, space utilization, cost of implementation and long-term viability are selected to evaluate the alternatives [3-4]. Weighted factor comparison can used to choose the best facility layout [5].

In simulation of layout using ARENA, factors such as total travelling distance, total travelling time, travelling cost, number of cross over, output over a certain time duration, average resource utilization, total average work in process, total average waiting time and total time spent in system are used as evaluation factors [6 -7]. Efficiency indices can be used to evaluate the existing and proposed layout. Direct material handling, production line flexibility and aisle space are some of the efficiency indices which can be used to indicate an improvement in efficiency of the proposed layout [8]. Material flow distance is used to compare the proposed layout with the existing [9] and adjacency score can be used for the evaluation [10]. The main objective of this paper was to redesign production floor layout of a department using Muther's Systematic Layout Planning (SLP) methodology. Alternative layouts were simulated using ARENA simulation tool.

**Mail address: Ramaa A, Associate Professor, Dept. of IEM, RV College of Engineering®, Bengaluru – 59*

Email: ramaa@rvce.edu.in, Ph: +91 9886846831

2.0 Methodology

The study was undertaken in Glazing and Metal Works factory in which the process layout was followed with incidences of back tracking and unnecessary movements. Placement of machines resulted in unsmooth and discontinuous movement of parts between machines. Unused machines and empty spaces present between the lines hindered movement of workers and the parts. The space utilization was only 70% of the total available 1.3 x 10^5 sq. feet.

2.1 Study of Existing lay-out

Aluminum fabrication, mild steel fabrication and stainless steel fabrication were the three main fabrication units. Detailed analysis was performed on two major products from each of the three units: window and panel in aluminum fabrication, bracket and canopy in mils steel fabrication and pipe and railing in stainless steel fabrication. Operation process charts for these products are shown in Fig. 1 to 3.

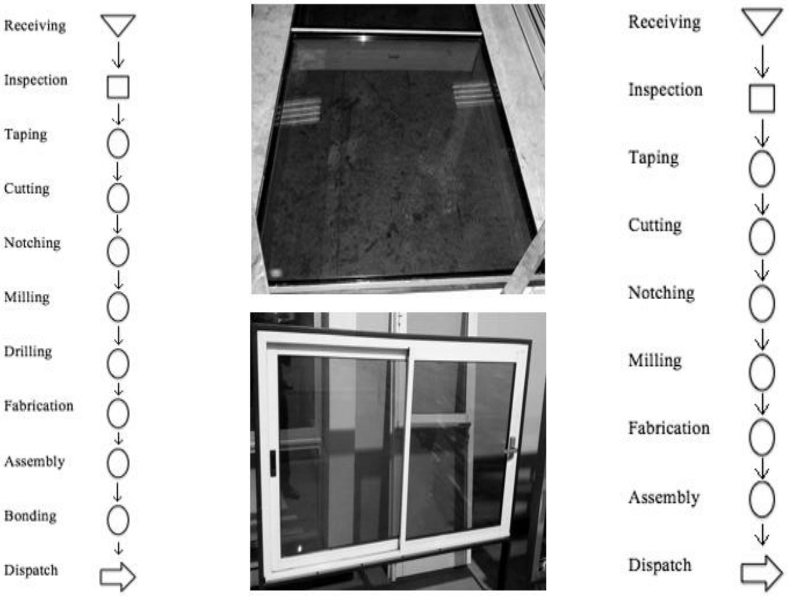

Fig. 1. Operation Process Charts for aluminium Panels and windows

Fig. 2. Operation process charts for MS brackets and canopies

Fig. 3. Operation process charts for SS pipes and railings

Existing layout is shown in Fig. 4.

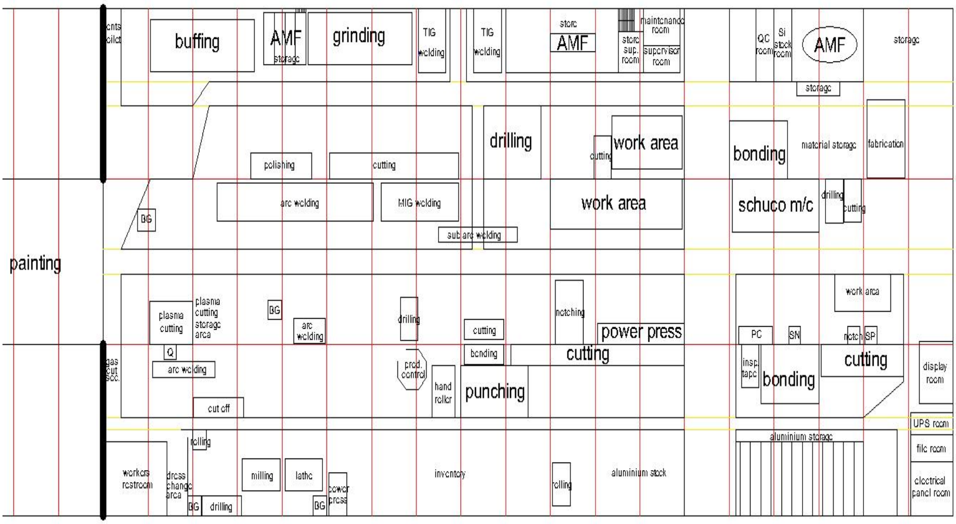

Fig. 4. Layout of existing facility - Department

2.2 Systematic Layout Planning

2.2.1 Material Flow

Flow of materials for aluminum products through the facility is mapped using AutoCAD (Fig. 5). It depicts both forward (blue) and backward (green) movements. Materials flow for other products was also studied.

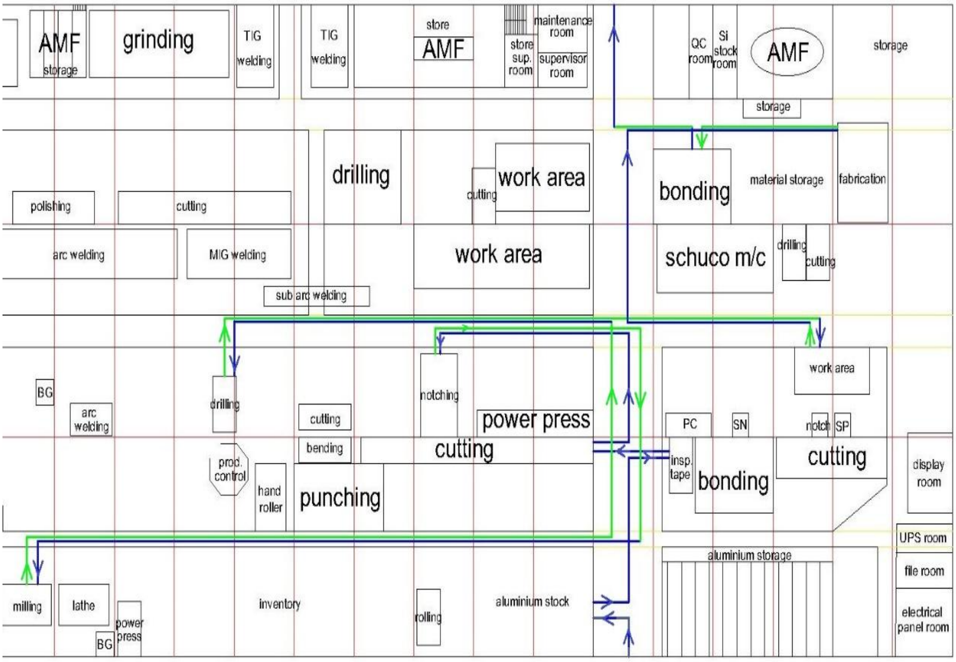

Fig. 5. Material flow process for aluminium panels

2.2.2 Mileage chart

FROM-TO chart data serves as baseline and is useful for finding the degree of closeness necessary between different departments for material interaction. Table 1 represents linear distances between different departments for each major process in aluminium fabrication. Similarly, mileage charts for the other two fabrications were studied. Departments having more material movement were placed together to minimize material handling and to ensure an optimum material flow.

Table 1. Mileage Chart - aluminum fabrication

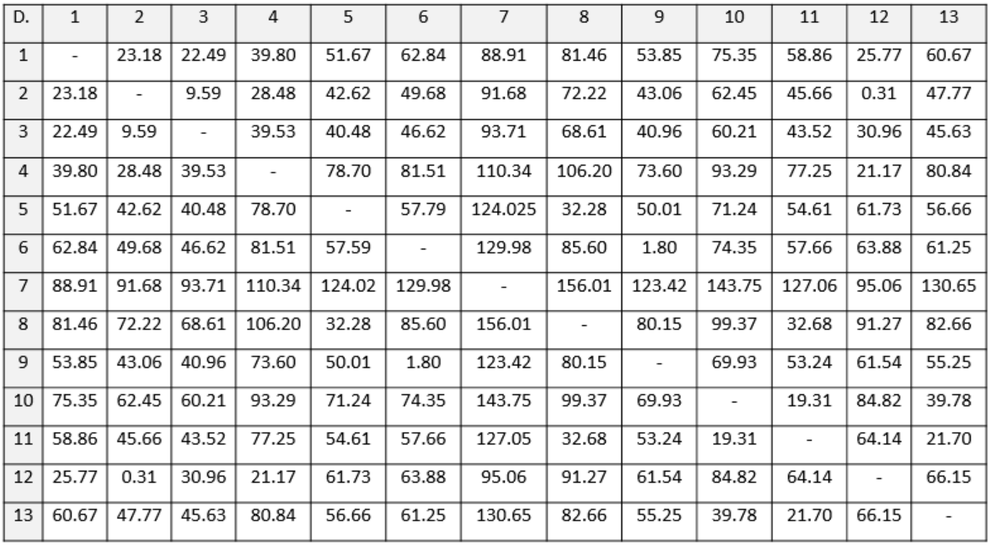

D.	1	2	3	4	5	6	7	8	9	10	11	12	13
1	-	23.18	22.49	39.80	51.67	62.84	88.91	81.46	53.85	75.35	58.86	25.77	60.67
2	23.18	-	9.59	28.48	42.62	49.68	91.68	72.22	43.06	62.45	45.66	0.31	47.77
3	22.49	9.59	-	39.53	40.48	46.62	93.71	68.61	40.96	60.21	43.52	30.96	45.63
4	39.80	28.48	39.53	-	78.70	81.51	110.34	106.20	73.60	93.29	77.25	21.17	80.84
5	51.67	42.62	40.48	78.70	-	57.79	124.025	32.28	50.01	71.24	54.61	61.73	56.66
6	62.84	49.68	46.62	81.51	57.59	-	129.98	85.60	1.80	74.35	57.66	63.88	61.25
7	88.91	91.68	93.71	110.34	124.02	129.98	-	156.01	123.42	143.75	127.06	95.06	130.65
8	81.46	72.22	68.61	106.20	32.28	85.60	156.01	-	80.15	99.37	32.68	91.27	82.66
9	53.85	43.06	40.96	73.60	50.01	1.80	123.42	80.15	-	69.93	53.24	61.54	55.25
10	75.35	62.45	60.21	93.29	71.24	74.35	143.75	99.37	69.93	-	19.31	84.82	39.78
11	58.86	45.66	43.52	77.25	54.61	57.66	127.05	32.68	53.24	19.31	-	64.14	21.70
12	25.77	0.31	30.96	21.17	61.73	63.88	95.06	91.27	61.54	84.82	64.14	-	66.15
13	60.67	47.77	45.63	80.84	56.66	61.25	130.65	82.66	55.25	39.78	21.70	66.15	-

2.2.3 Activity Relationship Chart

Value	Closeness	Line code	Allocation
A	Absolutely necessary	≣	5%
E	Especially Important	≡	10%
I	Important	=	15%
O	Ordinary Closeness OK	—	20%
U	Unimportant		50%

Activity Relationship Chart between pairs of departments were derived by the From-To chart, mileage chart and material flow. The relationship chart displays which departments are related to others and it also rates the importance of the closeness between them. The relationship chart for all 3 fabrications were prepared after considering both quantitative data of distances travelled as well as the qualitative data collected from the working personnel. Fig. 6 displays the activity relationship chart of aluminum fabrication.

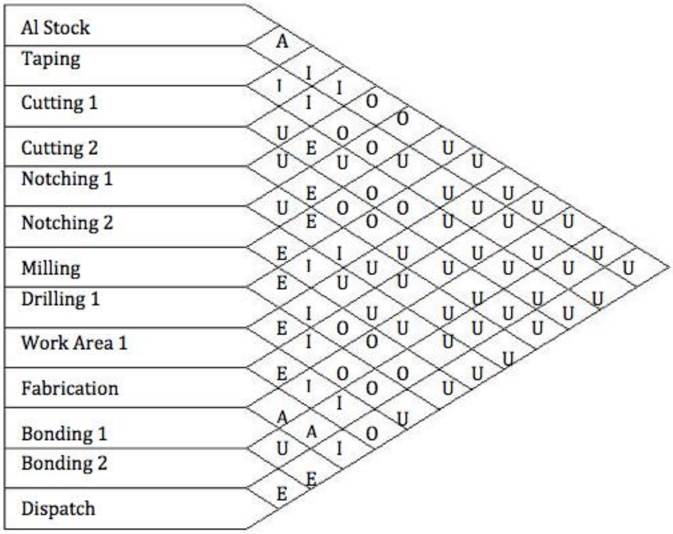

Fig. 6. Activity Relationship Chart - Al Fabrication

2.2.4. Space Relationship Diagram

This is the next crucial step in SLP. Considering the material flow and the relationship between each department, space relationship diagram for aluminum fabrication was generated (Fig. 7). It makes the proximity and relationship between two departments visually evident. The activity relationship diagrams for mild steel and stainless steel fabrication were also generated.

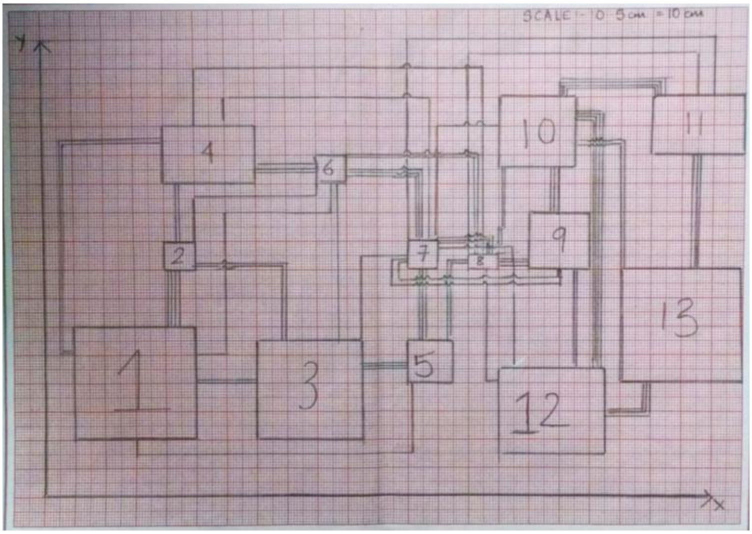

Fig. 7. Space Relationship Diagram - Al Fabrication

2.2.5. Space Requirements

The total working area of departments was collected which indicates the space required for each department. It is used in generating the alternative layouts for the facility. It is converted into the required area and the alternative block plans are derived using the areas for each department.

2.2.6 Closeness Relationship Matrix

This is the final step in SLP. A closeness relationship matrix is made using the activity relationship chart as an input. Weights are assigned to each relationship: A=10000, E=1000, I=100, O=10, U=0, X=-1000. Total closeness rating (TCR) for each department is calculated using the above weights. The department with the highest TCR is selected and located at the centre of the proposed layouts. The departments are selected from highest to lowest TCR while developing the alternative layouts, and are placed around the centre department and the dimensionless diagram is generated for aluminium fabrication as shown in table 2 and Figure 8. The TCR for the other two fabrications are also calculated.

Table 2. Total Closeness Ratings - Al Fabrication

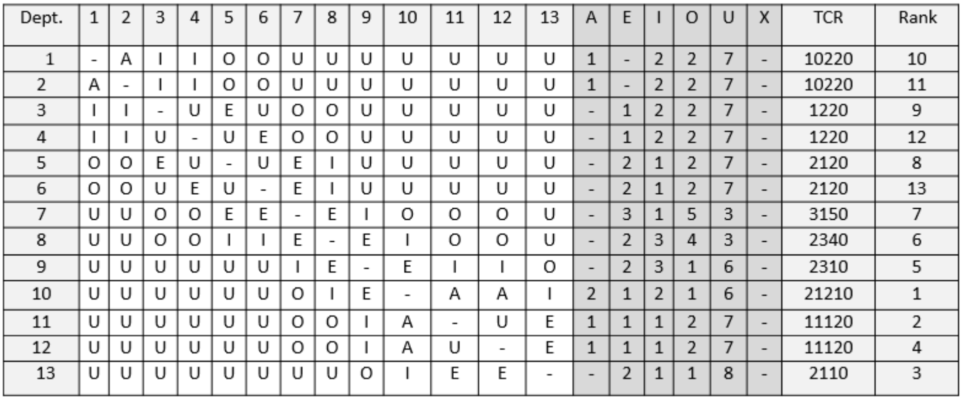

Dept.	1	2	3	4	5	6	7	8	9	10	11	12	13	A	E	I	O	U	X	TCR	Rank
1	-	A	I	I	O	O	U	U	U	U	U	U	U	1	-	2	2	7	-	10220	10
2	A	-	I	I	O	O	U	U	U	U	U	U	U	1	-	2	2	7	-	10220	11
3	I	I	-	U	E	U	O	O	U	U	U	U	U	-	1	2	2	7	-	1220	9
4	I	I	U	-	U	E	O	O	U	U	U	U	U	-	1	2	2	7	-	1220	12
5	O	O	E	U	-	U	E	I	U	U	U	U	U	-	2	1	2	7	-	2120	8
6	O	O	U	E	U	-	E	I	U	U	U	U	U	-	2	1	2	7	-	2120	13
7	U	U	O	O	E	E	-	E	I	O	O	O	U	-	3	1	5	3	-	3150	7
8	U	U	O	O	I	I	E	-	E	I	O	O	U	-	2	3	4	3	-	2340	6
9	U	U	U	U	U	U	I	E	-	E	I	I	O	-	2	3	1	6	-	2310	5
10	U	U	U	U	U	U	O	I	E	-	A	A	I	2	1	2	1	6	-	21210	1
11	U	U	U	U	U	U	O	O	I	A	-	U	E	1	1	1	2	7	-	11120	2
12	U	U	U	U	U	U	O	O	I	A	U	-	E	1	1	1	2	7	-	11120	4
13	U	U	U	U	U	U	U	U	O	I	E	E	-	-	2	1	1	8	-	2110	3

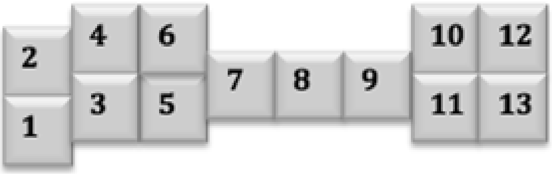

Fig. 8. Activity Relationship Diagram-Al Fabrication

2.2.7 Transportation Cost Matrix

Transportation cost matrix is a quantitative method that is used to draw a comparison between the existing and the proposed layouts. It is the product of production volume, distance and cost of the respective matrices. In the cost matrix, it is assumed that all backward moves cost $1.25/unit volume/ unit distance and all forward moves cost $1/unit volume/ unit distance.

The Formula used for total transportation cost is

$$\sum_{i=1}^{N}\sum_{j=1}^{N} \mathbf{f_{ij} * dij * cij}$$

where,

f is the production volume to and from departments

d is the distances between the departments

c is the cost for the moves between the departments

i is the department from which the material flows

j is the department to which the material flows

N is the number of departments

The sum of the resultant matrix is the facility transportation cost. The cost matrix and transportation matrix for the aluminum fabrication is shown in Table 4 and 5. The same procedure is conducted for the other two fabrications as well.

Table 3. Cost Matrix - Aluminium Fabrication

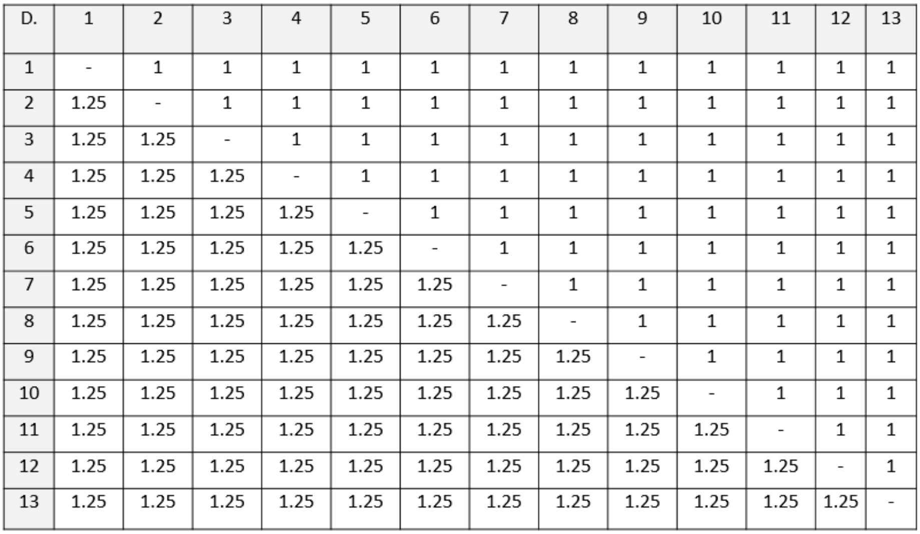

D.	1	2	3	4	5	6	7	8	9	10	11	12	13
1	-	1	1	1	1	1	1	1	1	1	1	1	1
2	1.25	-	1	1	1	1	1	1	1	1	1	1	1
3	1.25	1.25	-	1	1	1	1	1	1	1	1	1	1
4	1.25	1.25	1.25	-	1	1	1	1	1	1	1	1	1
5	1.25	1.25	1.25	1.25	-	1	1	1	1	1	1	1	1
6	1.25	1.25	1.25	1.25	1.25	-	1	1	1	1	1	1	1
7	1.25	1.25	1.25	1.25	1.25	1.25	-	1	1	1	1	1	1
8	1.25	1.25	1.25	1.25	1.25	1.25	1.25	-	1	1	1	1	1
9	1.25	1.25	1.25	1.25	1.25	1.25	1.25	1.25	-	1	1	1	1
10	1.25	1.25	1.25	1.25	1.25	1.25	1.25	1.25	1.25	-	1	1	1
11	1.25	1.25	1.25	1.25	1.25	1.25	1.25	1.25	1.25	1.25	-	1	1
12	1.25	1.25	1.25	1.25	1.25	1.25	1.25	1.25	1.25	1.25	1.25	-	1
13	1.25	1.25	1.25	1.25	1.25	1.25	1.25	1.25	1.25	1.25	1.25	1.25	-

Total Transportation Cost for Aluminum was Rs. 3.64×10^5, Mild Steel Rs. 4,841.4 and Stainless Steel Rs. 1.37×10^5, totaling to Rs. 5.06×10^5.

3.0 Redesign of Existing lay-out

The data collected from the analysis phase of the layout planning was used in proposing a new layout (Fig. 9). The dimensionless block diagrams prepared based on the relationship chart serves as a basis for the new layout. SLP technique resulted in the new plant layout after taking into consideration practical limitations and constraints and is shown in Fig. 9. When the material flow was observed in proposed method, it was seen that the backtracking was reduced significantly. From the proposed mileage chart it was observed that the distance between the departments for each of the fabrication has reduced drastically. From To chart and the cost matrix for the proposed layout is same as the existing layout.

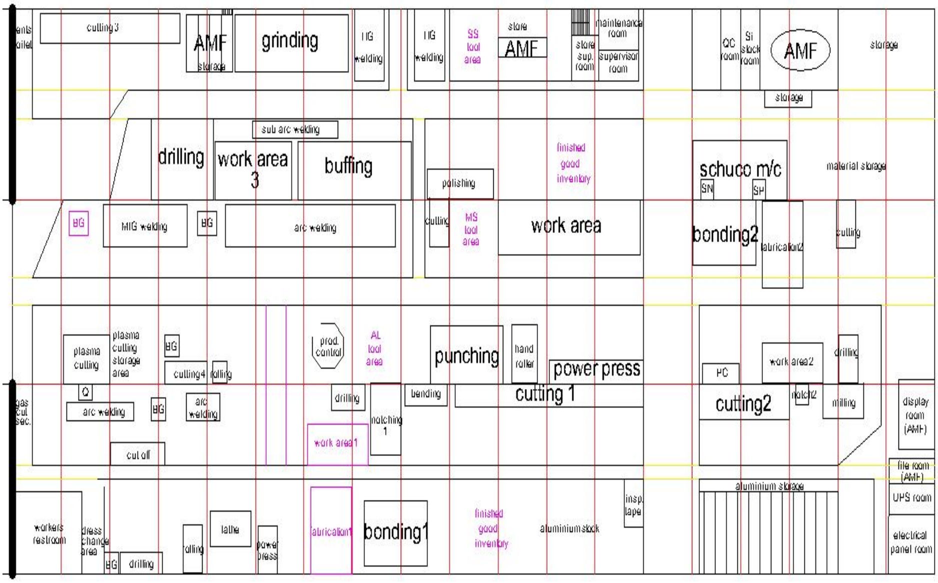

Fig. 9. Proposed Layout

3.1 Transportation Cost Matrix - Proposed

The transportation costs for the proposed layout was computed. Table 4 and 5 represent the transportation cost and summary of transportation costs for aluminum fabrication.

Table 4. Transportation Cost Matrix – Al Fabrication

	1	2	3	4	5	6	7	8	9	10	11	12	13	14	15
1	0	3883	0	0	0	0	0	0	0	0	0	0	0	0	0
2	0	0	3140	2986.5	0	0	0	0	0	0	0	0	0	0	0
3	0	0	0	0	5844	0	0	0	0	0	0	0	0	0	0
4	0	0	0	0	0	157.5	0	0	0	0	0	0	0	0	0
5	0	0	0	0	0	0	32452	0	0	0	0	0	0	0	0
6	0	0	0	0	0	0	330	0	0	0	0	0	0	0	0
7	0	0	0	0	0	0	0	36080	12650	0	0	0	0	0	0
8	0	0	0	0	0	0	0	0	0	0	0	0	0	38864	0
9	0	0	0	0	0	0	0	0	0	0	0	0	9435	0	0
10	0	0	0	0	0	0	0	0	0	0	0	0	0	0	0
11	0	0	0	0	0	0	0	0	0	0	0	0	23220	0	0
12	0	0	0	0	0	0	0	0	0	0	0	0	0	0	0
13	0	0	0	0	0	0	0	0	0	0	0	0	0	0	0
14	0	0	0	0	0	0	0	0	0	0	0	0	0	0	2404
15	0	0	0	0	0	0	0	0	0	0	16315	0	0	0	0

Table 5. Summary of Transportation Cost – Al Fabrication (in Rs)

Sl No	Fabrication	TC (Existing)	TC (Proposed)
1	Aluminum	2.84×10^5	1.87×10^5
2	Mild Steel	4,841.4	799.9
3	Stainless Steel	1.37×10^5	1.37×10^5
	Grand Total	4.26×10^5	3.24×10^5

3.2 Simulation

To evaluate the proposed layout, comparisons on certain key performance indices between the existing layout and proposed layout are performed. The indices used to evaluate the effectiveness of the proposed layout are waiting time, % utilization and number of products produced in the case study. Simulation was performed to evaluate the performance. First, cycle time and the waiting time of each process are collected. The distribution of data is determined using the ARENA input analyzer. Three simulation models were prepared for this study. The simulation process involves the parts arrival, processing at different stations and finally shipped. The simulation was executed for one month, eight hour and two shifts per day basis.

4.0 Results

The sample simulation model of Aluminum Fabrication department is shown in Figure 10. Simulation results are summarized in Table 6 and overall comparison of existing and proposed layouts are presented in Table 7.

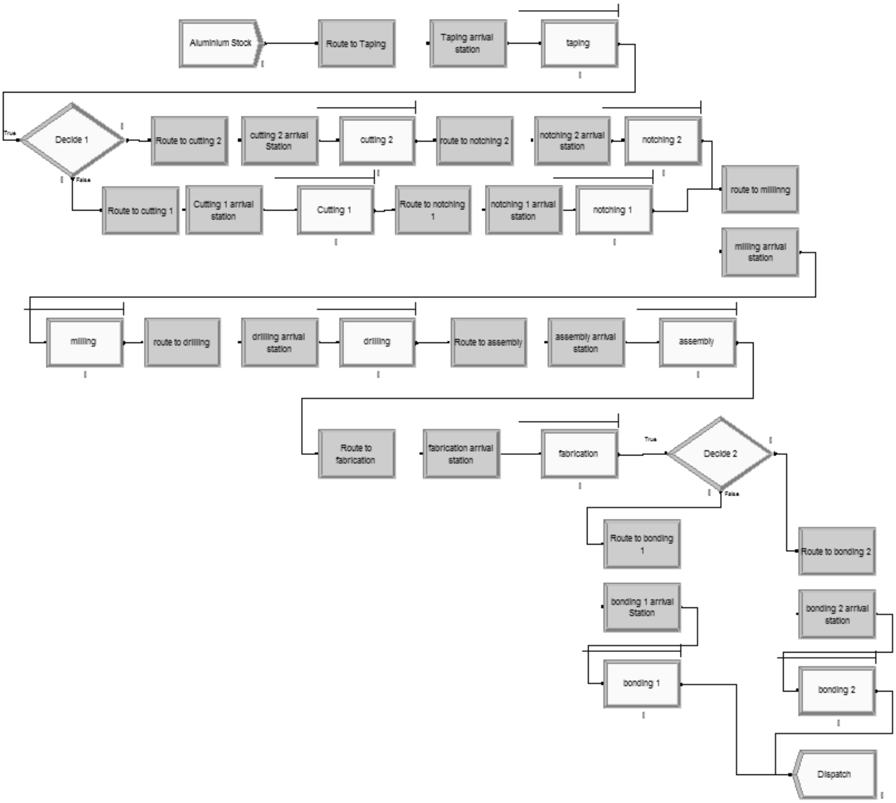

Fig. 10. Simulation model of the proposed method of aluminum fabrication unit

Table 6. Summary of simulation results

Sl. No	**Fabrication**	**No of Products produced (16 hours)**		**Waiting time (minutes per 16 hours)**		**% Utilization**	
		Existing	Proposed	Existing	Proposed	Existing	Proposed
1	Aluminum	276	279	51.16	28.9	65.82	85.56
2	Mild Steel	81	82	256.8	187.2	72.54	86.81
3.	Stainless Steel	80	81	57.13	39.04	79.83	85.62

Table 7. Results of Existing vs. Proposed Layout

Sl. No	Metric	Existing	Proposed
1.	Transportation Cost (Rs)	4.26×10^5	3.24×10^5
2	No of Products	437	442
3	Waiting Time (min)	365.09	255.14
4	Distance(m)	1364.01	914.03
5	% Utilization	72.73	85.99
6	Space utilization (%)	72.73	85.99
7	Net revenue (Rs – crore)	152	153.56

5.0 Conclusion

Facility layout of Glazing and Metal Works was redesigned using systematic layout planning. Data on the existing layout was obtained by using Process sequence, material flow and activity relationship. The lay-out was designed and simulated. The new layout showed reduced material flow distance by 33%, waiting time by 30% and increased space utilization by 14%.

References

1. Bartholdi, J John, Steven T Hackman, Warehouse & Distribution Science: Release 0.89. *Atlanta: Supply Chain and Logistics Institute*, 2008

2. Rouwenhorst, Bart, B Reuter, V Stockrahm, Geert-Jan van Houtum, R J Mantel, Willem HM Zijm, Warehouse design and control: Framework and literature review, *European journal of operational research*, 2000, 122(3), 515-533

3. Master, R Tobiah, Warehouse Redesign of Facility Layout, Racking System and Item Classification at Sunrize Tackle, Inc., 2009

4 Gu, Jinxiang, Marc Goetschalckx, Leon F McGinnis, Research on warehouse design and performance evaluation: A comprehensive review, *European Journal of Operational Research*, 2010, 203 (3), 539-549

5 De Koster, René, Tho Le-Duc, Kees Jan Roodbergen, Design and control of warehouse order picking: A literature review, *European Journal of Operational Research*, 2007, 182(2), 481-501

6 J Gu, M Goetschalckx, L F McGinnis, Research on warehouse operation: A comprehensive review, *European Journal of Operational Research*, 2007, 177(1), 1-21

7 M Rajesh, N V R Naidu, P Naveen Kumar, Plant layout optimization of oven manufacturing unit using CORELAP algorithm, *International Journal of Research in Engineering and Technology*, 2016, 5(16)

8 Hakim, Inaki Maulida, Vidyahningtyas Istiyanti, Improvement of layout production facilities for a secondary packaging area of a pharmaceutical company in Indonesia using the CORELAP method, *International Journal of Technology*, 2015, 6(6), 1006-1016

9 Baker, Peter, Marco Canessa, Warehouse design: A structured approach, *European journal of operational research*, 2009, 193(2), 425-436

10 Ali Naqvi, Syed Asad, Productivity improvement of a manufacturing facility using systematic layout planning, *Cogent Engineering*, 2016, 3(1), 1207296

RV College of Engineering®

Go, change the world

Autonomous Institution Affiliated to Visvesvaraya Technological University, Belagavi

Approved by AICTE, New Delhi, Accredited by NAAC, Bengaluru

Centre of Excellence Computational Genomics

The Centre of Excellence in Computational genomics aims to develop the-state-of-the-art research infrastructure in computational biology. Computational genomics is the study of deciphering biology from genome sequences using computational analysis, including both DNA and RNA. Computational genomics includes: bio-sequence analysis, gene expression data analysis, phylogenetic analysis, and more specifically pattern recognition and analysis problems such as gene finding, motif finding, gene function prediction, fusion of sequence and expression information, and evolutionary models.

The Centre is engaged in upskilling, Research and Development in Computational Genomics with special focus to agriculture and healthcare. The thematic areas under Genomics include Whole genome analysis, RNA-sequence Analysis and Functional Metagenomics. The areas under Drug Design and Informatics include Receptor and Ligand based drug design, Steered molecular dynamics, Trans membrane simulations and QSAR studies.

The Centre has several research projects sponsored by Department of Biotechnology, New Delhi. The projects are undertaken in collaboration with Central Sericultural Research and Training Institute, Mysore, Gandhi Krishi Vignana Kendra, University of Agricultural Sciences, Bangalore and Premier Universities and Institutions in India and abroad.

Partner Organisations of the Centre

RV College of Engineering®

Go, change the world

Autonomous
Institution Affiliated
to Visvesvaraya
Technological
University, Belagavi

Approved by AICTE,
New Delhi, Accredited
by NAAC, Bengaluru

RV-Mercedes Benz Centre for Automotive Mechatronics

RV-Mercedes Benz Centre for Automotive Mechatronics aims to impart the-state-of-the-art education in Advanced Automotive Mechatronics, in collaboration with Mercedes-Benz India. The curriculum is designed by Mercedes-Benz India and the laboratory infrastructure on par with international standards (German Technology) is established by RV College of Engineering. The engineering knowledge and technical skills acquired by the graduates find relevance for Technician Engineers in Automotive Dealerships, Automotive manufacturing industries and automotive Research and Development. The course curriculum has five modules: Mechanical Module, Electronics Module, Advanced Automotive Systems, Soft Skills and Internship in Automotive Dealership.

Aggregate lab

Mechanical module activity

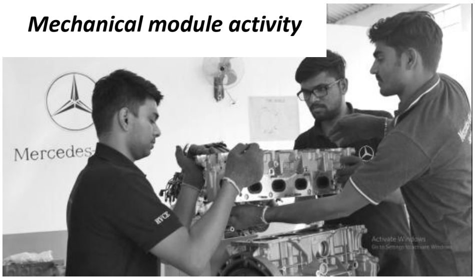

Electrical Lab

Car Bay

RV College of Engineering®

Go, change the world

Autonomous
Institution Affiliated
to Visvesvaraya
Technological
University, Belagavi

Approved by AICTE,
New Delhi, Accredited
by NAAC, Bengaluru

Centre of Excellence on Macroelectronics

The Centre of Excellence in Macroelectronics is established for design and development of flexible electronics devices, sensors, solar cells and TFT for diverse applications such as health care, defense and communication. The centre is engaged in fabrication and characterisation of new class of materials, devices and systems based on nanomaterials, amorphous semiconductors, polymers, metal oxides and MEMS.

Interdisciplinary Research Center (IDRC) is established under the CoE to leverage the institutional interdisciplinary expertise and collaboration with industries for research and development in thin film sensors and Nanocoatings. The research infrastructure is developed through sponsored research projects of DST, DRDO, UGC, AICTE, VGST, TEQIP – II [sub component 1.2 and 1.2.1] grants and Rashtreeya Sikhana Samithi Trust (RSST) funds.

Major processing infrastructure of the centre includes sputtering system (Metallisation unit), Plasma enhanced CVD, Evaporation unit, Dual coating system (Sputtering and PECVD), Plasma Deposition System, Laser writer, Sono Scan and Plot, Cathodic Arc System, Ball Mill, CO_2 Laser, Spin Coater and Electrospinning System. Characterisation systems include FTIR, UV Vis Spectroscopy, Scanning nearfield Optical Microscope, Surface Profilometer, Atomic Force Microscope, Nanoindentation, SEM, Microhardness Tester, XRD, Zeta Potential (Particle Analyser), Thickness Measuring Unit, DSC, Micro Raman and Electrical Resistivitymeter.

Major projects undertaken under the centre include, Design and fabrication of hetero-junction amorphous silicon solar cells for superior efficiency, Oxide nanoparticles of novel metals for plasmonic amorphous silicon solar cells, Development of Diode and Amorphous Silicon TFT, Growth and Characterisation of ZnO thin films, room / low temperature grown Nanocluster carbon based TFT, Metal Oxide Thin films, Doped Metal Oxide films for sensor applications, PVDF and PVDF / nanofiller films for sensor and multilayer electrospun nanofibres for protective clothing.

RV College of Engineering® **Go, change the world**

Autonomous Institution Affiliated to Visvesvaraya Technological University, Belagavi | Approved by AICTE, New Delhi, Accredited by NAAC, Bengaluru

CISCO-RVCE Centre of Excellence in IoT

Centre of Excellence (CoE) in Internet of things is a joint initiative of RVCE and the Networking giant CISCO. The centre aims to develop skills for design and implementation of IoT solutions in different domains through upskilling, research, innovation and incubation.

Modules of Upskilling and Research offered by CISCO-RVCE CoE:

- Intelligent Analytics - Data Analytics and Predictive Analytics, Machine Learning Algorithms, Tools: R, Hadoop, Weka and Matlab
- Embedded Systems for IoT- Hardware and Software of Embedded Systems
- IoT Application Development - Basics of IoT and Electronics, Rasberrypi, Arduino, and nodemcu, interfacing the sensors with Arduino boards and Webpearl with nodemcu and JavaScript based applications.
- Intelligent Transportation Systems - Design of IoT enabled safer, smarter and sustainable transportation systems
- Networking for IoT - Networking Architecture, Computing approaches, Techniques and protocols
- Industrial Internet of Things (IIoT) - IoT enabled Industrial Automation, intelligent industrial operations through advanced data analytics for controlling machines
- RF System Design for IoT Networking - Zigbee, Wi-Fi, Lora based networks

The Centre has established similar centres in Jawaharlal Nehru National College of Engineering (JNNCE), Shimoga and Gogte Institute of Technology, Belagavi. Setting up of CoE and IoT lab in YMCA Faridabad is in process.

The centre has conducted upskilling programmes in IoT in RVCE and elsewhere in India along with quiz and Hackathon on IoT.

RV College of Engineering®

Go, change the world

Autonomous Institution Affiliated to Visvesvaraya Technological University, Belagavi

Approved by AICTE, New Delhi, Accredited by NAAC, Bengaluru

GREAVES
SINCE 1859
Greaves Cotton Limited

Centre of Excellence for e-Mobility

The Centre of Excellence in e-Mobility is established in collaboration with Greeves Cotton Limited with an aim to create a platform for academia and industry to interact, innovate and co-create newer technologies for the EV industry. The centre is engaged in developing futuristic electric vehicle solutions in areas such as Next Generation Controllers, Battery, Thermal Management, embedded design for connected vehicles and application development for electrical mobility.

Graves Cotton Limited is committed to develop competence in RVCE through its UG and PG Students Internship, and Exchange program for training in following areas:

- Electric vehicle Design
- Electric vehicle Architecture
- Functional Safety in Electric vehicles through ISO26262
- Vehicle Styling and Industrial Design
- Sub Systems Design like Controller, Motor, Battery Systems, Regenerative Braking, Connected Vehicles etc.
- Verification and Validation of Sub Systems and Reliability Engineering
- Concepts of HALT, HAST and MEOST in Accelerated testing
- EMI/EMC of sub systems and Vehicles

The centre has identified the following projects for the first year of its operations:

- Controller Design for 1.2 kW and 3 kW BLDC Traction Motors
- BMS Design for Lion battery
- CAN Based telematics Gateway Unit for Preventive Diagnostics
- Application Software for special features in EV – IP shared by RVCE and GCL
- Development of Hybrid battery solution with Ultra Capacitors

RV College
of Engineering®
Go, change the world
Autonomous
Institution Affiliated
to Visvesvaraya
Technological
University, Belagavi
Approved by AICTE,
New Delhi, Accredited
by NAAC, Bengaluru
rexroth
A Bosch Company

BOSCH REXROTH – RVCE Centre of Excellence in Automation Technologies

The Centre of Excellence in Automation technologies is established for upskilling, research and development and industrial consultancy in diverse areas of automation with hydraulics and pneumatics. The interdisciplinary centre is engaged in building hydraulic and pneumatic circuits, designing ladder logic circuit using PLC and demonstrating automated assembly sections using Mechatronics systems for various applications. The centre is equipped with high end equipment such as hardware training kits, PLC which support internet gateway for cloud communication, motion control PLC and CNC simulator MTX.

The centre is upgraded with Industry 4.0 kit, high end XM PLC, L65 PLC to cater to the training needs of one of the modules of CISCO-RVCE in IIoT. The centre is engaged in training industrial professionals, students of RVCE and Institutions elsewhere in Karnataka. Major industrial consultancy projects undertaken by the centre include: Design and Development of 4 degrees of freedom Collaborative Robot which can pick 3 kg load with a reach of 550 mm, Development of Electric and Pneumatic actuation based Cartesian robot for pick and place operation and Design and development of robotic arm to place toys on the conveyor.

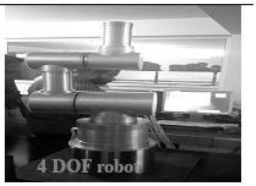

RV College of Engineering® **Go, change the world**

Autonomous Institution Affiliated to Visvesvaraya Technological University, Belagavi | Approved by AICTE, New Delhi, Accredited by NAAC, Bengaluru

Centre of Excellence in Smart Antenna Systems and Measurements (SAS)

The center of excellence in smart antenna systems and its measurements (SAS) specializes in the analysis, design, optimization and measurement of RF and microwave devices for wireless and defense applications. This facility is for characterization of Antennas and also doubles as an EMI/EMC test facility. This large Electromagnetics and Microwave facility will be utilized for multiple activities R & D activities for funded projects, Lab facility for Antenna and EMI/EMC measurements that are a part of our PG programs and Consultancy activities for outsourced measurements.

Key facilities of the centre are i. **Electromagnetic Simulation software**: The SAS center employs various methods for the analysis of radiating devices implemented in bespoke software codes. The commercial package ANSYS HFSS™ is used in conjunction with evolutionary optimizers to affect novel antenna design shapes to meet high performance goals. **ii. Microwave Test Equipment: Rohde & Schwarz Vector Network Analysers** : The R&S®ZVL6vector network analyser has Specified frequency range 9 kHz to 6 GHz with Frequency over range (unspecified): 5 kHz to 7 GHz With Improved trace noise characteristics **iii. Antenna Measurements in Anechoic Chamber:** Far field Antenna Radiation Patterns (700 MHz – 40 GHz): The measurement chamber is equipped with a turntable with ± 0.1° positional accuracy. Measurements are conducted with Broad-Band Horn Antenna reference standards. The SAS faculty has anechoic chamber for antenna measurements and characterization. The room dimensions approximately are Height=2.5 meters (from floor to beam), Length=4 meters and Width=3 meters. The electrical specifications are as follows.

Chamber dimensions	4m ×3m× 2.5m
Frequency range	700MHz-20GHz
Quiet zone size	1m^3
Reflection requirement in the QZ	-40dB below peak
Ripple requirement at the QZ edge	+/- 1.5dB
Test distance	5mt (Approx)
Near field or far field testing	Far Field

The key outcomes from this facility are some of the funded projects from DRDO, NRB, ISRO and private research organizations related to Antennas and electromagnetics. These projects demand the design and validation of the designed structures by characterizing in Anechoic chamber only. One patent has been filed based on the results obtained from the anechoic chamber. There are about 25 publications by faculty and students related to the results obtained from anechoic chamber in reputed IEEE conferences, which are available in IEEE digital explorer and indexed by Scopus. There are 40 designed and working models related to funded projects which are characterized in the anechoic chamber. These structures are available in the institution.

RV College of Engineering®

Go, change the world

Autonomous Institution Affiliated to Visvesvaraya Technological University, Belagavi

Approved by AICTE, New Delhi, Accredited by NAAC, Bengaluru

MI Incubation Center

MI Incubation Center is a privately funded Technology Business Incubator (TBI) established by RSST to activate Innovation and promote entrepreneurship development among students, faculty of RVCE and other RV Institutes such as, RV College of Architecture (RVCA), RV Institute of Management (RVIM) and RV Institute of Technology & Management (RVITM) and other higher educational institutes in the region.

The Centre is not just a co-working space but a startup hub which provides end to end ecosystem for entrepreneurship development, including state-of-the-art infrastructure, seed funding, access to a strong mentoring network of domain experts, business planning and execution, acceleration, marketing, product launch support, go to market strategies, etc.

The center also provides access to startups to get connected with investors, corporates and MSME's to support product and business development. MIIC has signed MoU with leading incubators, accelerators and other institutes of national importance such as IIT and IIM for mentoring and supporting business development of the startups which get incubated at MIIC.

Incubation Model

MI Incubation center has setup FOUR stages in its incubation program

Pre-Incubation – The Centre accepts startup applications at idea level from RVCE students, faculty as well as from non-RV group startups. MIIC screens such applications once a month to identity ideas which have innovative components, are original, technogically feasible and have the potential to develop into a business within a time span of two to three years.

Admission - The startups which are screened through the pre-incubation phase are then invited to give their presentation to a selection panel, which does a thorough feasibility study of the proposal.

Incubation - The startups which are admitted into the center are provided working space, access to all lab and research facilities of RVCE, seed funding (for RVCE student startups only), regular mentoring from domain experts and any other support to develop their product and business.

Graduation - MIIC assists startups to develop their business plans, marketing strategies, developing sales, product launches etc. so that the businesses may further sustain on their own without the support of the center. Once a business reaches a stage of self sustenance, they graduate from MIIC and venture out on their own.

Companies incubated at MI Incubation Center

1) Rubizon Pvt Ltd- Would healing technology (Bio-Med domain)

2) Caranrose Biosol Pvt. Ltd. - Flower preservation Technology (Bio-Tech domain)

3) Upride Network Pvt. Ltd - Socio Educational Platform (E-Commerce)

4) Suchandra Technologies Pvt. Ltd - Next Gen Power Bank systems (Electronic Hardware)

5) Maven - Social blogging platform (E-commerce)

6) Biozzy Pvt. Ltd. - Developing resins from wet waste (Bio Tech domain)

Manuscript Guidelines

Provide a separate title page containing title, all author names, affiliations, and contact information of the corresponding author.

Submission of a manuscript implies that the work described has not been published before; that it is not under consideration for publication anywhere else; that its publication has been approved by all co-authors, if any, as well as by the responsible authorities – tacitly or explicitly – at the institute where the work has been carried out. The publisher will not be held legally responsible should there be any claims for compensation.

Permissions: Authors wishing to include figures, tables, or text passages that have already been published elsewhere are required to obtain permission from the copyright owner(s) for both the print and online format and to include evidence that such permission has been granted when submitting their papers. Any material received without such evidence will be assumed to originate from the authors.

The article can be mailed to rvjsteam@rvce.edu.in

Title page Essentials

Title: A concise and informative title, Avoid abbreviations and formulae where possible.

Authors and Affiliations: The name(s) of the author(s), Affiliation(s) and complete postal address of the author (s), e-mail address and telephone number (s) of the corresponding author.

Abstract

Please provide an abstract of 150 to 250 words. The abstract should not contain any undefined abbreviations or unspecified references. It should present concisely the objectives, methodology followed, results obtained, and their significance.

Keywords

Please provide five keywords which can be used for indexing purposes

Text Formatting

Manuscripts should be submitted in word format

- Text to be typed double-spaced, in a single column using 12-point type (Times New Roman)
- Use italics for emphasis
- Use the automatic page numbering function to number the pages
- Do not use field functions
- Use tab stops or other commands for indents, not the space bar
- Use the table function, not spreadsheets, to make tables

- Use the equation editor or Math Type for equations
- Save your file in docx format (Word 2007 or higher) or doc format (older Word versions)

Headings

Please use no more than three levels of displayed headings

Abbreviations

Abbreviations should be defined at first mention and used consistently thereafter

Acknowledgments

Acknowledgments of people, grants, funds, etc. should be placed in a separate section on the title page. The names of funding organizations should be written in full

Scientific style

Please always use internationally accepted signs and symbols for units (SI units)

Please use the standard mathematical notation for formulae, symbols etc

- Italic for single letters that denote mathematical constants, variables, and unknown quantities
- Roman/upright for numerals, operators, and punctuation, and commonly defined functions or abbreviations, e.g., cos, det, e or exp, lim, log, max, min, sin, tan, d (for derivative)
- Bold for vectors, tensors, and matrices

Maximum number of pages: The article should not exceed maximum of 15 pages in word format.

Reference citation

Reference citations in the text should be identified by numbers in square brackets. Some examples:

1. Negotiation research spans many disciplines [3]
2. This result was later contradicted by Becker and Seligman [5]
3. This effect has been widely studied [1-3, 7]

Reference list

The list of references should only include works that are cited in the text and that have been published or accepted for publication. Do not use footnotes or endnotes as a substitute for a reference list. The entries in the list should be numbered consecutively.

Format of References:

Journal article: F X Gamelin, G Baquet, S Berthoin, D Thevenet, C Nourry, S Nottin, L Bosquet, Effect of high intensity intermittent training on heart rate variability in prepubescent children, Eur J Appl Physiol, 3 (5), 238 - 253, 2009

Patents: F Bischoff, Apparatus for vapour deposition of silicon, U.S. Patent 3 335 697, 1967

Thesis: R C Nongpiur, Near-End Crosstalk Cancellation in xDSL Systems, Doctoral thesis, University of Victoria, 2005.

Article by DOI: M K Slifka, J L Whitton, Clinical implications of dysregulated cytokine production. J Mol Med, 2010, https://doi.org/ 10.1007/s001090000086

Book: J South, B Blass, The future of modern genomics, Blackwell, London, ISSN, Edition, 2017

Tables:

- Number all the tables using Arabic numerals
- Cite the tables in the text in consecutive numerical order
- For each table, provide a caption (title) stating the components of the table
- Identify any previously published material by giving the original source in the form of a reference at the end of table caption

Figures:

- Number all figures using Arabic numerals
- Cite the figures in the text in consecutive numerical order
- Denote the figure parts by lowercase letters (a, b, c etc.)
- For each figure, provide a caption (title) stating the components of the figure
- No punctuation is to be included after the number, nor is any punctuation to be placed at the end of the caption
- Identify all elements found in the figure in the figure caption; and use boxes, circles, etc., as coordinate points in graphs.
- Identify any previously published material by giving the original source in the form of a reference at the end of figure caption
- Color or grayscale photographs, keep to a minimum of 300 dpi.

Conflict of interest

All benefits in any form from a commercial party related directly or indirectly to the subject of this manuscript or any of the authors must be acknowledged. For each source of funds, both the research funder and the grant number should be given. This note should be added in a separate section before the reference list. If no conflict exists, authors should state: The authors declare that they have no conflict of interest.